UNIVERSITY OF CALIFORNIA SAN DIEGO

Exploring size-tunable magnetite nanoparticles: synthesis, characterization, and quantification of superparamagnetic materials

A dissertation submitted in partial satisfaction of the requirements
for the degree Doctor of Philosophy

in

Chemistry

by

Kyle M. Kirkpatrick

Committee in charge:

Professor Jeffrey D. Rinehart, Chair
Professor Javier Garay
Professor Brian Leigh
Professor Michael Sailor
Professor Alina Schimpf

2023

The dissertation of Kyle M. Kirkpatrick is approved, and it is acceptable in quality and form for publication on microfilm and electronically.

University of California San Diego

2023

DEDICATION

To my parents

TABLE OF CONTENTS

LIST OF FIGURES

LIST OF TABLES

ACKNOWLEDGEMENTS

First and foremost, I must thank my PhD advisor, Professor Jeff Rinehart. His unwavering passion for science, dedication to his students, and constant support has been an incredible source of encouragement during graduate school. I also thank my undergraduate advisor, Professor Harry Dorn, who took me on in my last two years at Virginia Tech. Having spent almost 50 years in the Chemistry department, Professor Dorn was an incredible source of wisdom, when at the time, I was unsure of the path I wanted to pursue. His kindness, friendship, and commitment to his students is something I still hold with me today. I feel incredibly grateful to have had the opportunity to learn from these two mentors who are just as committed to performing great science as they are in caring about the well-being and success of their students.

I am grateful to all the members of the Rinehart group who I have interacted with during my time at UCSD. Postdoc Phil Bunting joined the lab shortly after I did and has made a tremendous positive influence on my success as a graduate student. Even when busy, Phil was excited to teach me a new technique or show me a better way to do something. Next, I thank Ben Zhou, my graduate student mentor who spent countless hours teaching me the art of nanoparticle synthesis. To Jeremy Hilgar, Alex Mantanona, Max Bernbeck, Angelica Orlova, and Zachary Chavez, thank you for teaching me the ways of crystallography and helping me view magnetism from a different perspective. To Tara Zand and Yijun Xie, thank you for kindness and for always making the lab environment pleasant.

I thank my family for their unwavering guidance and motivation throughout this experience. Finally, I am grateful to have found my partner, Nathalia, during graduate school and I am appreciative for her unconditional love, support, and encouragement.

Chapter 2, in full, is a reformatted reprint from the manuscript entitled "Size-Tunable Magnetite Nanoparticles from Well-Defined Iron Oleate Precursors" by Kirkpatrick, K. M.; Zhou, B. H.; Bunting, P. C.; Rinehart, J. D. The dissertation author was a primary researcher and author of this paper. Reprinted with permission from *Chem. Mater.* **2022**, *34* (17), 8043–8053. Copyright 2022 American Chemical Society.

Chapter 3, in full, is a reformatted reprint from the manuscript entitled "Quantifying Superparamagnetic Signatures in Nanoparticle Magnetite: A Generalized Approach for Physically Meaningful Statistics and Synthesis Diagnostics" by Kirkpatrick, K. M.; Zhou, B. H.; Bunting, P. C.; Rinehart, J. D. The dissertation author was a primary researcher and author of this paper. Reprinted with permission from *Chem. Sci.* **2023**, *14* (27), 7589–7594. Reproduced with permission from the Royal Society of Chemistry.

Chapter 4, is partially adapted from the manuscript entitled "Molecular Network Approach to Anisotropic Ising Lattices: Parsing Magnetization Dynamics in Er^{3+} Systems with 0–3-Dimensional Spin Interactivity" by Orlova, A. P.; Varley, M. S.; Bernbeck, M. G.; Kirkpatrick, K. M.; Bunting, P. C.; Gembicky, M.; Rinehart, J. D. The dissertation author was a secondary researcher of this paper. Reprinted with permission from *J. Am. Chem. Soc.* **2023.** Copyright 2023 American Chemical Society.

VITA

2014 Bachelor of Science in Chemistry, Virginia Tech

2018 Master of Science in Chemistry, University of California San Diego

2023 Doctor of Philosophy in Chemistry, University of California San Diego

PUBLICATIONS

Orlova, A. P.; Varley, M. S.; Bernbeck, M. G.; **Kirkpatrick, K. M.**; Bunting, P. C.; Gembicky, M.; Rinehart, J. D. Molecular Network Approach to Anisotropic Ising Lattices: Parsing Magnetization Dynamics in Er^{3+} Systems with 0–3-Dimensional Spin Interactivity. *J. Am. Chem. Soc.* **2023**, jacs.3c08946.

Kirkpatrick, K. M.; Zhou, B. H.; Bunting, P. C.; Rinehart, J. D. Quantifying Superparamagnetic Signatures in Nanoparticle Magnetite: A Generalized Approach for Physically Meaningful Statistics and Synthesis Diagnostics. *Chem. Sci.* **2023**, *14* (27), 7589–7594.

Kirkpatrick, K. M.; Zhou, B. H.; Bunting, P. C.; Rinehart, J. D. Size-Tunable Magnetite Nanoparticles from Well-Defined Iron Oleate Precursors. *Chem. Mater.* **2022**, *34* (17), 8043–8053.

Koutsouflakis, E.; Krylov, D.; Bachellier, N.; Sostina, D.; Dubrovin, V.; Liu, F.; Spree, L.; Velkos, G.; Schimmel, S.; Wang, Y.; Büchner, B.; Westerström, R.; Bulbucan, C.; **Kirkpatrick, K. M.**; Muntwiler, M.; Dreiser, J.; Greber, T.; Avdoshenko, S. M.; Dorn, H.; Popov, A. A. Metamagnetic Transition and a Loss of Magnetic Hysteresis Caused by Electron Trapping in Monolayers of Single-Molecule Magnet $Tb_2@C_{79}N$. *Nanoscale* **2022**, *14* (27), 9877–9892.

Velkos, G.; Krylov, D. S.; **Kirkpatrick, K. M.**; Spree, L.; Dubrovin, V.; Büchner, B.; Avdoshenko, S. M.; Bezmelnitsyn, V.; Davis, S.; Faust, P.; Duchamp, J.; Dorn, H. C.; Popov, A. A. High Blocking Temperature of Magnetization and Giant Coercivity in the Azafullerene $Tb_2@C_{79}N$ with a Single-Electron Terbium–Terbium Bond. *Angew. Chem. Int. Ed.* **2019**, *58* (18), 5891–5896.

Velkos, G.; Krylov, D. S.; **Kirkpatrick, K. M.**; Liu, X.; Spree, L.; Wolter, A. U. B.; Büchner, B.; Dorn, H. C.; Popov, A. A. Giant Exchange Coupling and Field-Induced Slow Relaxation of Magnetization in $Gd_2@C_{79}N$ with a Single-Electron Gd–Gd Bond. *Chem. Commun.* **2018**, *54* (23), 2902–2905.

Wang, X.; McKay, J. E.; Lama, B.; Van Tol, J.; Li, T.; **Kirkpatrick, K. M.**; Gan, Z.; Hill, S.; Long, J. R.; Dorn, H. C. Gadolinium Based Endohedral Metallofullerene $Gd_2@C_{79}N$ as a Relaxation Boosting Agent for Dissolution DNP at High Fields. *Chem. Commun.* **2018**, *54* (19), 2425–2428.

ABSTRACT OF THE DISSERTATION

Exploring size-tunable magnetite nanoparticles: synthesis, characterization, and quantification of superparamagnetic materials

by

Kyle M. Kirkpatrick

Doctor of Philosophy in Chemistry

University of California San Diego, 2023

Professor Jeffrey D. Rinehart, Chair

Superparamagnetic nanoparticles represent an exciting area of research within the broader field of nanoscale materials. Synthetic control over physical properties, such as nanoparticle size, shape, and crystalline phase strongly impact the magnetic properties, ultimately dictating the functionality in potential applications.

Chapter 1 provides a brief background of nanoscale magnetic materials. It discusses the high degree of control possible through colloidal nanoparticle synthesis techniques, as well as common challenges encountered. The chapter includes specific examples on the structure-property

relationship, including implications for magnetism, concluding with a summary of superparamagnetism.

Chapter 2 discusses the efforts to enhance the reproducibility in magnetic nanoparticle synthesis. The chapter introduces two novel forms of iron oleate precursor that offer long-term stability, well-defined stoichiometry, and large-scale availability, addressing issues with reproducibility. These advancements enable the synthesis of magnetite nanoparticles with tunable sizes ranging from 4 to 16 nm and low size dispersity, providing consistent results in the superparamagnetic size regime.

Chapter 3 details the development of a new technique for the quantification and parametrization of superparamagnetic nanoparticle magnetization curves. The size-dependent magnetic properties were elucidated by fitting the data to a statistical model, leading to a better understanding of these materials' behavior and potential for applications. It emphasizes the challenges in interpreting magnetization data and the importance of simplified models in advancing the field.

Chapter 4, in collaboration with Angelica Orlova, presents the extension of the statistical analysis of magnetization data to a molecular system. Three $ErCOT_2$ compounds with varying structures, including the angle, and spacing between magnetic units, were analyzed. The temperature dependence and effect of dipolar coupling between $ErCOT_2$ units on the magnetization curve were analyzed. Each curve was deconvoluted into its components, which were tracked and quantified across the parameter space.

Chapter 1

Fundamentals of Nanoscale Magnetism

1.1 Introduction

Nanoscience is an exciting and rapidly-evolving field of research on materials and phenomena occurring on the nanoscale ranging from 1 to 100 nanometers (nm) in size.[1] While the concepts of nanoscale materials and processes have been recognized for centuries, recent advancements in science and technology have propelled this field into the forefront of scientific exploration. The Scanning Electron Microscope (SEM), for example, has allowed researchers to peer into the complex world of nanoscale materials. Figure 1.1 demonstrates the power of electron microscopy, as tiny 10 nm particles are made visible, showcasing the intricacy that lies beneath the surface of materials we may encounter every day. One of the most important aspects of nanoscale materials is their propensity to exhibit properties distinct from their bulk counterparts. These properties span a wide range of scientific domains and applications, including electronics, medicine, energy, biology, optics, magnetism, and many more.

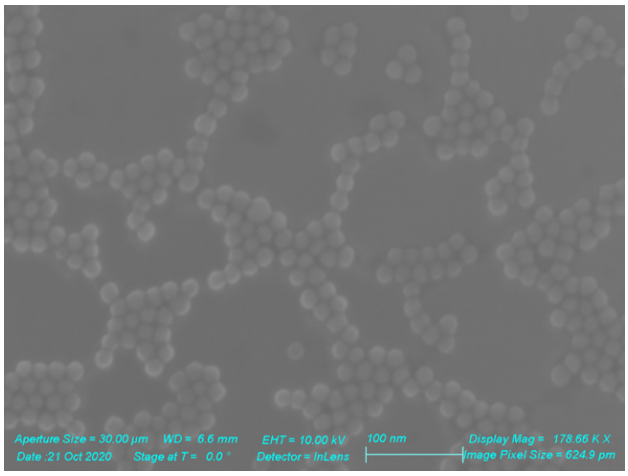

Figure 1.1. Scanning electron microscope (SEM) image of an array of magnetite (Fe_3O_4) nanoparticles.

My research, dating back beyond my graduate studies, has largely focused on elucidating the fundamental structure-property relationship of magnetic nanomaterials. Located at the interdisciplinary intersection between chemistry, physics, and materials science, nanoscale magnetism is a mature, yet largely unexplored field with ample room for further study, innovation, and creativity.

The maturity of nanoscale magnetism is evident in the extensive body of knowledge that has been amassed over the years. Researchers have made significant strides in understanding the principles governing the magnetic behavior of nanomaterials, unraveling the complex phenomena behind superparamagnetism. These foundational concepts provide a solid framework for comprehending the behavior of magnetic nanomaterials at the atomic and molecular levels. The depth of understanding achieved thus far has paved the way for practical applications in areas such as medical diagnostics and magnetic sensors. Despite these advancements, the field remains largely unexplored in terms of its full potential. The intricacies of nanoscale magnetism open up avenues for novel discoveries that could reshape our technological landscape. My research delves into these uncharted territories, pushing the boundaries of current knowledge to uncover new phenomena and establish connections that may have been overlooked, aiming to improve synthetic capabilities and advance characterization methods in the realm of magnetic nanomaterials. By doing so, I aim to contribute not only to the theoretical understanding of nanoscale magnetism, but also to its practical applications, unlocking possibilities for more efficient and advanced magnetic nanomaterials. In the broader context, the interdisciplinary nature of my work reflects the collaborative spirit required to tackle the challenges posed by nanoscale magnetism. Bridging the gaps between chemistry, physics, and materials science is essential for a holistic understanding of the field. My research serves as a testament to the need for diverse perspectives and skill sets in exploring the richness of nanoscale magnetism. As the boundaries between scientific disciplines continue to blur, the potential for groundbreaking discoveries in this mature yet evolving field becomes even more promising.

1.2 Colloidal Nanoparticles

Colloidal nanoparticles are generally defined as nanoscale particles that are stably suspended in a liquid. As particle size decreases from the bulk to the nanoscale, significant differences arise in the electronic and vibrational structure compared to bulk materials. Moreover, this reduction in size substantially increases the surface-to-volume ratio of nanomaterials, a key characteristic that directly influences their extensive range of applications. A significant amount of research has focused on controlling nanoparticle size,[2–5] as it alone determines a number of key properties. For example, optical properties of quantum dots,[6] catalytic properties of gold nanoparticles,[7] and magnetic properties of superparamagnetic nanoparticles[8–10] all strongly depend on particle size. Arguably just as important as size, the broadness and shape of the size distribution can also have a detrimental impact on the intended properties. For example, the physical size distribution of colloidal plasmonic nanoparticles (quantum dots) directly correlates to the sharpness of the peaks in the corresponding optical spectrum.[11,12] Both the precision and accuracy of the observed color emitted from quantum dots is tied to the synthetic capabilities.

Shape control is also an important factor to consider in the structure-property relationship of nanoparticles. A wide range of dimensionalities and shapes are possible through various changes in reaction conditions, ranging from 0D (spherical, cubic, octahedral), 1D (rods and wires), 2D (plates, disks, rings), and 3D (nano-urchins),[13] some of which are demonstrated in Figure 1.2. There are many examples of properties that are dependent on particle shape. In the 0D case, superparamagnetic magnetite (Fe_3O_4) nanoparticles of spheres, cubes, and octahedra exhibit drastically different magnetic properties.[14] In the 1D case, the aspect ratio of cobalt nanorods tunes the magnetic field at which magnetization reversal occurs, commonly referred to as the coercive field (H_c) .[15] In another example, the surface plasmon resonance effect of gold nanorods is dependent on aspect ratio, ultimately permitting treatment of cancerous cells through the photothermal effect.[16] One specific advantage of shape control is the ability to expose specific facets of the nanoparticle's crystal structure, with examples of changes in catalytic activity depending on the available crystal facets in 2D nanomaterials.[17,18]

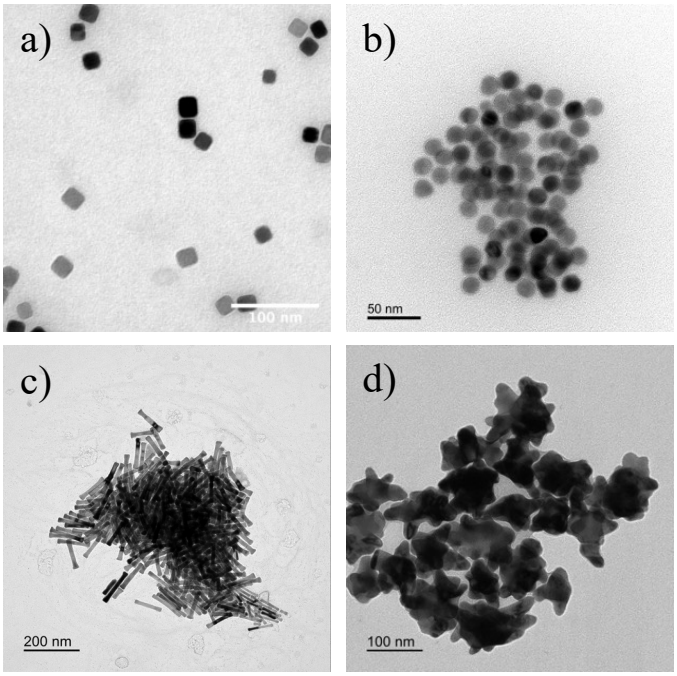

Figure 1.2. Transmission electron microscope (TEM) images highlighting different examples of colloidal nanoparticle shapes. (a) Magnetite (Fe_3O_4) nanocubes synthesized from iron oleate. (b) Ni@NiO core-shell nanoparticles synthesized from nickel acetylacetonate, oleylamine, and trioctylphosphine oxide. (c) Cobalt nanorods synthesized from the polyol method using cobalt laurate. (d) Nickel oxide nanoflowers synthesized from nickel acetylacetonate, oleylamine, and trioctylphosphine oxide.

In the case of every nanomaterial regardless of dimensionality, the morphology influences the packing and alignment on a surface. Low size dispersity (%RSD < 10%) nanoparticles tend to self-assemble into an ordered array when drop-cast from solution onto a surface, forming a superlattice, shown in Figure 1.3. This self-assembly process is driven by a general minimization of energy, ultimately leading to a more favorable energetic state. A wide range of crystal structures, such as face centered cubic (fcc) and body centered cubic (bcc) type packing is possible, along with more complex structures through the introduction of additional materials or driving factors for assembly. For example, interparticle interactions can be mediated by coating nanoparticles with complementary strands of DNA, yielding incredible control over particle arrangement.[19] While superlattice assemblies are aesthetically pleasing, they represent an additional degree of freedom with respect to interparticle interactions, which may influence the thermal, electronic, or magnetic properties.

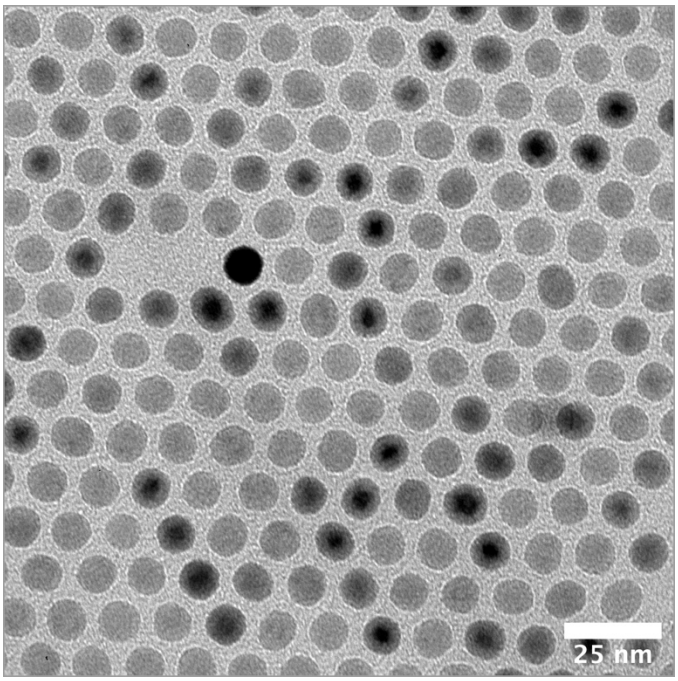

Figure 1.3. TEM image of a superlattice type self-assembly of core-shelled $FeO@Fe_3O_4$ nanoparticles.

Finally, due to the inherent bottom-up-nature and incredible control over reaction conditions, properties can also be modified through changes in nanoparticle composition. This includes core-shell particles where the interior material differs from the exterior material, which can be achieved by a variety of methods. For example, control of gas composition during synthesis can lead to two different iron phases within the same nanoparticle, identified by the difference in contrast within particles in Figure 1.3.[20] Additionally, one may grow a new material onto an existing one, referred to as seed-mediated growth.[21] Nanoscale materials offer opportunities for incredible precision and creativity, ultimately leading to unparalleled control over the resulting properties.

1.3 Synthesis of Colloidal Nanoparticles

Nanoparticles are synthesized by a variety of methods, each with their advantages and disadvantages. Top-down style nanoparticle syntheses involve the breakdown of a larger material through various methods, such as ball milling. This technique involves the mechanical grinding of bulk materials to reduce particle size.[22] Conversely, bottom-up methods involve the assembly of atoms or molecules through various reaction processes. Predominantly performed in the liquid phase, bottom-up methods offer more precise control over the crucial physical properties that render nanoscale materials so extraordinary. Common liquid phase methods for the synthesis of colloidal nanoparticles include co-precipitation, microemulsion, solvothermal, and high temperature thermal decomposition (thermolysis).[23] While all liquid phase techniques produce nanoparticles, in many cases, thermolysis remains the premier option for optimal control of size, size dispersity, shape, and phase.[24–26]

In general, the reaction mixture of a thermolysis based nanoparticle synthesis contains three components: precursor, surfactant, and solvent. Generally, the precursor supplies the metal, the surfactant directs particle growth, and the solvent keeps the reaction mixture in solution. Beyond the reaction contents, there are countless parameters that provide additional levels of control, including temperature, stir rate,[27] gas composition and gas flow rate,[28,29] and choice of glassware.[30] Due to all these factors (and many more not listed) and in efforts to avoid the mysticism (irreproducible or unverifiable results only achievable by certain researchers) so commonly encountered in nanoparticle synthesis, it is imperative that synthetic methods are kept consistent and contain as much detail as possible.

The first component of the reaction, the precursor, is arguably the most important of the three, as it contains the metal(s) of choice. Examples of common precursors include metal chlorides, metal alkoxides, metal carbonyls, metal carbonates, and a wide number of organometallic compounds.[31–33] Selecting the correct precursor for modulation of the intended nanoparticle property is challenging, considering the abundance of research spent developing precursors.[34–38] Considerations must be made with regard to purity,

decomposition properties, oxidation state, and reactivity of the precursor material, as they ultimately impact the resulting nanoparticles.[31]

Thermolysis results in a colloidal suspension of particles coated with surfactant to keep them dispersed in solution. The surfactant is an organic amphiphilic molecule containing a functional group that attaches to the nanoparticle surface, while also containing a long chain non-polar carbon chain. Common surfactants include oleic acid (OA), oleylamine (OAm), and trioctylphosphine oxide (TOPO), each containing a carboxylate, amine, and phosphine oxide group, respectively, that binds to or "caps" the nanoparticle surface. Surfactant may also be present within the precursor material itself.[31] In addition to the role of surfactant in dispersing the nanoparticles in solution and preventing aggregation, the quantity and type of surfactant strongly impacts nanoparticle growth, ultimately presenting itself through changes in nanoparticle size and shape. For example, the use of surfactant with a propensity to bind to a specific facet of a nanoparticle surface may help direct its overall shape, while the overall amount of surfactant in a reaction helps to determine the final nanoparticle size.[39,40]

Finally, the solvent choice has a significant impact on the resulting nanoparticles, as it determines the boiling point of the reaction mixture. This boiling/reflux point can be another source of control, as it has been correlated with nanoparticle size.[29] Additionally, the solvent may determine the overall reducing or oxidizing power of the reaction. In the case of the polyol-based synthesis of metallic nanoparticles, controlled decomposition of the solvent itself in the presence of base is responsible for the strongly reducing atmosphere, ultimately determining the phase (e.g., Fe vs. Fe_3O_4).[5,41]

While control over the contents of the reaction mixture can lead to exquisite control over the physical properties of the resulting nanoparticles, it is a challenging task. Nanoparticle synthesis represents a uniquely complex system with many variables beyond just the reaction components. Truly understanding the mechanism and sources of control in a nanoparticle reaction requires rigorous and extensive experimentation. A primary goal of the research described in this dissertation is to identify and fix aspects of superparamagnetic nanoparticle synthesis and characterization that facilitate its quantitative characterization in forms of greater utility to those interested in potential commercial application. This

process includes more consistent production of phase pure materials and detection of impurity phases, as well as quantification of thermodynamic and kinetic aspects of the magnetization important to use in sensing, imaging, magnetothermal generation, and magnetic switching and torque. This topic as it pertains to synthesis of magnetic nanoparticles is discussed in detail in Chapter 2.

1.4 Magnetism in Nanoscale Materials

The incorporation of magnetism to colloidal nanoparticles introduces an additional layer of complexity, specifically in how the size, size dispersity, shape, exposed facets, and surface ligands contribute to the overall magnetic properties. Reliable synthetic methods are of utmost importance, as slight changes in physical characteristics can either facilitate or limit the functional magnetic capabilities.

Magnetic materials can be broadly categorized based on their response to an externally applied magnetic field, including diamagnetism, paramagnetism, and ferromagnetism. Present in every material, diamagnetism is a result of the orbital motion of electrons generating a weakly opposing magnetic moment with respect to the direction of the applied magnetic field. Conversely, paramagnetism is observed in materials containing unpaired electrons, resulting in an attraction to a magnetic field. Importantly, paramagnetism does not exhibit long-range ordering and does not retain its magnetic moment when removed from a magnetic field. Ferromagnetic materials, such as Fe, Co, and Ni also contain unpaired electrons yet are characterized by an alignment or long-range ordering of spins. Under the broader umbrella of ferromagnetism, subclassifications include ferrimagnetism and superparamagnetism. In the case of ferrimagnetism, a net magnetic moment is produced as a result of the anti-alignment of multiple sublattices with varying (unequal) magnitudes. Examples of ferrimagnetic materials include the spinel ferrites MFe_2O_4, where M represent Fe^{2+}, Co^{2+} and Ni^{2+}.

Thus far in this brief classification of magnetic materials, the assumption has been that all materials are in their bulk state, however, when certain magnetic materials are made on the nanoscale, a new subcategory of magnetism emerges, known as superparamagnetism. While a bulk material might contain

many grains of large size and thus multiple magnetic domains, nanoscale materials exhibiting superparamagnetism consist of single magnetic domains. In the realm of superparamagnetism, a distinctive feature emerges; thermal energy becomes commensurate with the energy barrier required for the collective magnetic moment to reverse. When thermal energy exceeds this threshold, the magnetic moment traverses the barrier, leading to a net zero magnetic moment among the entire collective sample of nanoparticles. Conversely, if thermal energy decreases below this threshold, the moment becomes effectively "blocked" or immobilized on one side of the energy barrier. The energy landscape for superparamagnetic nanoparticles can be conceptualized as a form of the double well potential model, depicted in Figure 1.4.

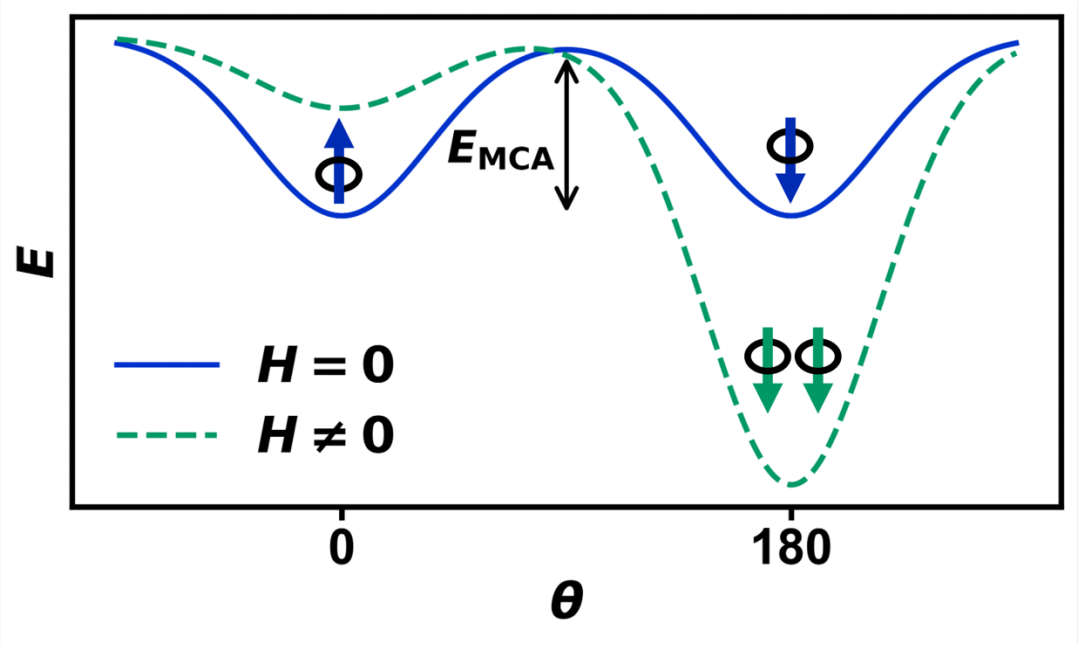

Figure 1.4. Schematic of superparamagnetic energy barrier. With no applied magnetic field ($H = 0$), there is an equal population of nanoparticle moments in the up ($\theta = 0°$) and down ($\theta = 90°$) states. In this example, with an applied magnetic field ($H \neq 0$), the nanoparticle moments in the up state become destabilized and are able to rotate over the barrier.

$$E_{MCA} = KVsin^2(\theta) \qquad \text{Equation 1.1}$$

The energy barrier of superparamagnetism results from magnetocrystalline anisotropy, described by Equation 1.1, which is a preference for the magnetic moment to point in a particular direction stemming from the physical crystal structure of the material. This preferential direction is described as the “easy axis”.

In a uniaxial particle containing a single easy axis, the energy is minimized when the direction of the magnetic field is parallel to this easy axis. As the angle between the two, denoted θ, changes between 0 and 90°, the energy increases, then decreases following the shape of the double well schematic. While the relative energy at any point is determined by θ, the anisotropy constant K, and the particle volume V, determine the magnitude of the energy barrier. The competition between thermal energy and degree of accessibility over the energy barrier can be directly visualized through a measurement of magnetization vs. temperature.

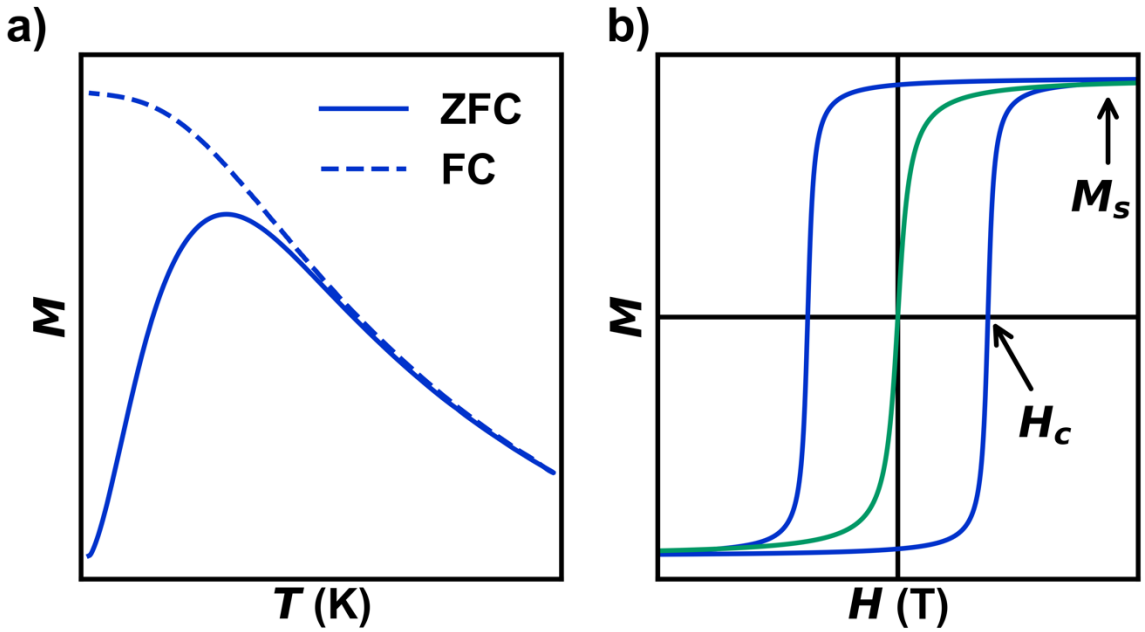

Figure 1.5. Typical measurements for the characterization of magnetic materials. (a) Plot of zero-field cooled (ZFC) susceptibility and field cooled (FC) susceptibility. (b) Plot of magnetization curves for a typical superparamagnet above the blocking temperature (green) and below the blocking temperature (blue). The location of two important parameters, saturation magnetization (M_s) and coercive field (H_c), are highlighted on the curve.

This measurement consists of two parts: zero-field cooling (ZFC, solid) and field cooling (FC, dashed), shown in Figure 1.5a. When combined, the temperature dependent dynamics are revealed, specifically the temperature above which the nanoparticles exhibit superparamagnetic behavior. The split between the ZFC and FC curves is one indication of superparamagnetism, and it occurs where the energy barrier for magnetic moment alignment becomes equal to thermal energy. First, cooling under zero-field

essentially freezes the system in place with an equal population of magnetic moments on each side of the barrier, leading to a net zero magnetic moment. After cooling under zero-field, a small magnetic field, typically 100 Oersted (0.01 Tesla), is applied. The magnetization is measured as temperature is slowly increased. As thermal energy is reintroduced into the system, the nanoparticle moments can begin to orient themselves with the small magnetic field. Eventually, a peak in the magnetization forms near the "blocking temperature," where the blocking temperature is defined as the temperature at which the superparamagnetic material is able to re-establish equilibrium on the timescale of the measurement once more. A single agreed upon definition for the blocking temperature does not exist unanimously, as multiple methods for blocking temperature determination exist depending on the field.[42,43] In superparamagnetism literature, typical choices for the blocking temperature involve determining the temperature at which the maximum ZFC magnetization occurs, identifying the temperature corresponding to the inflection point, or pinpointing the temperature at which a peak appears in the derivative of the difference between the ZFC and FC curves. Above the blocking temperature, thermal energy again exceeds the energy barrier, leading to a net zero magnetization as the moments fluctuate randomly over the barrier. Next, in the FC case, the nanoparticle moments are already biased in the direction of the magnetic field, resulting in a larger magnetization at low temperatures. The shape of the FC curve below the blocking temperature yields information on interparticle interactions, described in more detail in Chapter 3. Finally, as the temperature increases, the FC curve converges with the ZFC curve near the blocking temperature.

While the temperature dependence of magnetization yields significant insights into the behavior of superparamagnetic nanoparticles, the magnetic field dependence can reveal further information. The measurement of a magnetization curve is demonstrated in Figure 1.5b, in which a magnetic field is swept from a large negative applied field to a large positive applied field (left to right), a sharp increase in magnetization is observed. Due to the nature of the double well behavior described above, superparamagnetic nanoparticles above the blocking temperature (green) exhibit zero magnetization at zero field. This is demonstrated by the complete lack of coercivity or a coercive field (H_c), referring to the

magnetic field needed to demagnetize a material. When below the blocking temperature, however, coercivity is observed in the magnetization curve (blue).

An additional parameter from the measurement of a magnetization curve is saturation magnetization (M_s), which represents the sum of all magnetic moments in a material, typically normalized by mass or volume. In a sample of superparamagnetic nanoparticles, saturation magnetization is determined by particle size, phase, and overall mass of superparamagnetic material being measured. Depicted in Figure 1.5b, saturation magnetization is measured by applying a large magnetic field to a sample and determining the magnetization in which no further increase is observed. Typically, saturation magnetization is invoked as an indicator of crystallinity and thus, particle quality. While bulk Fe_3O_4 exhibits a saturation magnetization of roughly 92 emu/g,[44] directly comparing this saturation magnetizations of nanoscale Fe_3O_4 is not a recommended approach. A host of variables, including size, shape, surface effects, crystalline defects, and mass percentage of non-superparamagnetic material present in the sample all contribute to inconsistencies between the bulk and nanoscale saturation magnetization values.[45–48] Moreover, the combined effect of errors in both mass and magnetization measurement can result in significant variations in saturation magnetization. The difference in error of the sample mass (± 0.1 mg) is roughly 10^2 larger than the error in magnetic moment.

Magnetite (Fe_3O_4) nanoparticles are the superparamagnetic material of choice throughout this dissertation. While many superparamagnetic materials exist, such as cobalt nanoparticles, magnetite is a naturally occurring material in nature and it is biocompatible, making it attractive for potential biomedical applications. Additionally, magnetite exhibits a large saturation magnetization, and a wealth of knowledge is available on its synthesis and characterization. The topic of magnetization curves of superparamagnetic nanoparticles is discussed in more detail in Chapter 3.

1.5 Outlook of Superparamagnetic Nanoparticles

While the work described in this dissertation primarily focuses on the fundamental research of superparamagnetic nanoparticles, there are implications in many applications, including biomedical imaging, drug delivery, cancer treatment, and sensing of biomolecules.[23,34,49–51] Superparamagnetic iron oxide nanoparticles, in general, exhibit biocompatibility, possess intrinsic customizability, and can be functionalized with biomolecules for precise targeting of specific cells or tissues. One example of an application that directly depends on the size and size distribution of superparamagnetic nanoparticles is Magnetic Particle Imaging (MPI). A relatively new technique, MPI is an alternative to MRI imaging, especially MRI imaging with the assistance of gadolinium-based contrast agents, which have been shown to be harmful in patients with kidney issues.[52,53] MPI relies on an oscillating AC magnetic field to determine the location and intensity of the superparamagnetic nanoparticles, up to a spatial resolution of roughly 1 mm.[54] Likely introduced to the body via an injection or oral ingestion, the magnetic nanoparticles emit a signal in a magnetic field, allowing researchers and doctors to visualize internal structures, track blood flow, and diagnose medical conditions. Due to the inherent selectivity for magnetic material and the thousand order of magnitude difference in magnetic moment compared to paramagnetic molecules such as gadolinium, MPI proves to be an exceptionally sensitive technique for high-resolution cancer detection and imaging. The MPI signal itself is directly related to the derivative of the magnetization curve.[55] As such, a sharp magnetization curve requires a smaller magnetic field and leads to a MPI signal with a higher signal-to-noise ratio. Conversely, one may desire an MPI signal that is less sensitive at the expense of using a larger magnetic field range. The success of MPI hinges on the consistent and reliable synthesis of superparamagnetic nanoparticles. The size, size distribution, and shape of the superparamagnetic nanoparticles all strongly influence the magnetization curve, consequently impacting the MPI signal shape and intensity.[56] The improved parameterization of magnetization curves is far-reaching in terms of its implications, as it could be used to both predetermine and quantify existing MPI signals. The future

prospects for superparamagnetic nanoparticles will undeniably revolve around their contributions to biomedical applications.

In a similar process to the AC magnetic field of several kHz utilized in MPI, a much larger frequency in the MHz range can lead to the conversion of magnetic energy into heat. Known as magnetic hyperthermia, this technique may potentially be used to ablate cancerous tumors and release drugs following thermal degradation triggered by the AC magnetic field.[57] Similarly to the role of physical properties directing the magnetic properties with respect to MPI, the same is true of magnetic hyperthermia. An incredible amount of research has been carried out correlating size, elemental composition, shape, and crystallinity with magnetic hyperthermia performance.[45,57–59] For example, the use of zinc substituted ferrite ($ZnFe_2O_4$) results in a larger saturation magnetization compared to the non-substituted ferrite (Fe_3O_4) analogue, leading to a higher heat capacity.[60]

Beyond biomedicine, the improved nanoparticle synthesis and analysis of magnetization curves finds a direct application in granular magnetoresistance, an area where the Rinehart Lab holds expertise.[9,30] The discovery of various enhanced magnetoresistive (MR) effects in the late 1980s resulted in one of the most universally relevant quantum phenomena in modern technology.[61] Fundamentally, MR effects convert magnetic signals into electronic ones, which are generally more manageable, as they can be easily amplified, processed, and transmitted via various compatible electronic components. Characterized by the ability of magnetic material to change its electrical resistance with a small applied magnetic field, MR found its primary application in computing technology in the form of hard disk read-heads.[62] While this has undeniably made an impact on our daily lives, there remains ample room for further exploration and advancement in the field of sensing capabilities through enhanced MR effects. Beyond data storage, MR sensors are widely employed in various applications, encompassing industrial uses such as position, angle, and speed measurements, geophysical devices, and consumer electronics where they serve as compasses.[62–64] Additionally, MR sensors are used to detect and quantify a variety of biomolecules.[49,65–67]

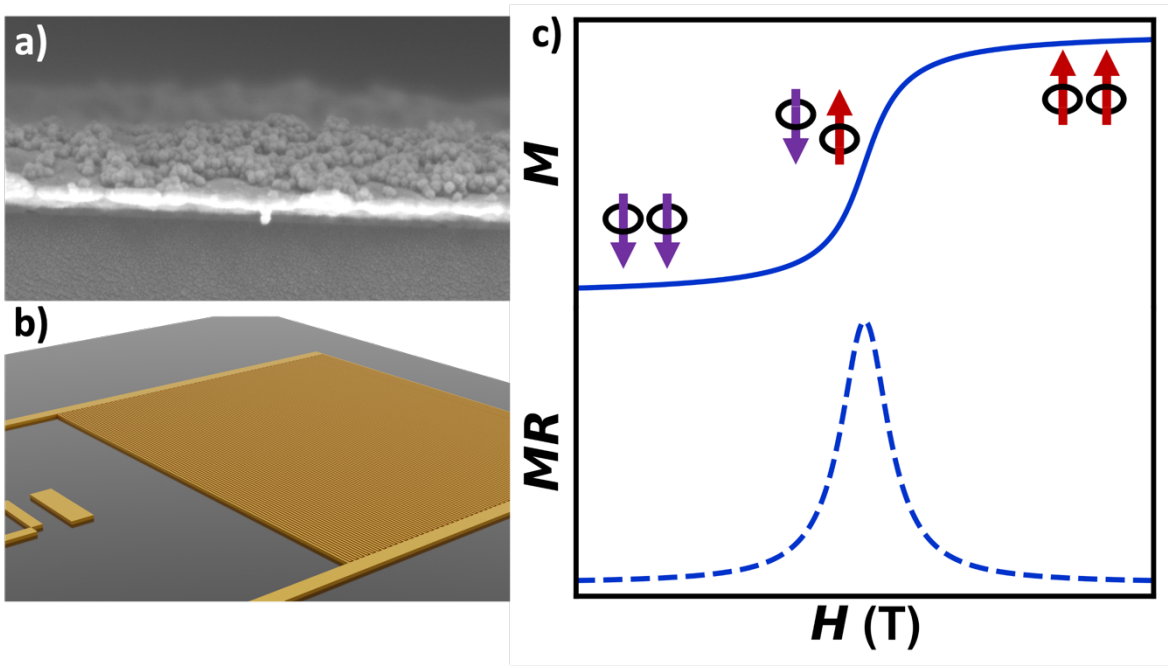

Figure 1.6. Granular magnetoresistance of colloidally prepared magnetic nanoparticles. (a) SEM image of thin film of magnetite nanoparticles. (b) 3-D model of interdigitated gold electrodes with a 10 μm spacing for magnetoresistance testing. (c) Plot of magnetization (blue) and corresponding magnetoresistance curve (green) for superparamagnetic nanoparticles.

Granular magnetoresistance is an enhanced MR effect found in arrays of magnetic nanomaterials separated by insulating materials, which act as tunnel barrier junctions. While MR effects based on tunnel barrier junctions are typically made through highly complex thin films of various magnetic and non-magnetic material manufactured in a cleanroom through expensive processes, granular MR is a promising low-cost alternative with the potential for a similar degree of control. A physical representation of a granular MR system consisting of Fe_3O_4 nanoparticles on a silicon surface is shown in Figure 1.6a. While thin film MR relies on the high spin selectivity of a single complex interface, the advantage of granular MR is in the sheer number of interfaces; each boundary in a thin film of nanoparticles becomes spin selective. Shown in Figure 1.6b, the MR effects of colloidal nanoparticles are measured by drop-casting a suspension of nanoparticles onto a tiny device consisting of interdigitated gold electrodes, which increase the overall electrode surface area. The nanoparticles fill in the 10 μm gaps between the electrodes, the contact pads are connected to gold wire via a soldering process, and the device is inserted into the SQUID magnetometer

for measurements. The basis of the granular MR effect with respect to the magnetization is demonstrated in Figure 1.6c. With no applied magnetic field, the system is at a high-resistance state, as nanoparticle moments are randomly aligned. With a small applied magnetic field, however, the nanoparticle moments align with the field, resulting in a low-resistance state.

The magnitude, curvature, and overall resistance is strongly dependent on the physical properties of the constituent nanoparticles used in the magnetoresistor. Thankfully, colloidal nanochemistry allows for incredible control over the physical properties that impact MR. The link between these two, however, is often unclear and warrants additional exploration. In 2018, Ben Zhou of the Rinehart lab elucidated the relationship between nanoparticle size ($CoFe_2O_4$) and the corresponding height of the MR curve.[9] It was discovered that smaller nanoparticles (5.3 nm) exhibited the largest MR response due to the increased number of interfaces between particles. While the size-dependence was elucidated, it represents just one of many parameters involved.

Depending on the application, one may need a sharp MR curve with the application of a small magnetic field, while another may require a wide MR signal that is resistant to change beyond a specific magnetic field. This particular level of control over the MR curve was achieved by physically mixing magnetically "hard" nanoparticles ($CoFe_2O_4$), which resist switching of its magnetization, with "soft" nanoparticles (Fe_3O_4) that rapidly switch magnetization in response to a small magnetic field.[30] Together, this combination of magnetic materials forms a pseudo-spin valve, resulting in incredible control over the MR curve shape. Beyond nanoparticle size and overall phase composition, parameters such as intrinsic material conductivity, ligand choice, and particle alignment can potentially push the boundaries of granular MR further. For example, changing from Fe_3O_4 to $Fe@Fe_3O_4$ through a small change in the gas flow composition during synthesis would result in a significantly more electrically conductive material, as well as a sharper and larger MR curve as a result of a larger saturation magnetization, demonstrated in Figure 1.7.[68] The exploration into non-ferrite materials would potentially increase the functionality of granular MR in its current state.

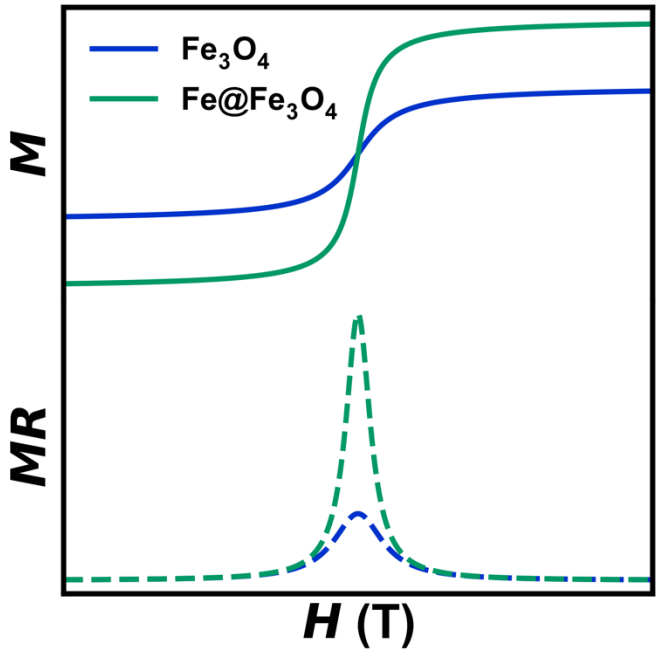

Figure 1.7. Example magnetization curve (top) and corresponding magnetoresistance curve for assemblies of Fe_3O_4 and $Fe@Fe_3O_4$ nanoparticles.

1.6 Organization of Chapters

The following chapters detail our efforts to more fully understand the fundamental structure-property relationship of superparamagnetic magnetite nanoparticles. Chapter 2 delves into the synthetic challenges associated with the iron oleate precursor and our solution in developing an improved precursor. Using this new precursor, the parameter space of iron content and ratio between iron and ligand in the nanoparticle synthesis was explored, leading to fine size control in the 5-20 nm range. The ability to reproducibly synthesize magnetite nanoparticles in a tunable size range with acceptable size distributions set the stage for the following study described in Chapter 3, which focuses on the statistical modelling of superparamagnetic magnetization curves. While saturation magnetization is typically invoked in the discussion of magnetite nanoparticle quality, fitting the data to a purely statistical distribution results in new quantifiable parameters that more fully describe the curvature of the magnetization curve. The success of the technique led to its implementation in analyzing magnetization curves of molecular magnetic materials with Angelica Orlova of the Rinehart Lab. Chapter 4 focuses on the extension of the fitting procedure to

molecular systems with complex magnetization curves, leading to unparalleled quantification and depiction of demagnetization processes that would have otherwise gone unobserved.

1.7 References

(1) Bayda, S.; Adeel, M.; Tuccinardi, T.; Cordani, M.; Rizzolio, F. The History of Nanoscience and Nanotechnology: From Chemical–Physical Applications to Nanomedicine. *Molecules* **2019**, *25* (1), 112. https://doi.org/10.3390/molecules25010112.

(2) Wu, L.; Mendoza-Garcia, A.; Li, Q.; Sun, S. Organic Phase Syntheses of Magnetic Nanoparticles and Their Applications. *Chem. Rev.* **2016**, *116* (18), 10473–10512. https://doi.org/10.1021/acs.chemrev.5b00687.

(3) Reiss, P.; Carrière, M.; Lincheneau, C.; Vaure, L.; Tamang, S. Synthesis of Semiconductor Nanocrystals, Focusing on Nontoxic and Earth-Abundant Materials. *Chem. Rev.* **2016**, *116* (18), 10731–10819. https://doi.org/10.1021/acs.chemrev.6b00116.

(4) Gawande, M. B.; Goswami, A.; Felpin, F.-X.; Asefa, T.; Huang, X.; Silva, R.; Zou, X.; Zboril, R.; Varma, R. S. Cu and Cu-Based Nanoparticles: Synthesis and Applications in Catalysis. *Chem. Rev.* **2016**, *116* (6), 3722–3811. https://doi.org/10.1021/acs.chemrev.5b00482.

(5) Fiévet, F.; Ammar-Merah, S.; Brayner, R.; Chau, F.; Giraud, M.; Mammeri, F.; Peron, J.; Piquemal, J.-Y.; Sicard, L.; Viau, G. The Polyol Process: A Unique Method for Easy Access to Metal Nanoparticles with Tailored Sizes, Shapes and Compositions. *Chem. Soc. Rev.* **2018**, *47* (14), 5187–5233. https://doi.org/10.1039/C7CS00777A.

(6) Murray, C. B.; Norris, D. J.; Bawendi, M. G. Synthesis and Characterization of Nearly Monodisperse CdE (E = Sulfur, Selenium, Tellurium) Semiconductor Nanocrystallites. *J. Am. Chem. Soc.* **1993**, *115* (19), 8706–8715. https://doi.org/10.1021/ja00072a025.

(7) Zhou, X.; Xu, W.; Liu, G.; Panda, D.; Chen, P. Size-Dependent Catalytic Activity and Dynamics of Gold Nanoparticles at the Single-Molecule Level. *J. Am. Chem. Soc.* **2010**, *132* (1), 138–146. https://doi.org/10.1021/ja904307n.

(8) Demortière, A.; Panissod, P.; Pichon, B. P.; Pourroy, G.; Guillon, D.; Donnio, B.; Bégin-Colin, S. Size-Dependent Properties of Magnetic Iron Oxide Nanocrystals. *Nanoscale* **2011**, *3* (1), 225–232. https://doi.org/10.1039/C0NR00521E.

(9) Zhou, B. H.; Rinehart, J. D. A Size Threshold for Enhanced Magnetoresistance in Colloidally Prepared $CoFe_2O_4$ Nanoparticle Solids. *ACS Cent. Sci.* **2018**, *4* (9), 1222–1227. https://doi.org/10.1021/acscentsci.8b00399.

(10) Pauly, M.; Pichon, B. P.; Panissod, P.; Fleutot, S.; Rodriguez, P.; Drillon, M.; Begin-Colin, S. Size Dependent Dipolar Interactions in Iron Oxide Nanoparticle Monolayer and Multilayer Langmuir–Blodgett Films. *J. Mater. Chem.* **2012**, *22* (13), 6343. https://doi.org/10.1039/c2jm15797g.

(11) Okamoto, A.; Toda, S.; Hirakawa, M.; Bai, H.; Tanaka, M.; Seino, S.; Nakagawa, T.; Murakami, H. Narrowing of the Particle Size Distribution of InP Quantum Dots for Green Light Emission by Synthesis in Micro-Flow Reactor. *ChemistrySelect* **2022**, *7* (6), e202104215. https://doi.org/10.1002/slct.202104215.

(12) Borah, R.; Verbruggen, S. W. Effect of Size Distribution, Skewness and Roughness on the Optical Properties of Colloidal Plasmonic Nanoparticles. *Colloids and Surfaces A: Physicochemical and Engineering Aspects* **2022**, *640*, 128521. https://doi.org/10.1016/j.colsurfa.2022.128521.

(13) Wu, Z.; Yang, S.; Wu, W. Shape Control of Inorganic Nanoparticles from Solution. *Nanoscale* **2016**, *8* (3), 1237–1259. https://doi.org/10.1039/C5NR07681A.

(14) Ma, Z.; Mohapatra, J.; Wei, K.; Liu, J. P.; Sun, S. Magnetic Nanoparticles: Synthesis, Anisotropy, and Applications. *Chem. Rev.* **2023**, *123* (7), 3904–3943. https://doi.org/10.1021/acs.chemrev.1c00860.
(15) Pousthomis, M.; Anagnostopoulou, E.; Panagiotopoulos, I.; Boubekri, R.; Fang, W.; Ott, F.; Atmane, K. A.; Piquemal, J.-Y.; Lacroix, L.-M.; Viau, G. Localized Magnetization Reversal Processes in Cobalt Nanorods with Different Aspect Ratios. *Nano Res.* **2015**, *8* (7), 2231–2241. https://doi.org/10.1007/s12274-015-0734-x.
(16) Huang, X.; El-Sayed, I. H.; Qian, W.; El-Sayed, M. A. Cancer Cell Imaging and Photothermal Therapy in the Near-Infrared Region by Using Gold Nanorods. *J. Am. Chem. Soc.* **2006**, *128* (6), 2115–2120. https://doi.org/10.1021/ja057254a.
(17) Luo, T.; Meng, Q.-Q.; Gao, C.; Yu, X.-Y.; Jia, Y.; Sun, B.; Jin, Z.; Li, Q.-X.; Liu, J.-H.; Huang, X.-J. Sub-20 Nm-Fe_3O_4 Square and Circular Nanoplates: Synthesis and Facet-Dependent Magnetic and Electrochemical Properties. *Chem. Commun.* **2014**, *50* (100), 15952–15955. https://doi.org/10.1039/C4CC06064D.
(18) Nasilowski, M.; Mahler, B.; Lhuillier, E.; Ithurria, S.; Dubertret, B. Two-Dimensional Colloidal Nanocrystals. *Chem. Rev.* **2016**, *116* (18), 10934–10982. https://doi.org/10.1021/acs.chemrev.6b00164.
(19) Macfarlane, R. J.; Lee, B.; Jones, M. R.; Harris, N.; Schatz, G. C.; Mirkin, C. A. Nanoparticle Superlattice Engineering with DNA. *Science* **2011**, *334* (6053), 204–208. https://doi.org/10.1126/science.1210493.
(20) Pichon, B. P.; Gerber, O.; Lefevre, C.; Florea, I.; Fleutot, S.; Baaziz, W.; Pauly, M.; Ohlmann, M.; Ulhaq, C.; Ersen, O.; Pierron-Bohnes, V.; Panissod, P.; Drillon, M.; Begin-Colin, S. Microstructural and Magnetic Investigations of Wüstite-Spinel Core-Shell Cubic-Shaped Nanoparticles. *Chem. Mater.* **2011**, *23* (11), 2886–2900. https://doi.org/10.1021/cm2003319.
(21) Baaziz, W.; Pichon, B. P.; Lefevre, C.; Ulhaq-Bouillet, C.; Greneche, J.-M.; Toumi, M.; Mhiri, T.; Bégin-Colin, S. High Exchange Bias in $Fe_{3-\delta}O_4$@CoO Core Shell Nanoparticles Synthesized by a One-Pot Seed-Mediated Growth Method. *J. Phys. Chem. C* **2013**, *117* (21), 11436–11443. https://doi.org/10.1021/jp402823h.
(22) Joy, J.; Krishnamoorthy, A.; Tanna, A.; Kamathe, V.; Nagar, R.; Srinivasan, S. Recent Developments on the Synthesis of Nanocomposite Materials via Ball Milling Approach for Energy Storage Applications. *Applied Sciences* **2022**, *12* (18), 9312. https://doi.org/10.3390/app12189312.
(23) Gul, S.; Khan, S. B.; Rehman, I. U.; Khan, M. A.; Khan, M. I. A Comprehensive Review of Magnetic Nanomaterials Modern Day Theranostics. *Front. Mater.* **2019**, *6*, 179. https://doi.org/10.3389/fmats.2019.00179.
(24) Park, J.; Joo, J.; Kwon, S. G.; Jang, Y.; Hyeon, T. Synthesis of Monodisperse Spherical Nanocrystals. *Angew. Chem. Int. Ed.* **2007**, *46* (25), 4630–4660. https://doi.org/10.1002/anie.200603148.
(25) Park, J.; An, K.; Hwang, Y.; Park, J.-G.; Noh, H.-J.; Kim, J.-Y.; Park, J.-H.; Hwang, N.-M.; Hyeon, T. Ultra-Large-Scale Syntheses of Monodisperse Nanocrystals. *Nature Mater* **2004**, *3* (12), 891–895. https://doi.org/10.1038/nmat1251.
(26) Chang, H.; Kim, B. H.; Lim, S. G.; Baek, H.; Park, J.; Hyeon, T. Role of the Precursor Composition in the Synthesis of Metal Ferrite Nanoparticles. *Inorg. Chem.* **2021**, *60* (7), 4261–4268. https://doi.org/10.1021/acs.inorgchem.0c03567.
(27) Mrad, K.; Schoenstein, F.; Nong, H. T. T.; Anagnostopoulou, E.; Viola, A.; Mouton, L.; Mercone, S.; Ricolleau, C.; Jouini, N.; Abderraba, M.; Lacroix, L.-M.; Viau, G.; Piquemal, J.-Y. Control of the Crystal Habit and Magnetic Properties of Co Nanoparticles through the Stirring Rate. *CrystEngComm* **2017**, *19* (25), 3476–3484. https://doi.org/10.1039/C7CE00714K.
(28) Unni, M.; Uhl, A. M.; Savliwala, S.; Savitzky, B. H.; Dhavalikar, R.; Garraud, N.; Arnold, D. P.; Kourkoutis, L. F.; Andrew, J. S.; Rinaldi, C. Thermal Decomposition Synthesis of Iron Oxide Nanoparticles with Diminished Magnetic Dead Layer by Controlled Addition of Oxygen. *ACS Nano* **2017**, *11* (2), 2284–2303. https://doi.org/10.1021/acsnano.7b00609.

(29) Lynch, J.; Zhuang, J.; Wang, T.; LaMontagne, D.; Wu, H.; Cao, Y. C. Gas-Bubble Effects on the Formation of Colloidal Iron Oxide Nanocrystals. *J. Am. Chem. Soc.* **2011**, *133* (32), 12664–12674. https://doi.org/10.1021/ja2032597.
(30) Zhou, B. H.; Rinehart, J. D. Pseudo Spin Valve Behavior in Colloidally Prepared Nanoparticle Films. *ACS Appl. Electron. Mater.* **2019**, *1* (7), 1065–1069. https://doi.org/10.1021/acsaelm.9b00196.
(31) Kirkpatrick, K. M.; Zhou, B. H.; Bunting, P. C.; Rinehart, J. D. Size-Tunable Magnetite Nanoparticles from Well-Defined Iron Oleate Precursors. *Chem. Mater.* **2022**, *34* (17), 8043–8053. https://doi.org/10.1021/acs.chemmater.2c02046.
(32) Herman, D. A. J.; Cheong-Tilley, S.; McGrath, A. J.; McVey, B. F. P.; Lein, M.; Tilley, R. D. How to Choose a Precursor for Decomposition Solution-Phase Synthesis: The Case of Iron Nanoparticles. *Nanoscale* **2015**, *7* (14), 5951–5954. https://doi.org/10.1039/C5NR00718F.
(33) Bronstein, L. M.; Huang, X.; Retrum, J.; Schmucker, A.; Pink, M.; Stein, B. D.; Dragnea, B. Influence of Iron Oleate Complex Structure on Iron Oxide Nanoparticle Formation. *Chem. Mater.* **2007**, *19* (15), 3624–3632. https://doi.org/10.1021/cm062948j.
(34) Ali, A.; Shah, T.; Ullah, R.; Zhou, P.; Guo, M.; Ovais, M.; Tan, Z.; Rui, Y. Review on Recent Progress in Magnetic Nanoparticles: Synthesis, Characterization, and Diverse Applications. *Front. Chem.* **2021**, *9*, 629054. https://doi.org/10.3389/fchem.2021.629054.
(35) Perton, F.; Cotin, G.; Kiefer, C.; Strub, J.-M.; Cianferani, S.; Greneche, J.-M.; Parizel, N.; Heinrich, B.; Pichon, B.; Mertz, D.; Begin-Colin, S. Iron Stearate Structures: An Original Tool for Nanoparticles Design. *Inorg. Chem.* **2021**, acs.inorgchem.1c01689. https://doi.org/10.1021/acs.inorgchem.1c01689.
(36) Kovalenko, M. V.; Bodnarchuk, M. I.; Lechner, R. T.; Hesser, G.; Schäffler, F.; Heiss, W. Fatty Acid Salts as Stabilizers in Size- and Shape-Controlled Nanocrystal Synthesis: The Case of Inverse Spinel Iron Oxide. *J. Am. Chem. Soc.* **2007**, *129* (20), 6352–6353. https://doi.org/10.1021/ja0692478.
(37) Muro-Cruces, J.; Roca, A. G.; López-Ortega, A.; Fantechi, E.; del-Pozo-Bueno, D.; Estradé, S.; Peiró, F.; Sepúlveda, B.; Pineider, F.; Sangregorio, C.; Nogues, J. Precise Size Control of the Growth of Fe_3O_4 Nanocubes over a Wide Size Range Using a Rationally Designed One-Pot Synthesis. *ACS Nano* **2019**, *13* (7), 7716–7728. https://doi.org/10.1021/acsnano.9b01281.
(38) Willis, A. L.; Chen, Z.; He, J.; Zhu, Y.; Turro, N. J.; O'Brien, S. Metal Acetylacetonates as General Precursors for the Synthesis of Early Transition Metal Oxide Nanomaterials. *Journal of Nanomaterials* **2007**, *2007*, 1–7. https://doi.org/10.1155/2007/14858.
(39) Cotin, G.; Kiefer, C.; Perton, F.; Ihiawakrim, D.; Blanco-Andujar, C.; Moldovan, S.; Lefevre, C.; Ersen, O.; Pichon, B.; Mertz, D.; Bégin-Colin, S. Unravelling the Thermal Decomposition Parameters for The Synthesis of Anisotropic Iron Oxide Nanoparticles. *Nanomaterials* **2018**, *8* (11), 881. https://doi.org/10.3390/nano8110881.
(40) Narnaware, P. K.; Ravikumar, C. Mechanistic Insights into the Formation and Growth of Anisotropic-Shaped Wüstite–Spinel Core–Shell Iron Oxide Nanoparticles in a Coordinating Solvent. *J. Phys. Chem. C* **2020**, *124* (45), 25010–25027. https://doi.org/10.1021/acs.jpcc.0c05606.
(41) Ammar, S.; Fiévet, F. Polyol Synthesis: A Versatile Wet-Chemistry Route for the Design and Production of Functional Inorganic Nanoparticles. *Nanomaterials* **2020**, *10* (6), 1217. https://doi.org/10.3390/nano10061217.
(42) Bruvera, I. J.; Mendoza Zélis, P.; Pilar Calatayud, M.; Goya, G. F.; Sánchez, F. H. Determination of the Blocking Temperature of Magnetic Nanoparticles: The Good, the Bad, and the Ugly. *Journal of Applied Physics* **2015**, *118* (18), 184304. https://doi.org/10.1063/1.4935484.
(43) Vieru, V.; Gómez-Coca, S.; Ruiz, E.; Chibotaru, L. F. Increasing the Magnetic Blocking Temperature of Single-Molecule Magnets. *Angew Chem Int Ed* **2023**, e202303146. https://doi.org/10.1002/anie.202303146.
(44) Baaziz, W.; Pichon, B. P.; Grenèche, J.-M.; Begin-Colin, S. Effect of Reaction Environment and *in Situ* Formation of the Precursor on the Composition and Shape of Iron Oxide Nanoparticles Synthesized by the Thermal Decomposition Method. *CrystEngComm* **2018**, *20* (44), 7206–7220. https://doi.org/10.1039/C8CE00875B.

(45) Mamiya, H.; Fukumoto, H.; Cuya Huaman, J. L.; Suzuki, K.; Miyamura, H.; Balachandran, J. Estimation of Magnetic Anisotropy of Individual Magnetite Nanoparticles for Magnetic Hyperthermia. *ACS Nano* **2020**, *14* (7), 8421–8432. https://doi.org/10.1021/acsnano.0c02521.
(46) Wetterskog, E.; Tai, C.-W.; Grins, J.; Bergström, L.; Salazar-Alvarez, G. Anomalous Magnetic Properties of Nanoparticles Arising from Defect Structures: Topotaxial Oxidation of $Fe_{1-x}O|Fe_{3-\delta}O_4$ Core|Shell Nanocubes to Single-Phase Particles. *ACS Nano* **2013**, *7* (8), 7132–7144. https://doi.org/10.1021/nn402487q.
(47) Salazar-Alvarez, G.; Qin, J.; Šepelák, V.; Bergmann, I.; Vasilakaki, M.; Trohidou, K. N.; Ardisson, J. D.; Macedo, W. A. A.; Mikhaylova, M.; Muhammed, M.; Baró, M. D.; Nogués, J. Cubic versus Spherical Magnetic Nanoparticles: The Role of Surface Anisotropy. *J. Am. Chem. Soc.* **2008**, *130* (40), 13234–13239. https://doi.org/10.1021/ja0768744.
(48) Hadadian, Y.; Masoomi, H.; Dinari, A.; Ryu, C.; Hwang, S.; Kim, S.; Cho, B. ki; Lee, J. Y.; Yoon, J. From Low to High Saturation Magnetization in Magnetite Nanoparticles: The Crucial Role of the Molar Ratios Between the Chemicals. *ACS Omega* **2022**, *7* (18), 15996–16012. https://doi.org/10.1021/acsomega.2c01136.
(49) Wu, K.; Saha, R.; Su, D.; Krishna, V. D.; Liu, J.; Cheeran, M. C.-J.; Wang, J.-P. Magnetic-Nanosensor-Based Virus and Pathogen Detection Strategies before and during COVID-19. *ACS Appl. Nano Mater.* **2020**, *3* (10), 9560–9580. https://doi.org/10.1021/acsanm.0c02048.
(50) Lapitan, L. D. S.; Xu, Y.; Guo, Y.; Zhou, D. Combining Magnetic Nanoparticle Capture and Poly-Enzyme Nanobead Amplification for Ultrasensitive Detection and Discrimination of DNA Single Nucleotide Polymorphisms. *Nanoscale* **2019**, *11* (3), 1195–1204. https://doi.org/10.1039/C8NR07641C.
(51) Wallyn; Anton; Vandamme. Synthesis, Principles, and Properties of Magnetite Nanoparticles for In Vivo Imaging Applications—A Review. *Pharmaceutics* **2019**, *11* (11), 601. https://doi.org/10.3390/pharmaceutics11110601.
(52) Gale, E. M.; Caravan, P. Gadolinium-Free Contrast Agents for Magnetic Resonance Imaging of the Central Nervous System. *ACS Chem. Neurosci.* **2018**, *9* (3), 395–397. https://doi.org/10.1021/acschemneuro.8b00044.
(53) Gao, S.; Chen, M.-L.; Zhou, Z.-H. Substitution of Gadolinium Ethylenediaminetetraacetate with Phosphites: Towards Gadolinium Deposit in Nephrogenic Systemic Fibrosis. *Dalton Trans.* **2014**, *43* (2), 639–645. https://doi.org/10.1039/C3DT52015C.
(54) Yu, E. Y.; Bishop, M.; Zheng, B.; Ferguson, R. M.; Khandhar, A. P.; Kemp, S. J.; Krishnan, K. M.; Goodwill, P. W.; Conolly, S. M. Magnetic Particle Imaging: A Novel in Vivo Imaging Platform for Cancer Detection. *Nano Lett.* **2017**, *17* (3), 1648–1654. https://doi.org/10.1021/acs.nanolett.6b04865.
(55) Wang, Q.; Ma, X.; Liao, H.; Liang, Z.; Li, F.; Tian, J.; Ling, D. Artificially Engineered Cubic Iron Oxide Nanoparticle as a High-Performance Magnetic Particle Imaging Tracer for Stem Cell Tracking. *ACS Nano* **2020**, *14* (2), 2053–2062. https://doi.org/10.1021/acsnano.9b08660.
(56) Kemp, S. J.; Ferguson, R. M.; Khandhar, A. P.; Krishnan, K. M. Monodisperse Magnetite Nanoparticles with Nearly Ideal Saturation Magnetization. *RSC Adv.* **2016**, *6* (81), 77452–77464. https://doi.org/10.1039/C6RA12072E.
(57) Shingte, S. D.; Phakatkar, A. H.; McKiernan, E.; Nigoghossian, K.; Ferguson, S.; Shahbazian-Yassar, R.; Brougham, D. F. Correlating Magnetic Hyperthermia and Magnetic Resonance Imaging Contrast Performance of Cubic Iron Oxide Nanoparticles with Crystal Structural Integrity. *Chem. Mater.* **2022**, acs.chemmater.2c00708. https://doi.org/10.1021/acs.chemmater.2c00708.
(58) Castellanos-Rubio, I.; Arriortua, O.; Iglesias-Rojas, D.; Barón, A.; Rodrigo, I.; Marcano, L.; Garitaonandia, J. S.; Orue, I.; Fdez-Gubieda, M. L.; Insausti, M. A Milestone in the Chemical Synthesis of Fe3O4 Nanoparticles: Unreported Bulklike Properties Lead to a Remarkable Magnetic Hyperthermia. *Chem. Mater.* **2021**, *33* (22), 8693–8704.
(59) Cotin, G.; Perton, F.; Blanco-Andujar, C.; Pichon, B.; Mertz, D.; Bégin-Colin, S. Design of Anisotropic Iron-Oxide-Based Nanoparticles for Magnetic Hyperthermia. In *Nanomaterials for*

Magnetic and Optical Hyperthermia Applications; Elsevier, 2019; pp 41–60. https://doi.org/10.1016/B978-0-12-813928-8.00002-8.

(60) Castellanos-Rubio, I.; Arriortua, O.; Marcano, L.; Rodrigo, I.; Iglesias-Rojas, D.; Barón, A.; Olazagoitia-Garmendia, A.; Olivi, L.; Plazaola, F.; Fdez-Gubieda, M. L.; Castellanos-Rubio, A.; Garitaonandia, J. S.; Orue, I.; Insausti, M. Shaping Up Zn-Doped Magnetite Nanoparticles from Mono- and Bimetallic Oleates: The Impact of Zn Content, Fe Vacancies, and Morphology on Magnetic Hyperthermia Performance. *Chem. Mater.* **2021**, *33* (9), 3139–3154.

(61) Baibich, M. N.; Broto, J. M.; Fert, A.; Van Dau, F. N.; Petroff, F.; Etienne, P.; Creuzet, G.; Friederich, A.; Chazelas, J. Giant Magnetoresistance of (001)Fe/(001)Cr Magnetic Superlattices. *Phys. Rev. Lett.* **1988**, *61* (21), 2472–2475. https://doi.org/10.1103/PhysRevLett.61.2472.

(62) Ennen, I.; Kappe, D.; Rempel, T.; Glenske, C.; Hütten, A. Giant Magnetoresistance: Basic Concepts, Microstructure, Magnetic Interactions and Applications. *Sensors* **2016**, *16* (6), 904. https://doi.org/10.3390/s16060904.

(63) Reig, C.; Cubells-Beltrán, M.-D.; Ramírez Muñoz, D. Magnetic Field Sensors Based on Giant Magnetoresistance (GMR) Technology: Applications in Electrical Current Sensing. *Sensors* **2009**, *9* (10), 7919–7942. https://doi.org/10.3390/s91007919.

(64) Reig, C.; Cardoso, S.; Mukhopadhyay, S. C. *Giant Magnetoresistance (GMR) Sensors*; Smart Sensors, Measurement and Instrumentation; Springer Berlin Heidelberg: Berlin, Heidelberg, 2013; Vol. 6. https://doi.org/10.1007/978-3-642-37172-1.

(65) Krishna, V. D.; Wu, K.; Perez, A. M.; Wang, J.-P. Giant Magnetoresistance-Based Biosensor for Detection of Influenza A Virus. *Front. Microbiol.* **2016**, *7*. https://doi.org/10.3389/fmicb.2016.00400.

(66) Adem, S.; Jain, S.; Sveiven, M.; Zhou, X.; O'Donoghue, A. J.; Hall, D. A. Giant Magnetoresistive Biosensors for Real-Time Quantitative Detection of Protease Activity. *Sci Rep* **2020**, *10* (1), 7941. https://doi.org/10.1038/s41598-020-62910-2.

(67) Su, D.; Wu, K.; Saha, R.; Peng, C.; Wang, J.-P. Advances in Magnetoresistive Biosensors. *Micromachines* **2019**, *11* (1), 34. https://doi.org/10.3390/mi11010034.

(68) Famiani, S.; LaGrow, A. P.; Besenhard, M. O.; Maenosono, S.; Thanh, N. T. K. Synthesis of Fine-Tuning Highly Magnetic Fe@Fe_xO_y Nanoparticles through Continuous Injection and a Study of Magnetic Hyperthermia. *Chem. Mater.* **2018**, *30* (24), 8897–8904. https://doi.org/10.1021/acs.chemmater.8b04056.

Chapter 2

Size-Tunable Magnetite Nanoparticles from Well-Defined Iron Oleate Precursors

2.1 Introduction

The synthesis of iron oxide nanoparticles with fine control over size and shape has been a long-studied area of research, with iron oleate being arguably the most successful precursor. Issues with reproducibility and versatility in iron oleate-based syntheses remain, however, in large part due to the mutable nature of its structure and stoichiometry. In this chapter, two new forms of iron oleate precursor are presented that can be isolated in large quantities, show long-term stability, and have well-defined stoichiometry, leading to reproducible and predictable reactivity. Synthesis with these precursors is shown to produce iron oxide nanoparticles in a tunable size range of 4-16 nm with low size dispersity and properties consistent with magnetite in the superparamagnetic size-regime.

The thermal decomposition of metal coordination complexes is a longstanding and commonly employed technique to produce colloidal nanoparticles.[1–4] Complexes formed from transition metals and the oleate anion (Ol^- = $CH_3(CH_2)_7CH{=}CH(CH_2)_7COO^-$) are one of the most common precursors for nanoparticles, providing access to a wide variety of metal oxide (e.g., CoO,[5,6] MnO,[7] ZnO[8]) and metal ferrite (e.g., MFe_2O_4 (M = Fe, Co, Ni, Mn, Zn))[9–11] materials. Perhaps the greatest testament to the utility of the oleate precursor is its continued dominance, despite persistent issues in reproducibility and predictability. Much of this variability arises from the fact that the term "metal oleate" rarely refers to an exact molecular formula. Indeed, there is significant evidence that metal oleates are highly variable materials where ligation, nuclearity, solvation, and oxidation state are sensitive to a host of synthetic details.[12,13] This sensitivity

presents a challenge to sample-to-sample consistency, inhibiting predictive and scalable control over nanoparticle size, size dispersity, morphology, and phase. Often, even small alterations to a functioning synthesis require extensive re-optimization. Once optimized, however, control over nanoparticle phase, size, and shape has been demonstrated to impressive levels of precision.[13–16] While the issues arising from precursor variability are a common challenge amongst nanoparticle syntheses, reliable methods are especially vital for magnetic nanomaterials. Even slight variations in phase, morphology, homogeneity, and heterostructure can limit or even negate their functional magnetic cabilities.[17] Especially with iron oxide, these capabilities are vital for optimizing responses in applications such as magnetic hyperthermia,[11,18] nanocomposite magnetoresistance,[19–23] smart fluids,[24] magnetic particle imaging,[25–27] magnetic particle spectroscopy,[28,29] and thermometry.[30,31]

Many syntheses for iron oxide nanoparticles have been explored from a host of precursors including long chain carboxylates (oleate,[2,12] stearate,[32–34] palmitate[16]), acetate,[35,36] acetylacetonate,[1,37] carbonyl,[38] carbonate,[39] and hydroxide ligands.[40,41] Amongst the many demonstrated precursor materials, iron oleate is arguably the most popular, as it is non-toxic, can be made on a large scale,[2] and has been shown to produce particles of a variety of sizes (d = 1 – 40 nm),[13,14] with considerable shape control.[15,16]

Many research groups,[10,12,14,42] including our own,[23] have reported structural and magnetic data for magnetite nanoparticles using iron oleate syntheses, yet, somewhat counterintuitively, these syntheses continue to have challenges. The formulations of the iron oleate used as a synthetic precursor to magnetic nanoparticles has been shown, through careful characterization, to be highly sensitive to minor variations in its synthesis due to its propensity to retain water, oleic acid and other reaction byproducts.[12,43,44]

Herein, we compare our standard preparation of the viscous red-brown oil typically characterized as iron oleate (FeOl-1), to two newly isolated iron oleate starting materials: a fine dark brown powder preparation (FeOl-2) and a hard, waxy preparation (FeOl-3) (Figure 2.1). Similar to FeOl-1, FeOl-2–3 lack crystallographic order, yet are compositionally more consistent, and upon thermal decomposition, lead to low size dispersity nanoparticles in a systematic and tunable size range of 4-16 nm. In this work, we detail the synthetic methods and characterization of these new precursors for the thermal decomposition synthesis

of magnetite nanoparticles. Additionally, we discuss the possible advantages of using FeOl-2–3 in nanoparticle synthesis in the context of both practical synthetic methods and the resulting magnetism. A general reaction scheme for the synthesis of each iron oleate precursor described in this work is depicted in Figure 2.1.

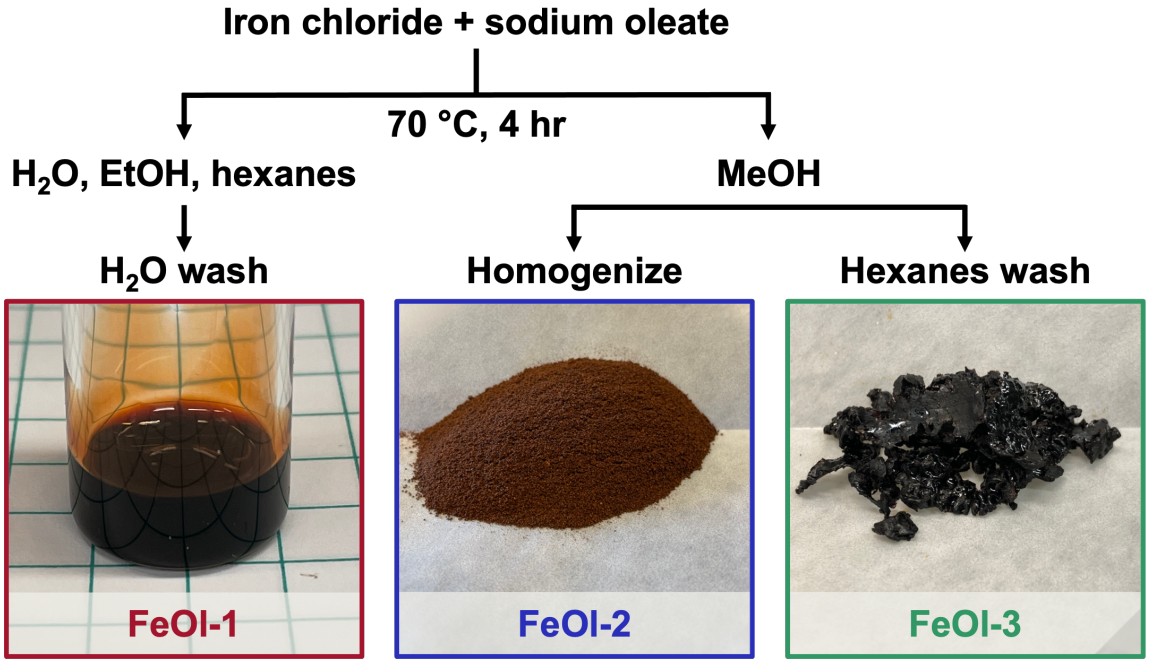

Figure 2.1. Abbreviated reaction scheme and representative images of iron oleate precursors.

2.2 Results and discussion

2.2.1 Synthesis and physical characterization of iron oleate precursors

The oleate precursor for the synthesis of iron oxide nanoparticles is generally agreed to contain the ubiquitous trinuclear oxo-centered iron motif, $[Fe_3O]^{n+}$, with charge balance provided by chelating oleate ligation.[10] Since there are countless variations on iron oleate syntheses, we use the general name FeOl-1 as a means to delineate observations based on procedures and characterization described herein for comparison with the materials FeOl-2 and FeOl-3.

Synthesis for FeOl-1 proceeds by stirring a solution of iron (III) chloride and sodium oleate in deionized (DI) water, ethanol, and hexanes at 70 °C for four hours (Figure 2.1).[2] Afterwards, the hexanes phase containing FeOl-1 is washed with DI water using a separatory funnel. The hexanes are removed under reduced pressure until the highly viscous, dark red oil (FeOl-1) is obtained. Literature procedures for this synthesis vary greatly and offer insight into how the starting material formulation can affect the resultant nanoparticle properties.

Unlike a well-defined, crystalline molecular structure, the connectivity and composition of FeOl-1 can change dramatically during synthesis and workup as a result of reflux temperature, reaction solvent, volume of solvent, degree of diligence in byproduct extraction, and method of solvent removal. For instance, the reported reflux temperature from syntheses similar to FeOl-1 varies from 57 °C to 70 °C,[2,14] with this variability exhibiting important consequences on the resultant nanoparticles. Bronstein et al. have also demonstrated the partial removal of free/residual oleic acid (OA) from syntheses similar to FeOl-1, indicating a high potential for variability in stoichiometry.[12]

Additionally, the charge of the trinuclear iron-oxo cluster leads to further inconsistency. The mixed valence cluster $[Fe_3O]^{6+}$ leads to a net neutral molecule with 6 oleate anions, yet x-ray photoelectron spectroscopy (XPS) on material from syntheses similar to FeOl-1 is consistent with an all Fe^{3+} core.[12] To further support this, the net charge of the iron-oxo core can be probed by peaks in the 500-650 cm^{-1} region of an infrared (IR) spectrum.[10] Analysis of molecular iron-oxo clusters indicates that an all Fe^{3+} core exhibiting D_{3h} symmetry will show a peak at ~ 610 cm^{-1}, which we indeed observe in FeOl-1 (Figure 2.2c). Therefore, the $[Fe_3O]^{7+}$ cluster core predicted for FeOl-1 has uncompensated cationic charge, most likely resulting in anionic outer sphere oleate.

In addition to residual anionic oleate present in FeOl-1, residual OA is also incorporated due to the nature of the biphasic synthesis, evident by the peak at ~ 1710 cm^{-1} in its IR spectrum (Figure 2.2b). Combined with residual OA present in the material, even in a purified form, FeOl-1 contains minimum excess ligand of roughly 30% by mass. Determining the carbon and hydrogen percentages through elemental analysis (EA) and iron percentage through inductively coupled plasma mass spectrometry (ICP-

MS), FeOl-1 matches the formula of $[Fe_3O(oleate)_6][oleate]\cdot(oleic\ acid)_2\cdot H_2O$ (Table 2.1), as noted by others.[12,13] This composition, however, has been shown to vary as a function of storage, reaction, and workup conditions. Additionally, some syntheses use stoichiometries based on an assumed formula of $Fe_3O(oleate)_6$ or $Fe(oleate)_3$, leading to higher uncertainty in the metal to ligand ratios. Typical nanoparticle syntheses add OA as a surfactant and because of the viscous and cationic nature of the core cluster in FeOl-1, it is very difficult to fully separate from free OA, oleate anions, residual sodium, and other solvents. Thus, reproducing metal to surfactant ratios across different batches of starting material and in different laboratories is a recurring challenge.

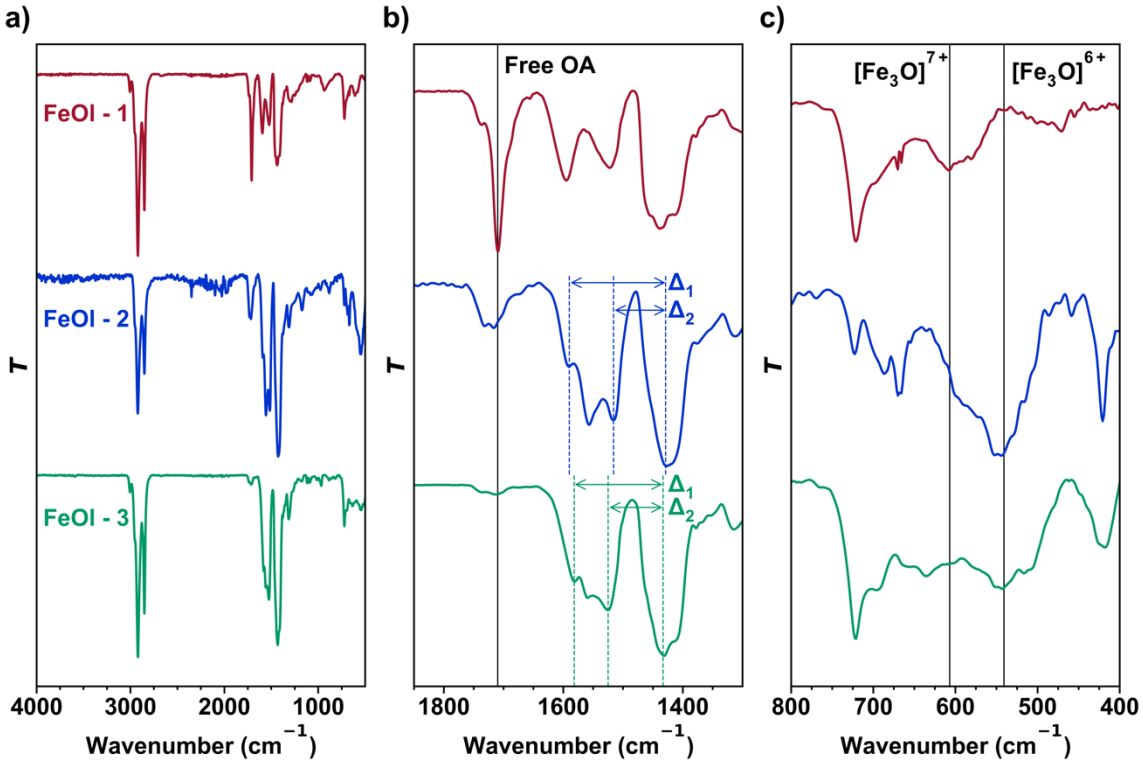

Figure 2.2. Infrared characterization of iron oleate precursors plotted as wavenumber (cm^{-1}) vs. normalized transmittance. (a) Full infrared spectra. (b) Carboxylate region with free/residual oleic acid (OA) indicated at 1710 cm^{-1}. (c) Metal-oxo core region with $[Fe_3O]^{n+}$ cluster peaks indicated at 610 cm^{-1} (n = 7) and 545 cm^{-1} (n = 6).

The drying step contains two other seemingly innocuous variables that lead to reproducibility issues. Multiple studies have analyzed the impact of drying time and temperature on the metal-carboxylate binding mode distribution from syntheses similar to FeOl-1.[12,18,43,44] Balakrishnan et al. observed

diminishing signal from free OA with increased drying times, attributing it in part to the removal of crystal hydrate water.[44] This change in the binding mode distribution led to a dramatic change in the resulting nanoparticles, from 6 nm to 13 nm for drying times of 5 d and 30 d, respectively.[44] Although the drying step represents a convenient parameter to tune the size in this case, a precursor that changes its composition over time is not ideal.

Table 2.1. Elemental composition of iron oleate precursors with corresponding formulas.

Sample	C	H	Fe
FeOl-1	71.19 ± 0.08	10.50 ± 0.31	6.51 ± 0.72
$[Fe_3O(oleate)_6][oleate] \cdot (oleic\ acid)_2 \cdot H_2O$	71.10	11.09	6.12
FeOl-2	62.34 ± 0.01	9.22 ± 0.02	15.27 ± 1.20
$Fe_3O\ C_{55}H_{103}O_7$	62.32	9.8	15.81
FeOl-3	67.42 ± 0.11	10.31 ± 0.01	9.40 ± 0.62
$Fe_3O(oleate)_6 \cdot 3H_2O$	67.34	10.67	8.70

Initial attempts to obtain a simplified formulation of FeOl-1 resulted in promising results from syntheses proceeding in organic solvents, specifically in methanol (MeOH). An optimized procedure was developed wherein FeOl-2 was prepared in a sealed Ace pressure vessel by stirring iron (III) chloride and sodium oleate in MeOH at 70 °C, followed by washing with DI water, homogenization of the resulting solid, and drying. A detailed step-by-step demonstration for the synthesis of FeOl-2 with photos is shown in Figure 2.3. Via this procedure, FeOl-2 is isolated as an air-stable powder on gram scale quantities.

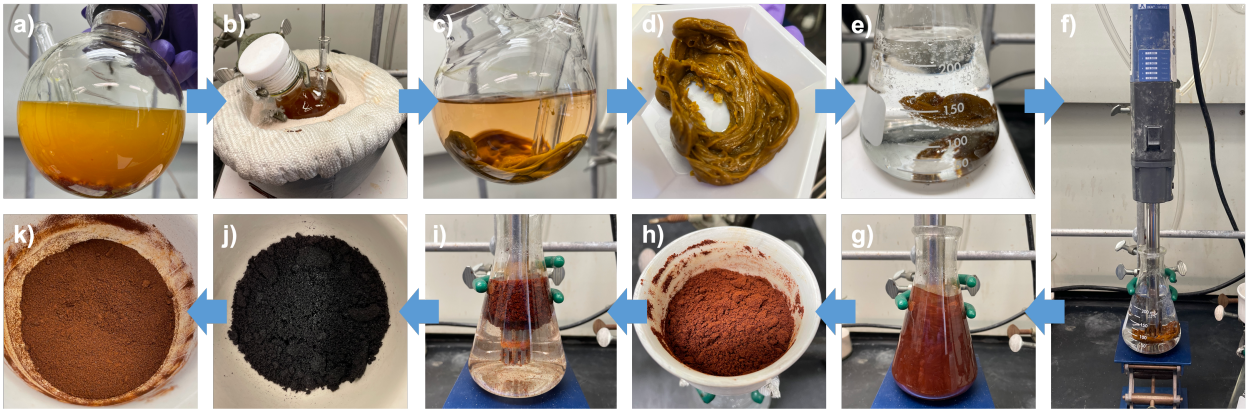

Figure 2.3. Step by step synthesis of FeOl-2. (a) Combined reactants in pressure flask. (b) Setup of flask in heating mantle. (c) Reaction end. (d) Rubbery solid resulting from the reaction. (e) Solid in ~ 250 mL DI water in 250 mL Erlenmeyer flask. (f) Tissue homogenizer inserted into flask. (g) Homogenization. (h) Product recovered after vacuum filtration. (i) Second homogenization (product floats to surface when not running homogenizer) (j) Dried 24 h in vacuum oven, then crushed with pestle. (k) Final product, FeOl-2, after additional 24 h in vacuum oven.

A small degree of variability (Fe:OA ratio) in the FeOl-2 composition was discovered, likely due to differences in vacuum oven conditions and/or exposure to air in the vacuum oven. The observed changes in the Fe:OA ratio can result in a slightly different nanoparticle size (± 2 nm) from the intended size. This result with FeOl-1, however, still represents a significant improvement over FeOl-1, as one can follow an iterative process by systematically adjusting reaction conditions (Fe %, Fe:OA) to synthesize a given size.

Homogenization in aqueous suspension was used to break up the tough rubbery clumps formed upon initially isolating the reaction mixture from MeOH (Figure 2.1). The thorough aqueous homogenization was found to be crucial for the removal of residual sodium chloride and sodium oleate, as confirmed by powder x-ray diffraction analysis (Figure 2.10). Following collection of the solid via vacuum filtration and drying (70 °C, 24 h, house vacuum), FeOl-2 was isolated as a fine, dark brown powder (Figure 2.1) and used in nanoparticle syntheses without further purification. Importantly, FeOl-2 is found to be a convenient nanoparticle starting material, as it can be synthesized with consistent stoichiometry and readily converts to $Fe_3O(oleate)_6$ in the presence of excess OA (e.g., in precursor solutions for magnetite nanoparticles).

With FeOl-1 leading to a viscous oil and FeOl-2 an insoluble powder, we sought methods to pinpoint key differences in composition, connectivity, and/or oxidation state. As in FeOl-1, IR spectroscopy

was used to probe the metal-carboxylate binding modes. The IR spectrum of FeOl-2 was found to be similar to FeOl-1, with metal-carboxylate peaks corresponding to symmetric and asymmetric stretching modes presenting in the region between 1300 cm^{-1} and 1800 cm^{-1} (Figure 2.2).[12] Four binding configurations are possible: ionic, monodentate, bridging, and bidentate, with the latter two most commonly observed. The most probable binding mode can be predicted by the difference (Δ) between the symmetric and asymmetric peaks, with Δ = 140 - 200 cm^{-1} corresponding to a bridging mode and Δ < 110 cm^{-1} corresponding to a bidentate mode.[12] Via this analysis, FeOl-2 exhibits bridging (1592 cm^{-1}, Δ_1 = 163 cm^{-1}) and bidentate modes (1514 cm^{-1}, Δ_2 = 85 cm^{-1}), varying significantly from the IR spectrum of FeOl-1. Bronstein et al. observed a similar IR spectrum after washing with acetone and ethanol, attributing the change in Δ to a more regular packing of the oleate ligands following the removal of free OA.[12] Notably, FeOl-2 lacks a free OA carbonyl peak at 1710 cm^{-1} when fully purified. This spectroscopic signature can be used to prevent stoichiometric errors due to variable free OA, which can be difficult to remove from FeOl-1.

While FeOl-1 exhibits a strong peak at ~ 610 cm^{-1} corresponding to a $[Fe_3O]^{7+}$ core, FeOl-2 exhibits a shifted peak at ~ 550 cm^{-1}, suggesting a localized mixed valence $[Fe_3O]^{6+}$ core.[10] Although not definitive evidence of the valence state, this shift is consistent with the local symmetry lowering from (pseudo) D_{3h} *to* C_{2v} expected for reduction at a single metal center.

Given the possibility of a partially reduced metal cluster core, we were interested in exploring whether FeOl-2 formed via a more complex reactivity than expected. The $[Fe_3O]^{6+}$ motif has been shown to be catalytically active and convert olefinic alcohol acetates into epoxides, likely forming aldehydes in the process.[45,46] To probe the importance of reactivity of olefins in the presence of $[Fe_3O]^{6+}$, the elemental composition of FeOl-2 was analyzed by EA and ICP-MS (Table 2.1). The Fe:C ratio for FeOl-2 (1:18), was well below than expected for $Fe_3O(oleate)_6$ (1:36), consistent with an irreversible loss of oleate or a breakdown of oleate into a smaller carboxylate. The redox activity of the iron-oxo cluster is consistent with some mechanisms for this oleate reactivity. Interestingly, such reactivity could be very difficult to characterize for in situ preparations or preparations where significant excess oleate is present, and thus could contribute to general reproducibility issues in many oleate based precursors.[39]

To further probe the reactivity of the $[Fe_3O]^{6+}$ cluster, we used headspace gas chromatography – mass spectrometry (GC-MS) experiments to monitor for any gaseous byproducts (e.g., aldehydes) released during the synthesis of iron oxide nanoparticles. FeOl-2 was reacted with OA in a GC vial and heated to 70 °C, simulating the degas step prior to a typical nanoparticle reaction. The vial headspace was sampled for 10 min at 70 °C and corrected for a background of neat OA. The chromatograph (Figure 2.11) shows the formation of aldehydes in sequential sizes, ranging from pentanal to nonanal. An identical experiment was performed with FeOl-1 in OA. Again, aldehydes ranging from C_5 to C_9 are observed (Figure 2.12). Cleavage of the alkene in OA likely proceeds through an epoxidation step at the trinuclear iron-oxo cluster, followed by addition of water, forming a di-alcohol.[47,48] Finally, the di-alcohol can be oxidized to an aldehyde by ambient oxygen. The GC-MS experiments demonstrate the redox activity of iron oleate based precursors in ligand decomposition reactions. These results bolster synthetic methods that include complete removal of water and oxygen from the system at low temperatures to minimize reactivity from uncontrolled side reactions catalyzed by metal-oxo cluster reagents.

To test the batch-to-batch reproducibility, the synthesis of FeOl-2 was performed in triplicate using the standardized procedure. The metal carboxylate behavior and elemental composition of the three batches were analyzed via IR and ICP/EA, respectively. The peaks in the IR spectra are functionally identical (Figure 2.13) and the elemental composition remains quite similar (Table 2.3), with a %RSD of 1.7, 0.50, and 1.6 for the percentages of Fe, C, and H, respectively.

Although non-crystalline, FeOl-2 is a free-flowing powder that can be made reproducibly with well-defined molar ratios and is thus amenable for use as a starting material. From a synthetic standpoint, a powder is simple to manipulate. FeOl-2 is air-stable and can be made in large quantities, enabling a potential scale-up of the nanoparticle reaction. After storage in air for six months, FeOl-2 exhibits a nearly identical IR spectrum (Figure 2.14), demonstrating a high degree of air-stability, however, considering the reactivity of the $[Fe_3O]^{6+}$ cluster, storage of FeOl-2 under inert atmosphere is preferred.

Finally, owing to its extended solid properties, FeOl-2 is highly insoluble in common organic solvents. However, it reacts with OA and mild heat (70 °C), allowing for dissolution in hexanes. This

permits characterization by matrix-assisted laser desorption/ionization mass spectrometry (MALDI-MS) for a detailed investigation into its cluster size and molecular weight with minimal fragmentation. The MALDI-MS spectrum of FeOl-2 in OA (Figure 2.4a) exhibits peaks corresponding to the expected trinuclear iron-oxo cluster, $Fe_3O(oleate)_6$. The molecular cluster $[Fe_3O(oleate)_6]^+$ is observed at 1872 Da (Figure 2.4b). Further confirming the assignment, the fragments $[Fe_3O(oleate)_5]^+$ and $[Fe_3O(oleate)_4]^+$ at 1570 Da and 1320 Da, respectively, are observed due to the sequential loss of oleate ligands.

These data are consistent with the idea that, following introduction of OA and mild heating, FeOl-2 is converted in situ to a form similar to that of FeOl-1 in a nanoparticle synthesis. This "activation" process of FeOl-2 extends to other carboxylic acids. For example, heating FeOl-2 with lauric acid in hexanes, shows the presence of $Fe_3O(laurate)_6$ by MALDI-MS (Figure 2.15). Considering the characterization of the material conducted thus far, we propose FeOl-2 to be an extended solid based on $[Fe_3O]^{6+}$ clusters bound by carboxylates, and capable of in situ activation by OA for the synthesis of iron oxide nanoparticles.

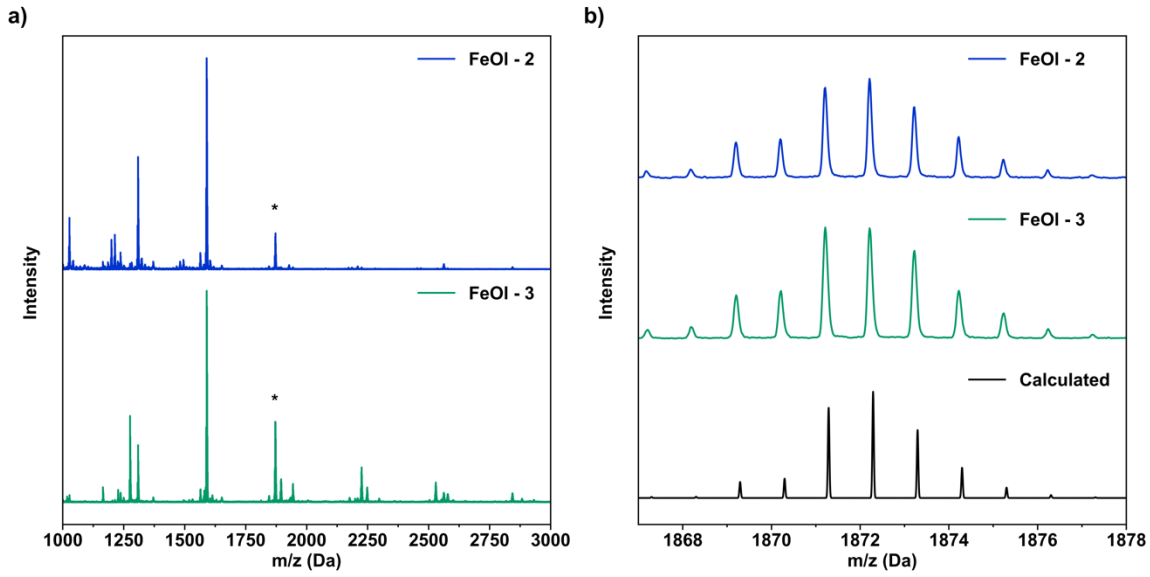

Figure 2.4. Molecular cluster structural data from MALDI-MS plotted as intensity vs. m/z. (a) Full MALDI-MS spectra of FeOl-2–3. The asterisk indicates the m/z value of the $[Fe_3O(oleate)_6]^+$ ion. (b) Zoomed in view of the asterisk-marked molecular ions of FeOl-2–3 compared to the calculated isotope pattern of $[Fe_3O(oleate)_6]^+$.

While storage and preparation were simplified by the insolubility of FeOl-2, extra care is required during the workup procedure to remove impurities. Achieving a soluble $Fe_3O(oleate)_6$ cluster in the initial

reaction mixture was likely to simplify purification from byproducts and residual salts. To do this, an identical procedure to that of FeOl-2 was followed with a mixture of iron (III) chloride and iron (II) chloride (2:1). The oily solid product of this reaction could be dissolved in hexanes, making a single aqueous wash usually sufficient for removing impurities. Hexanes was removed under reduced pressure to form a dark brown waxy solid (FeOl-3;Figure 2.1). Solid FeOl-3 was found to be suitable for synthesis directly or via formation of an octadecene stock solution for more convenient manipulation. The stock solution can be made by octadecene addition to FeOl-3 or octadecene addition directly to the hexane solution isolated after washing with water.

The IR spectrum of FeOl-3 exhibits similar peaks to FeOl-2, with a bridging mode at 1580 cm^{-1} ($\Delta_1 = 150\ cm^{-1}$) and a bidentate mode at 1526 cm^{-1} ($\Delta_2 = 96\ cm^{-1}$). The free OA peak near 1710 cm^{-1} is almost entirely absent. Additionally, IR data suggests the iron-oxo core of FeOl-3 is mixed valence, $[Fe_3O]^{6+}$, due to the observation of a peak observed at 550 cm^{-1}.[10]

In contrast with the insolubility of FeOl-2, FeOl-3 is soluble in hexanes and can be analyzed by MALDI-MS directly to determine the cluster size and molecular weight. The MALDI-MS data indicates that FeOl-3 consists of the trinuclear iron-oxo cluster, $Fe_3O(oleate)_6$, matching the calculated molecular ion at 1872 Da (Figure 2.4a). The two subsequent fragments at 1570 Da and 1320 Da are due to the loss of sequential oleates, confirming this assignment (Figure 2.4b).

Elemental analysis (Table 2.1) closely matches a solvated formula of $Fe_3O(oleate)_6 \cdot 3H_2O$. With these data, the assignment of FeOl-3 to a mixed-valence, trinuclear iron-oxo cluster, $Fe_3O(oleate)_6$, with no residual free oleic acid or anionic oleate is corroborated by elemental, IR, and MS analysis.

Both FeOl-2 and FeOl-3 provide practical advantages as starting materials for magnetic nanoparticle synthesis. There are still details of their structure and reactivity to explore, and we continue to do so. Their ultimate utility, however, lies in whether the observed stability and well-defined stoichiometry can be leveraged to enhance control over size and phase purity in iron oxide (especially magnetite) synthesis.

2.3 Synthesis and physical characterization of iron oxide nanoparticles

The synthesis of iron oxide nanoparticles from FeOl-2 is adapted from literature procedures with modification (Figure 2.5).[2,23,42] The Rinehart Group (Ben Zhou) previously observed an improvement in nanoparticle size dispersity with the use of Morton flasks instead of round bottom flasks, as they contain baffles that increase the turbulence in the reaction. The nanoparticle reactions are typically performed in 50 mL 3-neck Morton flasks with a temperature probe (left neck), short Liebig condenser, (middle neck), and a flow adapter (right). The reaction is heated with a heating mantle tightly wrapped around the bottom of the flask. The flask is centered on the hot plate, as proper stirring and even mixing of the reaction is essential at high temperatures.

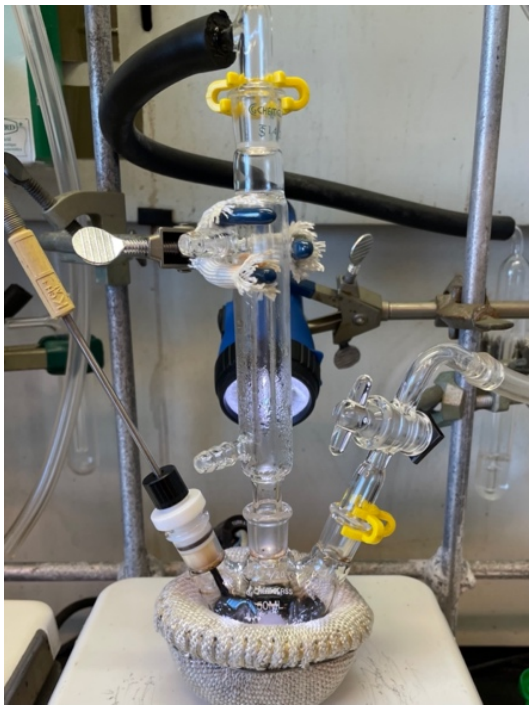

Figure 2.5. Experimental setup for the synthesis of magnetite nanoparticles.

Briefly, a stirred solution of FeOl-2 was heated under active evacuation of the headspace to 110 °C. After reaching 110 °C, the solution was evacuated for a further 30 min and then heated to reflux under N_2 flow (100 sccm). Upon achieving reflux, a stream of O_2 (5 sccm) in N_2 (100 sccm) was flowed through the reaction vessel to ensure magnetite phase purity and the reaction was allowed to continue for an

additional 30 min. Representative nanoparticle samples in the 5 – 16 nm range are shown in Figure 2.6 and Table 2.2, along with a full table of synthetic conditions (Table 2.4). Two tests of reproducibility are shown for 10.5 nm nanoparticles (Figure 2.16) and 12.5 nm nanoparticles (Figure 2.17).

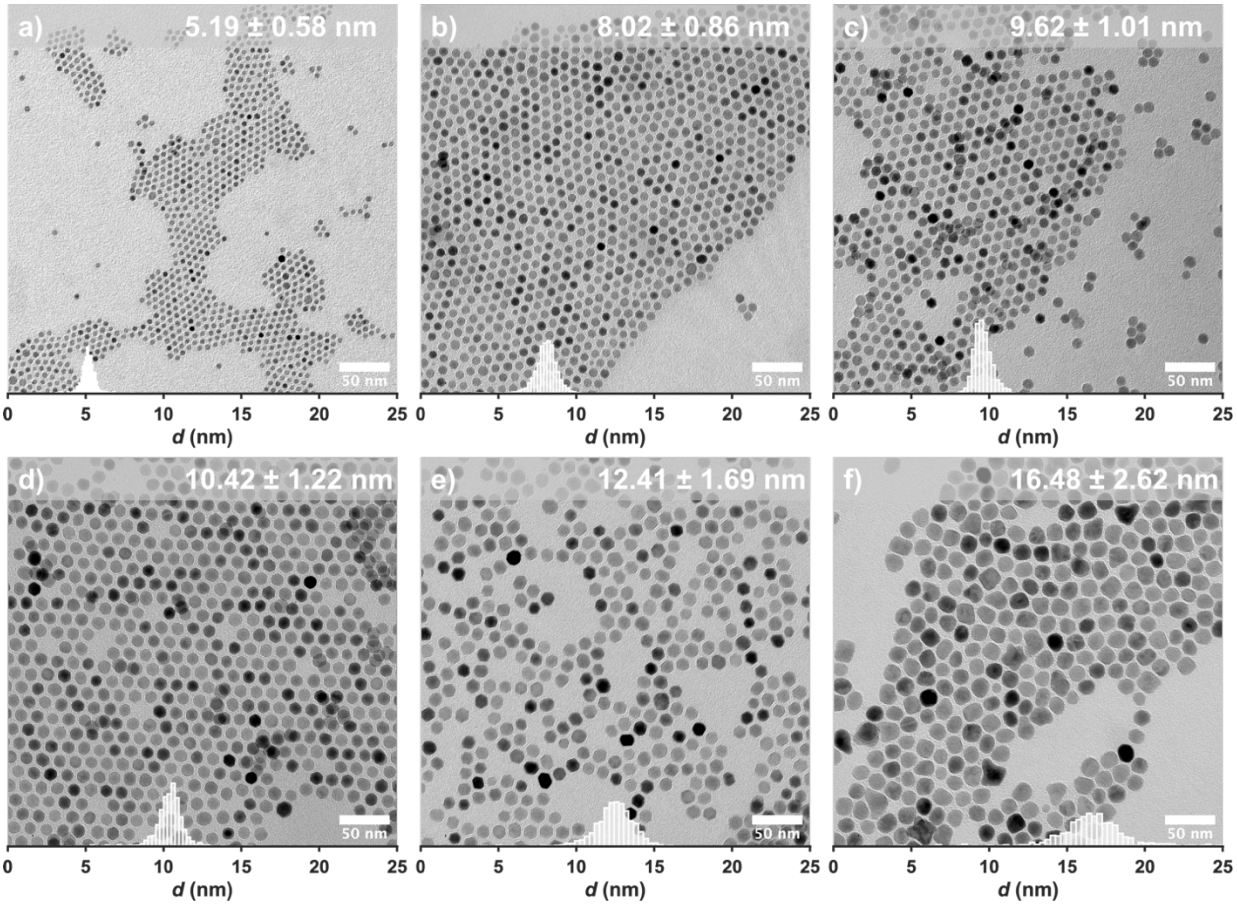

Figure 2.6. Representative TEM images of nanoparticles synthesized from FeOl-2 with overlaid size histograms.

Table 2.2. Nanoparticle size and size dispersity with varying synthetic conditions

Nanoparticles from FeOl-2			
Size (nm)	**RSD (%)**	**OA:Fe**	**Fe % (w/w)**
5.19	11.2	2.0	0.5
8.02	10.7	1.0	0.5
9.62	10.5	1.0	2.0
10.42	11.7	1.5	1.0
12.41	13.6	1.0	1.0
16.41	15.9	0.5	1.5
Nanoparticles from FeOl-3			
Size (nm)	**RSD (%)**	**OA:Fe**	**Fe % (w/w)**
4.24	10.8	1.5	0.9
4.99	12.2	0.7	1.3
5.19	12.9	1.5	1.4

As a result of the convenient ability to separately introduce iron and surfactant, the FeOl-2 precursor allows for a wider and more reliable investigation of the reaction parameter space than FeOl-1. Two variables are available for tuning nanoparticle size: the OA:Fe ratio and the overall Fe percentage (w/w) in the reaction. The OA in the OA:Fe ratio refers to the amount of OA added, as it assumes no residual/free OA present in FeOl-2 and FeOl-3. Figure 2.11 demonstrates a complete exploration of the parameter space with size distributions obtained from TEM images (Figure 2.18). Generally, we find that manipulation of these variables results in two different, yet rationalizable, trends. As the OA:Fe ratio increases, particle growth is inhibited by the additional surfactant, resulting in smaller particles. As the Fe percentage increases, more metal cluster i.e., $[Fe_3O(oleate)_6]^{n+}$ is available for nanoparticle growth, resulting in larger particles. Due to the complex nature and large parameter space of these reactions, these trends are not universal. For example, changes in OA concentration can influence the boiling point of the reaction mixture. The reaction boiling point has been shown to induce nucleation of particles, with higher boiling points resulting in larger nanoparticles.[49] Thus, as the two parameters (Fe % and OA:Fe) are adjusted, the boiling point is consequently altered, contributing to the size dependence in a way not fully captured by the OA:Fe ratio or the Fe percentage alone. A plot of particle size versus boiling point (Figure 2.19) exhibits a weak

trend, indicating that it is still a contributing factor for particle size control. Finally, magnetite phase purity was confirmed with powder X-ray diffraction (Figure 2.20).

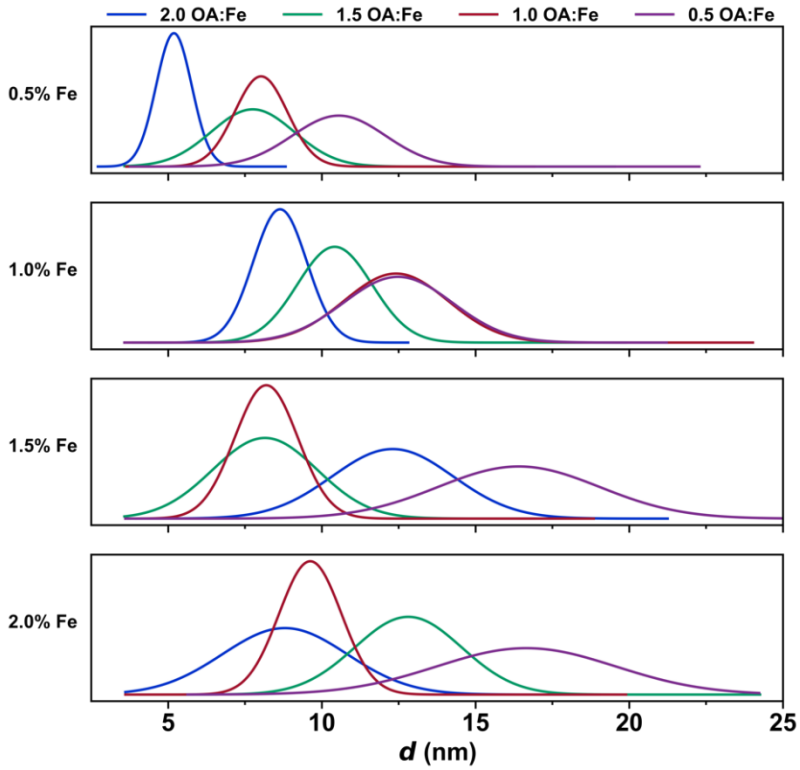

Figure 2.7. Nanoparticles synthesized from FeOl-2 were fit to normal distributions, demonstrating the effect of varying Fe % (w/w) and OA:Fe on nanoparticle size and size dispersity.

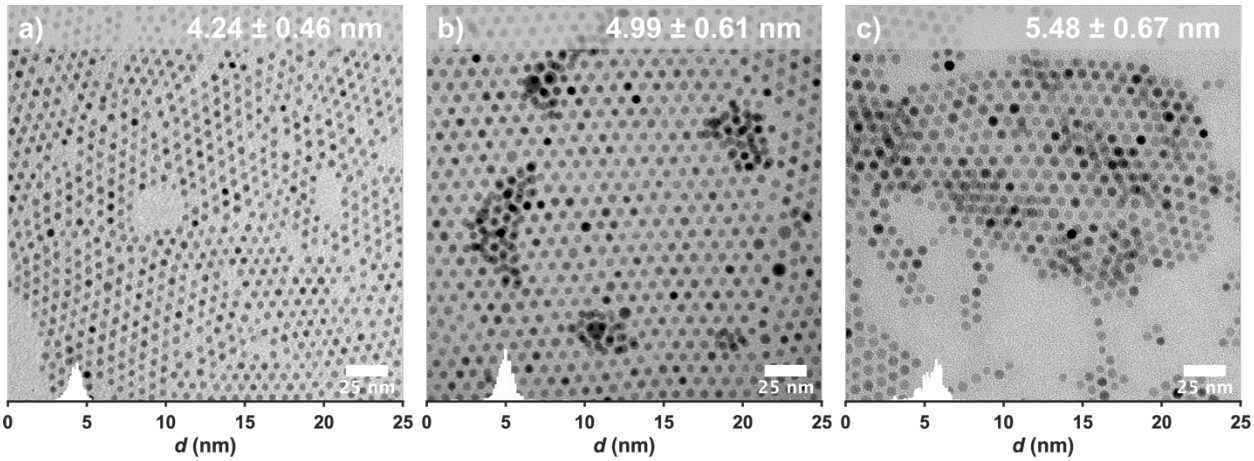

Figure 2.8. Representative TEM images of nanoparticles synthesized from FeOl-3 with overlaid size histograms.

The synthesis of iron oxide nanoparticles from FeOl-3 as a stock solution in octadecene was performed using a similar procedure to that of FeOl-2. In contrast to the wide size range accessible from FeOl-2, the size range of nanoparticles synthesized from FeOl-3 is limited to 4-5 nm (Figure 2.8). We attribute this to the structure and composition of FeOl-1. While FeOl-2 is an extended solid that is converted into reactive molecular cluster with heat and the addition of OA, FeOl-3 is likely far more reactive due to its discrete molecular cluster throughout its entire synthesis. Additionally, FeOl-3 is less sensitive to changes in OA:Fe and Fe %. Thus, the two materials complement each other; FeOl-2 allows for size control in the 5-16 nm range while FeOl-3 provides fine size control in the 4-5 nm range.

The two new starting materials, FeOl-2–3, are used in one-pot syntheses that selectively target a specific nanoparticle size without the use of an additional solvent,[18] seed-mediated growth,[50] or hot injection.[51] As the OA:Fe ratio decreases, less OA is available to control the nanoparticle shape resulting in larger, albeit non-spherical particles (Figure 2.6f). Within the scope of the reaction conditions used herein, specifically with ODE as solvent, particles reach a maximum size of 16.5 nm, with spherical shape control best achieved in the 4-12 nm range.

In several synthetic procedures, larger particle size has been achieved by adapting a synthesis to use with a higher boiling point solvent such as docosane.[42,44,52] As an initial test of the versatility of our precursors and methods, two reactions were performed with FeOl-2 in docosane, leading to low size dispersity 13 nm nanoparticles (Figure 2.21). Additionally, the role of flowing oxygen at reflux was simultaneously studied, with one reaction (Figure 2.21a) synthesized with 5% O_2 at reflux and the other (Figure 2.21b) synthesized with no O_2 at reflux, demonstrating the importance of O_2 for the synthesis of phase-pure magnetite.

2.4 Magnetic characterization of iron oxide nanoparticles

Iron oxide nanoparticles synthesized by thermal decomposition typically consist of magnetite (Fe_3O_4), a mixed valence material with a large saturation magnetization and a high magnetic

susceptibility.[53] However, the reducing environment generated by the iron oleate decomposition often leads to inadequate oxidation of Fe^{2+}, resulting in wüstite (FeO) core formation inside a magnetite (Fe_3O_4) shell. Nanoparticles of FeO@Fe_3O_4 exhibit a lower saturation magnetization and lower susceptibilities, limiting the sensitivity in magnetoresistance applications, for example.[54,55] As previously mentioned, we used a flow of oxygen (5%) during reflux to maintain an oxidizing environment without requiring a post-synthetic oxidation step involving ambient oxygen or a chemical oxidant.[42]

The room temperature magnetization vs. field curves of nanoparticles synthesized from FeOl-2 demonstrate superparamagnetic behavior consistent with magnetite (Figure 2.9a). As expected, the saturation magnetization generally increases with size. Additionally, a characteristic increase in blocking temperature with size is generally observed in the zero-field cooled (ZFC) curves (Figure 2.9b). This behavior is slightly more complex in the larger, faceted particles (10.4 nm and 12.4 nm), as well as in the largest, non-spherical particles (16.5 nm). Shape effects have been shown to strongly influence the ZFC curves and thus, the blocking temperature.[17] Of particular interest from this set of nanoparticle sizes is the emergence of the Verwey Transition at ~ 105 K for the 16.4 nm particles. The Verwey Transition is a metal-insulator transition observed in pure magnetite,[56–58] but is often suppressed due to the presence of defects or nanoscale size and shape effects. The nanoparticles synthesized from FeOl-3 exhibit a similar size dependence on the saturation magnetization (Figure 2.9c) and blocking temperature (Figure 2.9d).

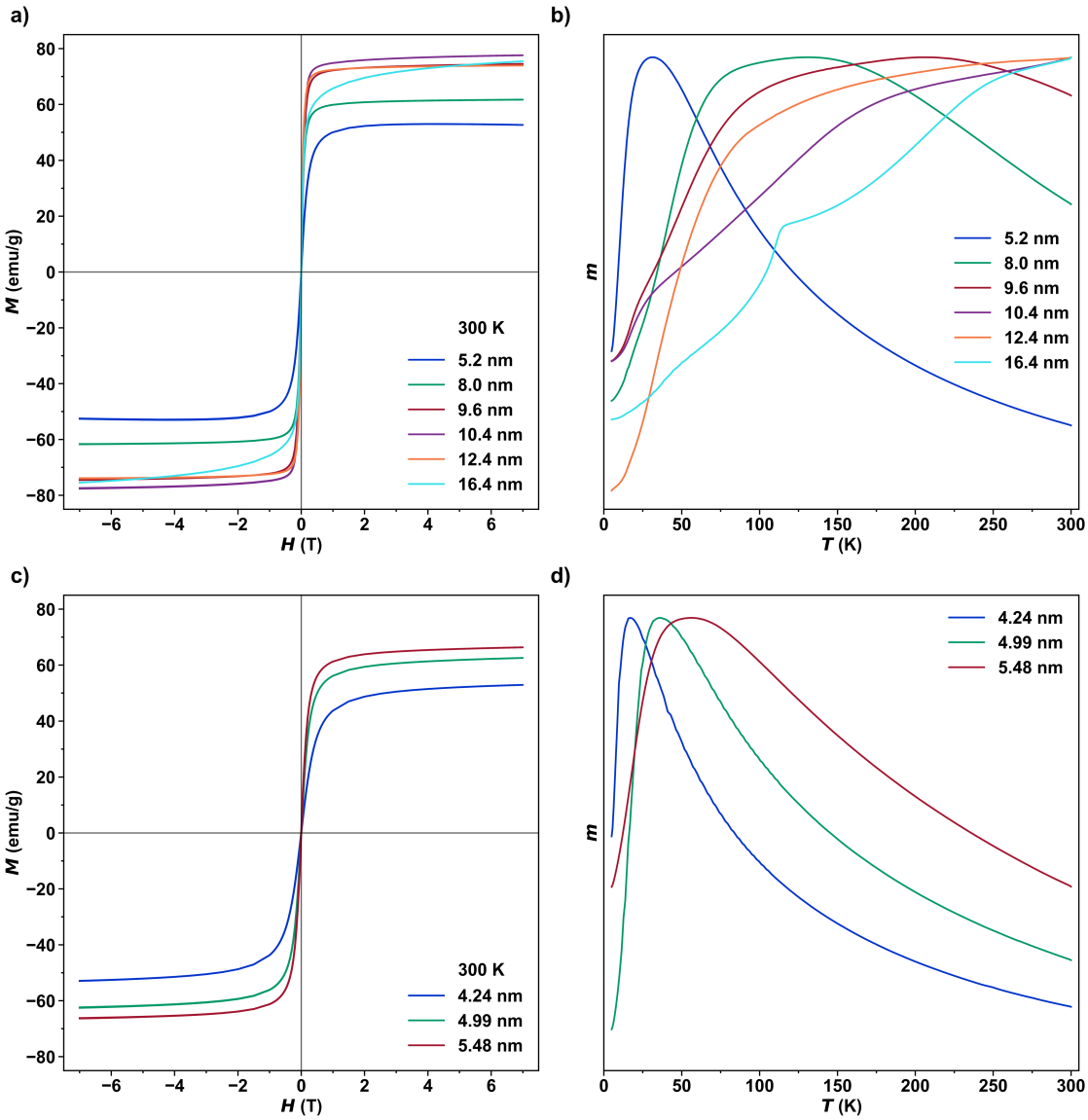

Figure 2.9. Static magnetic properties of nanoparticles synthesized from FeOl-2 and FeOl-3. Plots of isothermal magnetization vs. magnetic field for (a) FeOl-2 and (c) FeOl-3 at 300 K. Plots of normalized zero-field cooled magnetization vs. temperature from 5-300 K under an applied field of 0.01 T for (b) FeOl-2 and (d) FeOl-3.

2.5 Conclusions

Two new starting materials for the synthesis of high-quality magnetite have been synthesized, purified, and characterized. Namely, a free-flowing powder extended solid form (FeOl-2) and a soluble, waxy solid (FeOl-3). They display several desirable characteristics: a lack of free oleic acid, a consistent synthesis, and long-term stability. Thermal decomposition reactions of FeOl-2 and FeOl-3 yield nanoparticles in a tunable size range of 5-16 nm and 4-5 nm, respectively. A subsequent analysis of their static magnetic properties is presented, and trends are consistent with the expected dependencies of saturation magnetization and blocking temperature with size. Consistency of these materials, as well as the method of synthesis, will allow for a more reliable and quantitative mapping of magnetic properties on the nanoscale. Future work will extend the synthetic methods and precursor design ideas herein to enhance the reliability of magnetic properties in nanoparticle syntheses such as transition metal ferrites and antiferromagnetic oxides.

2.6 Experimental details

2.6.1 Safety considerations

The use of a pressure flask represents a convenient and green alternative to flowing water reflux condensers. Safety is paramount when heating closed vessels. The Ace pressure flasks are rated for 60 psig at 120 °C, which is well above the calculated pressure of this reaction performed at 70 °C.

2.6.2 Materials

The reagents used were iron (III) chloride hexahydrate (97% Alfa Aesar), iron (II) chloride tetrahydrate (97% Fisher), sodium oleate (97% TCI), oleic acid (90%, Alfa Aesar) and 1-octadecene (90% Sigma Aldrich). ACS grade hexane, ethanol, and methanol were purchased from Fisher. Oleic acid was

degassed and stored under vacuum in a Schlenk flask covered with aluminum foil. All other chemicals were used as received.

2.6.3 Synthesis of iron oleate: FeOl-1

In a 250 mL Ace round bottom pressure flask with a thermowell (rated for 60 psig at 120 °C), iron (III) chloride hexahydrate (4.05 g, 15 mmol) and sodium oleate (13.70 g, 45 mmol) were mixed with deionized (DI) water (30 mL), ethanol (23 mL), and hexanes (53 mL). The flask was sealed and heated to 70 °C for 4 h. After cooling to room temperature, the upper organic layer of the reaction was separated and washed with DI water (~ 50 mL) in a separatory funnel. The hexane was removed via vacuum, resulting in a viscous, dark red solid that was further dried in a vacuum oven (70 °C, house vacuum) for 24 h.

2.6.4 Synthesis of iron oleate: FeOl-2

In a 250 mL Ace round bottom pressure flask with a thermowell (rated for 60 psig at 120 °C), iron (III) chloride hexahydrate (4.05 g, 15 mmol) and sodium oleate (13.70 g, 45 mmol) were mixed with methanol (105 mL). The flask was sealed and heated to 70 °C for 4 h. After cooling to room temperature, a dark yellow clump was collected and washed with DI water (100 mL), forming a brown rubbery solid. The brown rubbery solid and 250 mL deionized water were added to a 250 mL Erlenmeyer flask. A tissue homogenizer (IKA Works T25 Basic S1) was used to simultaneously break up and wash the rubbery solid, converting it to a fine powder and removing residual sodium chloride and sodium oleate. The homogenization process was carried out for 0.5 h, followed by a vacuum filtration to recover the powder. An additional homogenization step was performed with 250 mL DI water for 0.5 h. The powder was collected again and dried in a vacuum oven (70 °C, house vacuum) for 24 h before being used in nanoparticle syntheses.

2.6.5 Synthesis of iron oleate: FeOl-3

In a 250 mL Ace round bottom pressure flask with a thermowell (rated for 60 psig at 120 °C), iron (III) chloride hexahydrate (2.70 g, 10 mmol), iron (II) chloride hexahydrate (1.00 g, 5 mmol), and sodium oleate (13.70 g, 45 mmol) were mixed with methanol (105 mL). The flask was sealed and heated in a mantle using a PID controller to 70 °C for 4 h. After cooling to room temperature, the viscous brown product was dissolved in 40 mL hexanes and washed with DI water (100 mL) in a separatory funnel. The iron oleate was left in hexanes. One mL of the hexane solution was dried out and weighed to determine the total amount of iron oleate. 1-octadecene was added to the iron oleate solution to make a 1:1 w/w stock solution. The hexane was removed via vacuum and the stock solution was dried in a vacuum oven (70 °C, house vacuum) for 24 h before being used in nanoparticle syntheses.

2.6.6 Synthesis of Fe_3O_4 nanoparticles from FeOl-2

Fe_3O_4 nanoparticles were synthesized according to modified literature procedures. In a typical synthesis, FeOl-2 was mixed with oleic acid (Table 2.4) in a 50 mL three-neck Morton flask and placed in a vacuum oven (70 °C, house vacuum) for 1 h. During this step, a stir bar was added and used to mix the FeOl-2 and OA, ensuring a homogenous product. This step helps to react the FeOl-2 and oleic acid, preventing FeOl-2 from depositing on the upper half of the flask during the degas and heat up. Without this step, it is difficult to avoid unreacted solid FeOl-2 accumulation on the sides of the flask during degas and heating, which can affect the reaction outcome. Afterwards, 1-octadecene was added according to Table 2.4. The flask was equipped with a temperature probe (left neck), condenser (middle neck), and flow adapter (right neck), then placed in a heating mantle. The reaction was degassed and backfilled with dinitrogen three times at room temperature. The reaction mixture was heated to 110 °C and degassed under vacuum for 0.5 h, after which the atmosphere was backfilled with dinitrogen. Throughout the reaction, dinitrogen (100 sccm) was flowed through a side neck of the Morton flask and out the top of the condenser, attached to an oil bubbler. The reaction mixture was heated to reflux at 3.3 °C/min using a PID controller and

refluxed for 0.5 h. When the temperature reached reflux, dioxygen (5 sccm) was added to the dinitrogen stream and flowed until the end of the reaction. The reflux temperature was recorded, and the timer was started when vigorous bubbling began. The stir rate of the reaction was kept to a minimum (500 rpm) during heat-up and increased (1100 rpm) at 300 °C. This is necessary to keep material within the reaction mixture during heat up.

2.6.7 Synthesis of Fe3O4 nanoparticles from FeOl-3

Fe_3O_4 nanoparticles were synthesized according to modified literature procedures. In a typical synthesis from the iron oleate stock solution, 2.00 g of the stock solution (1.00 g FeOl-3 in 1.00 g 1-octadecene) was mixed with oleic acid (0.20 g) and additional 1-octadecene (6.00 g) in a 50 mL three-neck Morton flask. The flask was equipped with a temperature probe (left neck), condenser (middle neck), and flow adapter (right neck), then placed in a heating mantle. The reaction was degassed and backfilled with dinitrogen three times at room temperature. The reaction mixture was heated to 110 °C and degassed under vacuum for 0.5 h, after which the atmosphere was backfilled with dinitrogen. Throughout the reaction, dinitrogen (100 sccm) was flowed through a side neck of the Morton flask and out the top of the condenser, attached to an oil bubbler. The reaction mixture was heated to reflux at 3.3 °C/min using a PID controller and refluxed for 0.5 h. When the temperature reached reflux, dioxygen (5 sccm) was added to the dinitrogen stream and flowed until the end of the reaction.

2.6.8 Fe_3O_4 nanoparticle purification

Nanoparticles were isolated and purified by the addition of hexanes and ethanol in a 1:1 ratio, followed by centrifugation (7 minutes at 8500 rpm). The nanoparticles were redispersed in hexanes. Two more cycles of purification by precipitation with ethanol and centrifugation were carried out before storing the nanoparticles in hexanes.

2.6.9 Characterization

Transmission electron microscopy was carried out using a FEI Spirit TEM operating at 120 kV, with images collected by a 2k x 2k Gatan CCD camera. TEM samples were prepared by drop-casting and air drying a dilute solution of nanoparticles in hexanes onto a carbon-coated copper TEM grid. Particles were analyzed in ImageJ using the default thresholding algorithm of sample sizes exceeding 500 particles for all syntheses.

IR measurements were carried out using a Bruker Alpha FT-IR spectrometer.

MALDI-MS was carried out on a Bruker Autoflex Max. Bruker peptide calibration standard II (Bradykinin Fragment 1-7, Angiotensin II, Angiotensin I, Substance P, Bombesin, Renin Substrate, ACTH clip 1-17, ACTH clip 18-39, Somatostatin 28) in a HCCA matrix was used as a calibrant. Samples were mixed with 9-nitroanthracene matrix in chloroform. A pulsed nitrogen laser (337 nm) with a power setting of 55% was used with a 21 kV potential operating in positive ion mode.

Magnetic measurements were carried out using a Quantum Design MPMS3 SQUID magnetometer. Nanoparticle samples were dried to a fine powder (1-2 mg), loaded into a VSM sample holder, and secured in a plastic straw.

The iron concentration was determined by ICP-MS. Samples were digested in 70% HNO_3 (TraceMetal^{TM} grade), diluted to 3% HNO_3 with milli-q water and analyzed by a Thermo iCAP RQ ICP−MS. Elemental analysis was performed on a Perkin Elmer PE2400-Series II, CHNS/O analyzer. Powder x-ray diffraction was performed with a Bruker D8 Advance diffractometer using Cu Kα (1.5418 Å) radiation (40 kV, 40 mA) or a Bruker Apex II Ultra CCD using Mo Kα (λ = 0.71073 Å) radiation.

2.7 Additional information

Table 2.3. Batch to batch comparison of FeOl-2 from EA and ICP-MS

FeOl-2	C	H	Fe
Batch A	60.32	8.28	15.45
Batch B	60.18	8.74	14.97
Batch C	60.76	8.56	15.39
Average	60.42 ± 0.30	8.50 ± 0.14	15.29 ± 0.26

Table 2.4. Summary of nanoparticle synthesis parameters

Nanoparticles synthesized from FeOl-2						
FeOl-2 (g)	**OA (g)**	**ODE (g)**	**OA:Fe (mol)**	**Fe % (w/w)**	**Size (nm)**	**Stdev**
0.25	0.10	7.30	0.5	0.5	10.55	1.52
0.25	0.19	7.20	1.0	0.5	8.02	0.86
0.25	0.29	7.13	1.5	0.5	7.75	1.35
0.25	0.38	7.00	2.0	0.5	5.19	0.58
0.50	0.20	6.95	0.5	1.0	12.48	1.77
0.50	0.39	6.80	1.0	1.0	12.41	1.69
0.50	0.59	6.59	1.5	1.0	10.42	1.22
0.50	0.78	6.40	2.0	1.0	8.64	0.87
0.75	0.29	6.61	0.5	1.5	16.41	2.63
0.75	0.57	6.30	1.0	1.5	8.19	1.03
0.75	0.87	6.02	1.5	1.5	8.15	1.70
0.75	1.16	5.74	2.0	1.5	12.30	1.97
1.00	0.46	6.27	0.6	2.0	16.65	2.91
1.00	0.77	5.87	1.0	2.0	9.62	1.01
1.00	1.17	5.48	1.5	2.0	12.81	1.74
1.00	1.55	5.09	2.0	2.0	8.80	2.03

Nanoparticles synthesized from FeOl-3						
FeOl-3 (g)	**OA (g)**	**ODE (g)**	**OA:Fe (mol)**	**% Fe (w/w)**	**Size (nm)**	**Stdev**
0.87	0.59	7.00	1.5	0.9	4.24	0.46
1.26	0.40	7.00	0.7	1.3	4.99	0.61
1.50	1.01	7.00	1.5	1.4	5.48	0.67

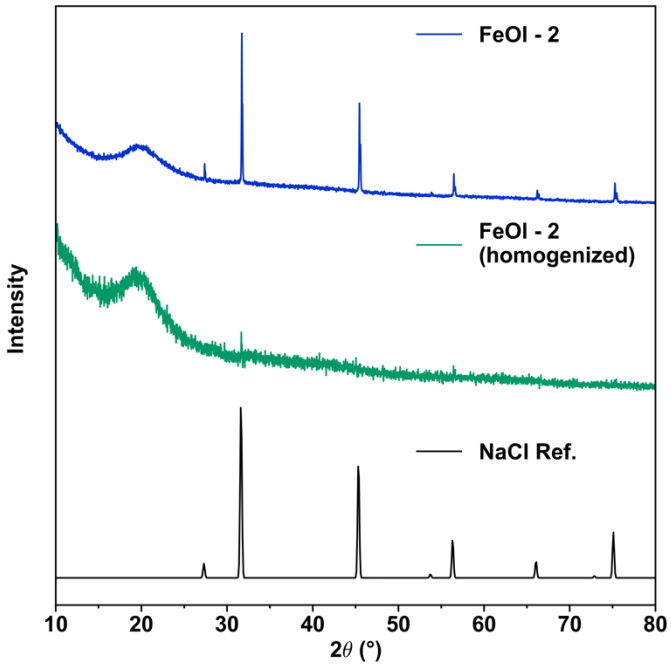

Figure 2.10. Powder x-ray diffraction patterns of non-homogenized and homogenized FeOl-2 with NaCl reference pattern, demonstrating the utility of a tissue homogenizer in removing NaCl.

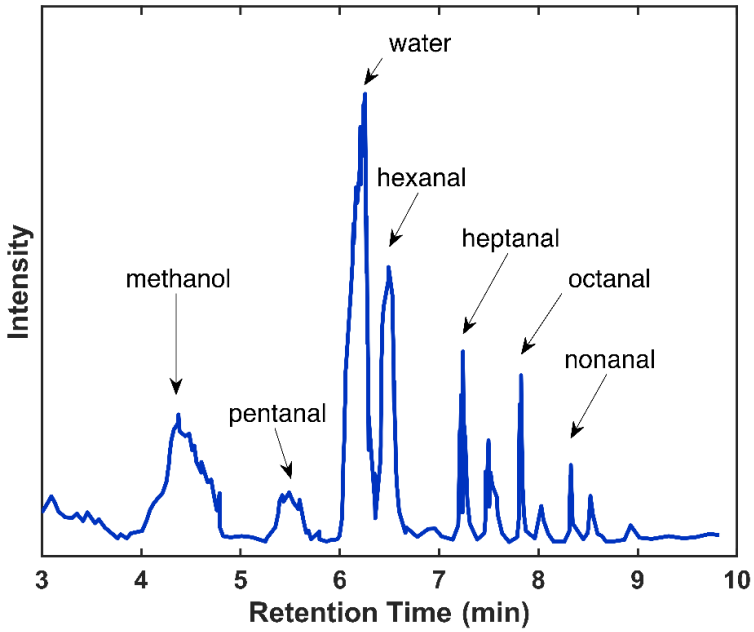

Figure 2.11. GCMS chromatograph of the headspace during the reaction of FeOl-2 and oleic acid at 70 °C. Peaks without corresponding labels were unable to be identified by the MS software.

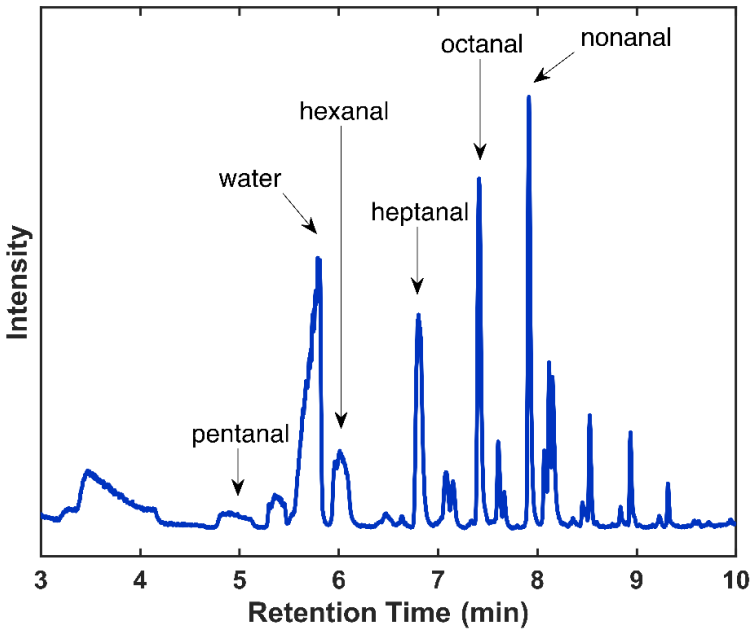

Figure 2.12. GCMS chromatograph of the headspace during the reaction of FeOl-1 and oleic acid at 70 °C. Peaks without corresponding labels were unable to be identified by the MS software.

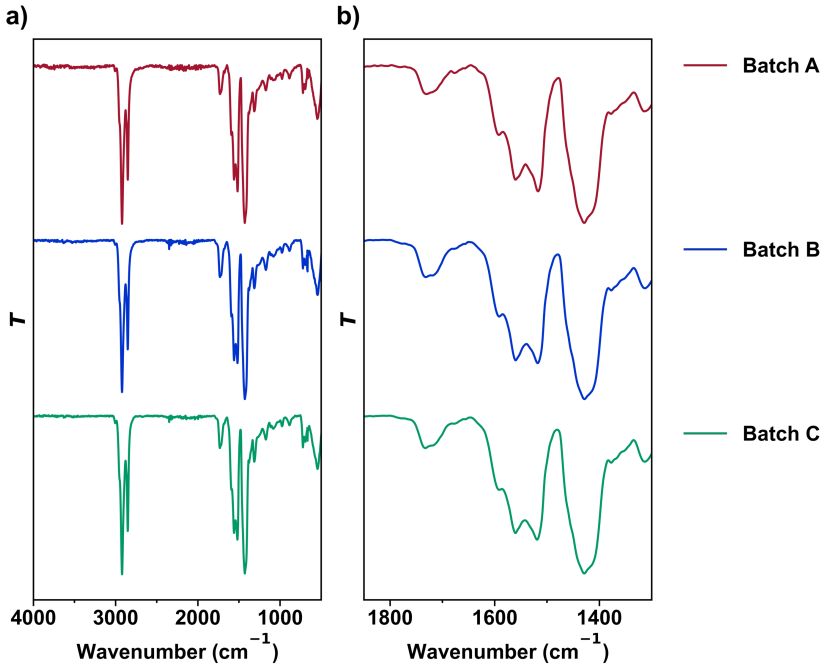

Figure 2.13. Full IR spectra for three batches of FeOl-2 prepared in identical fashion. (a) Full spectrum and (b) metal carboxylate region.

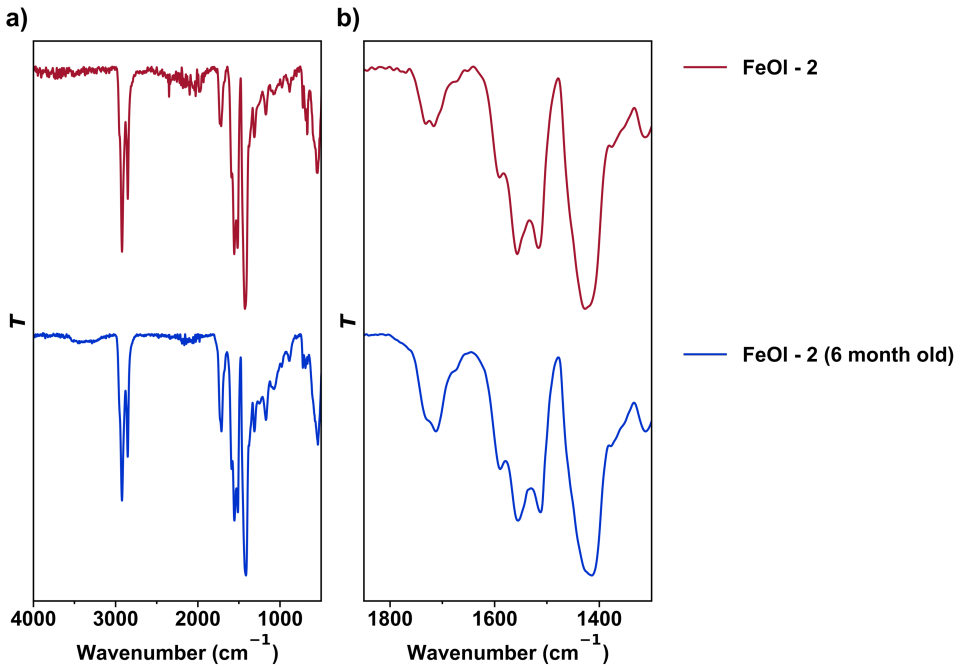

Figure 2.14. Full IR spectra (a) and metal carboxylate region (b) of freshly synthesized FeOl-2 vs. six-month-old FeOl-2 stored under ambient conditions.

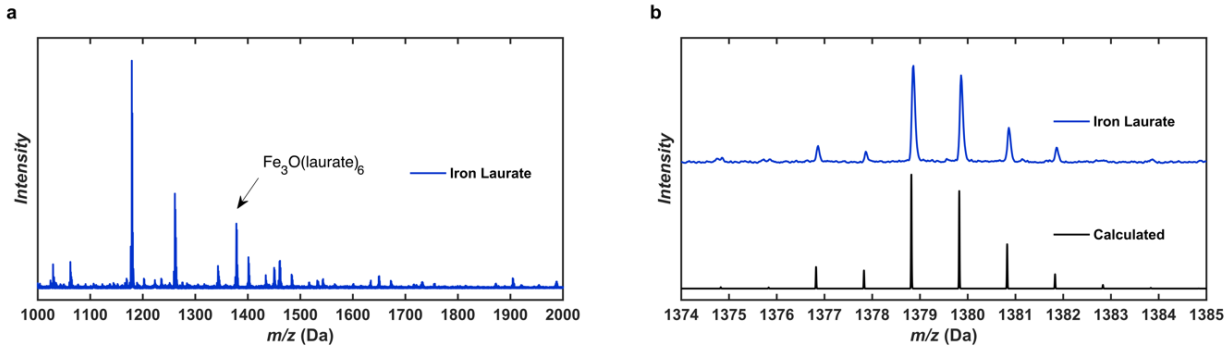

Figure 2.15. MALDI-MS data demonstrating ligand replacement on the central metal-oxo cluster. (a) Full MALDI-MS spectra of $Fe_3O(laurate)_6$, (b) and molecular ion with calculated isotope pattern.

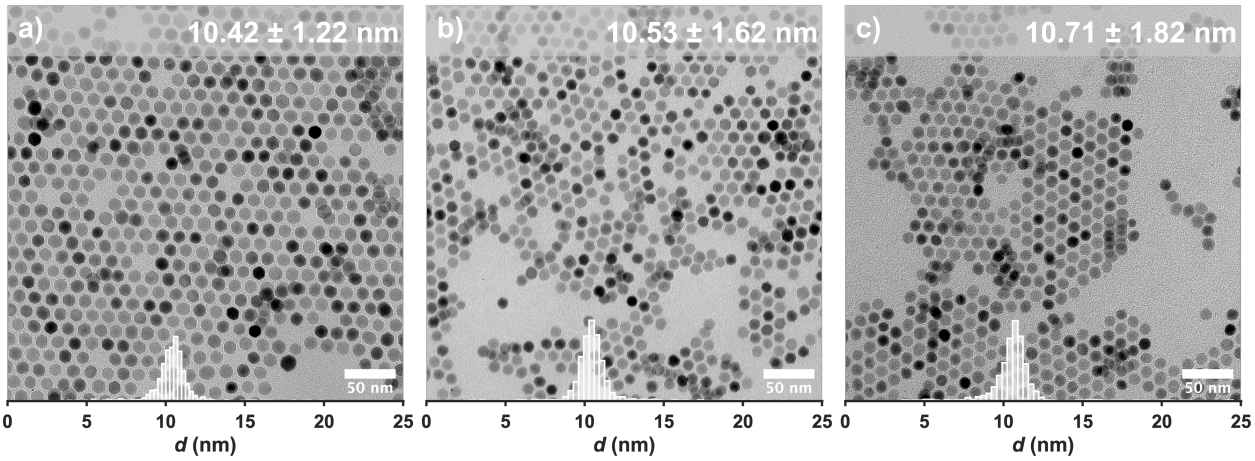

Figure 2.16. TEM images of repeated reactions for the synthesis of 10.5 nm nanoparticles from FeOl-2.

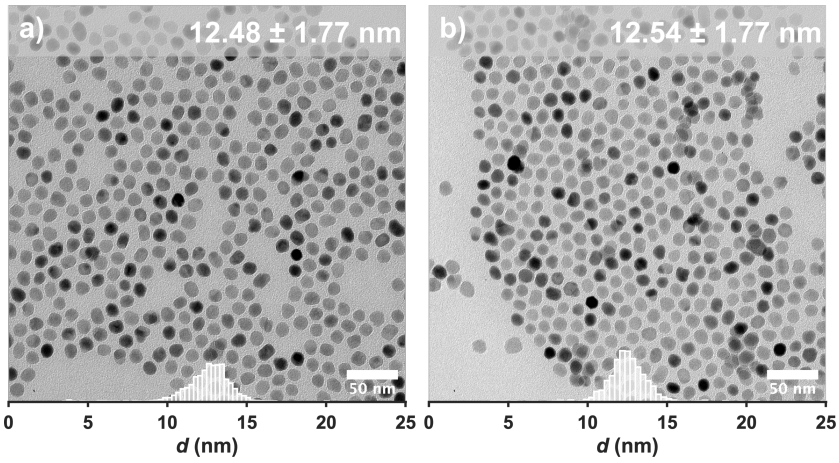

Figure 2.17. TEM images of repeated reactions for the synthesis of 12.5 nm nanoparticles from FeOl-2.

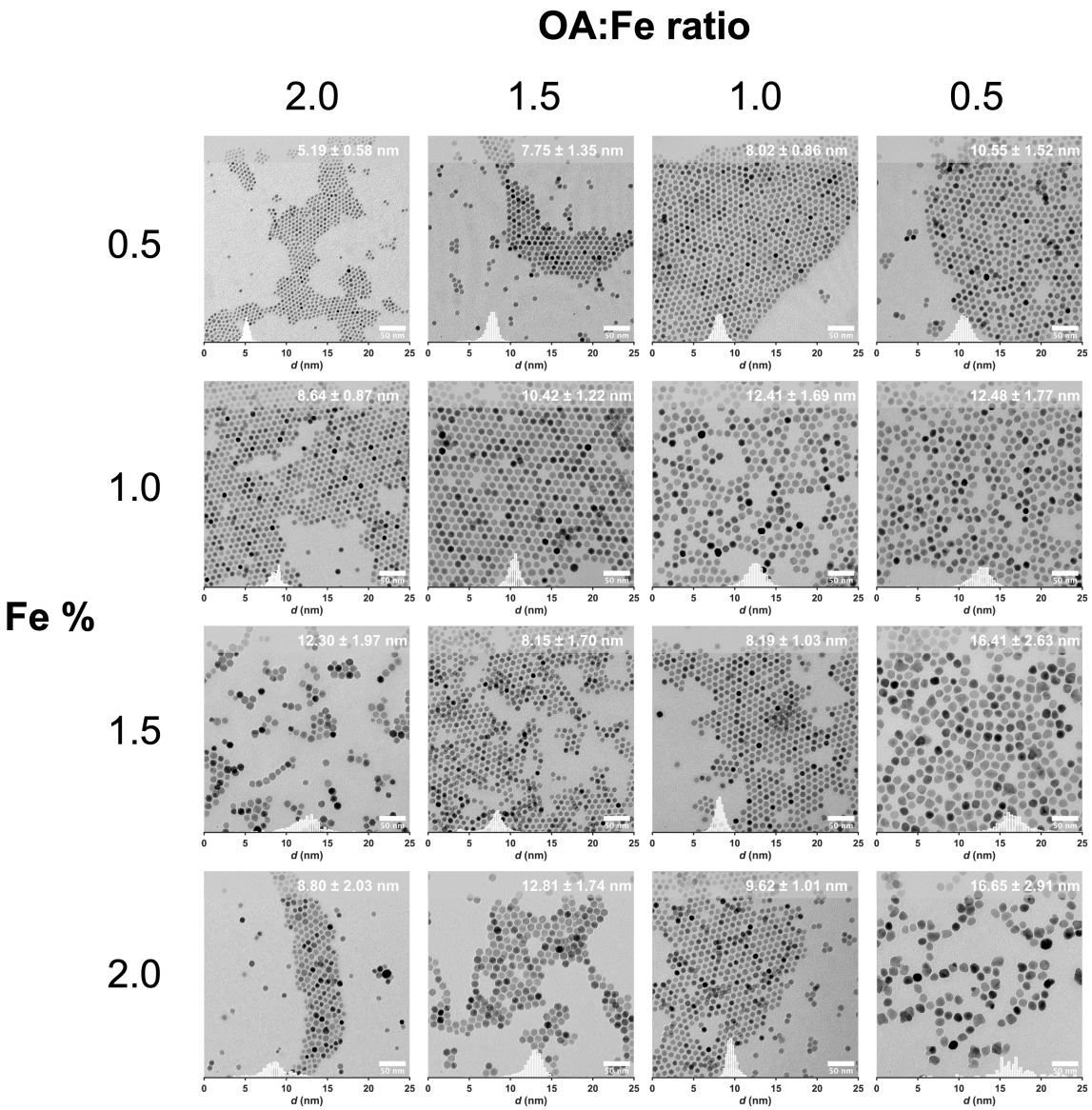

Figure 2.18. TEM images from full exploration of the parameter space, varying the OA:Fe molar ratio (top) and Fe % (bottom). Synthetic parameters for each synthesis are in Table 2.4.

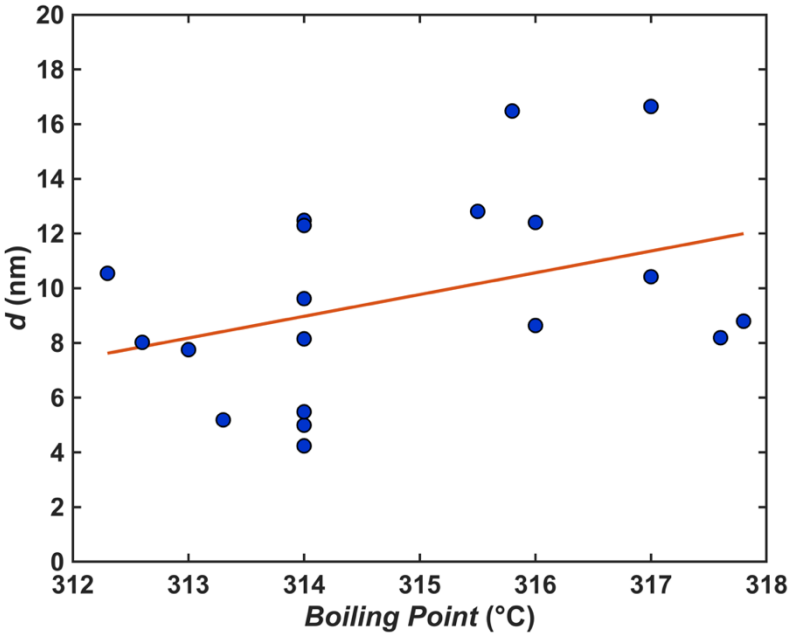

Figure 2.19. Plot of particle diameter (nm) vs. boiling point (°C) of the nanoparticle reaction showing weak correlation ($y = 0.7951x - 240.67$ $R^2 = 0.1425$).

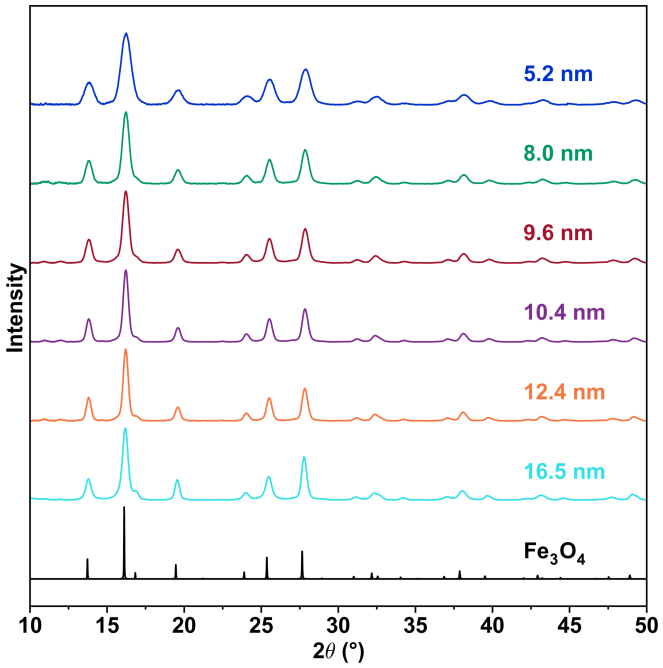

Figure 2.20. Powder X-ray diffraction (PXRD) patterns for the six representative magnetite nanoparticle sizes shown in Figure 2.3, collected using a Mo Kα (λ = 0.71073 Å) source.

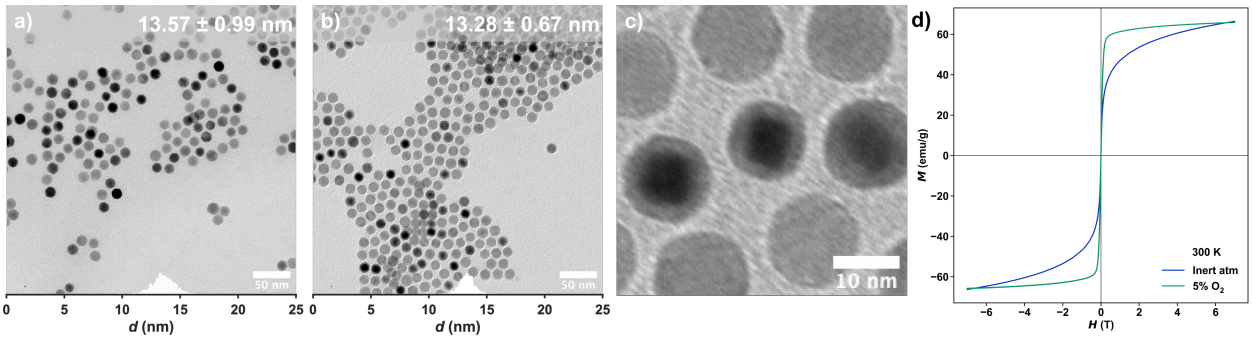

Figure 2.21. TEM images of nanoparticles synthesized from FeOl-2 in docosane. (a) Phase-pure nanoparticles from 5% O_2 flow at reflux. (b) Core-shelled nanoparticles from no O_2 flow at reflux. (c) Observed core-shelling. (d) Plot of isothermal magnetization vs. magnetic field for phase-pure and core-shelled nanoparticles at 300 K.

2.8 Acknowledgements

Chapter 2, in full, is a reformatted reprint from the manuscript entitled "Size-Tunable Magnetite Nanoparticles from Well-Defined Iron Oleate Precursors" by Kirkpatrick, K. M.; Zhou, B. H.; Bunting, P. C.; Rinehart, J. D. The dissertation author was a primary researcher and author of this paper. Reprinted with permission from *Chem. Mater.* **2022**, *34* (17), 8043–8053. Copyright 2022 American Chemical Society.

2.9 References

(1) Sun, S.; Zeng, H. Size-Controlled Synthesis of Magnetite Nanoparticles. *J. Am. Chem. Soc.* **2002**, *124* (28), 8204–8205. https://doi.org/10.1021/ja026501x.

(2) Park, J.; An, K.; Hwang, Y.; Park, J.-G.; Noh, H.-J.; Kim, J.-Y.; Park, J.-H.; Hwang, N.-M.; Hyeon, T. Ultra-Large-Scale Syntheses of Monodisperse Nanocrystals. *Nature Mater* **2004**, *3* (12), 891–895. https://doi.org/10.1038/nmat1251.

(3) Talapin, D. V.; Lee, J.-S.; Kovalenko, M. V.; Shevchenko, E. V. Prospects of Colloidal Nanocrystals for Electronic and Optoelectronic Applications. *Chem. Rev.* **2010**, *110* (1), 389–458. https://doi.org/10.1021/cr900137k.

(4) van Embden, J.; Chesman, A. S. R.; Jasieniak, J. J. The Heat-Up Synthesis of Colloidal Nanocrystals. *Chem. Mater.* **2015**, *27* (7), 2246–2285. https://doi.org/10.1021/cm5028964.

(5) An, K.; Lee, N.; Park, J.; Kim, S. C.; Hwang, Y.; Park, J.-G.; Kim, J.-Y.; Park, J.-H.; Han, M. J.; Yu, J.; Hyeon, T. Synthesis, Characterization, and Self-Assembly of Pencil-Shaped CoO Nanorods. *J. Am. Chem. Soc.* **2006**, *128* (30), 9753–9760. https://doi.org/10.1021/ja0608702.

(6) Buck, M. R.; Biacchi, A. J.; Schaak, R. E. Insights into the Thermal Decomposition of Co(II) Oleate for the Shape-Controlled Synthesis of Wurtzite-Type CoO Nanocrystals. *Chem. Mater.* **2014**, *26* (3), 1492–1499. https://doi.org/10.1021/cm4041055.

(7) Jana, N. R.; Chen, Y.; Peng, X. Size- and Shape-Controlled Magnetic (Cr, Mn, Fe, Co, Ni) Oxide Nanocrystals via a Simple and General Approach. *Chem. Mater.* **2004**, *16* (20), 3931–3935. https://doi.org/10.1021/cm049221k.
(8) Choi, S.-H.; Kim, E.-G.; Park, J.; An, K.; Lee, N.; Kim, S. C.; Hyeon, T. Large-Scale Synthesis of Hexagonal Pyramid-Shaped ZnO Nanocrystals from Thermolysis of Zn−Oleate Complex. *J. Phys. Chem. B* **2005**, *109* (31), 14792–14794. https://doi.org/10.1021/jp052934l.
(9) Bao, N.; Shen, L.; Wang, Y.; Padhan, P.; Gupta, A. A Facile Thermolysis Route to Monodisperse Ferrite Nanocrystals. *J. Am. Chem. Soc.* **2007**, *129* (41), 12374–12375. https://doi.org/10.1021/ja074458d.
(10) Chang, H.; Kim, B. H.; Lim, S. G.; Baek, H.; Park, J.; Hyeon, T. Role of the Precursor Composition in the Synthesis of Metal Ferrite Nanoparticles. *Inorg. Chem.* **2021**, *60* (7), 4261–4268. https://doi.org/10.1021/acs.inorgchem.0c03567.
(11) Castellanos-Rubio, I.; Arriortua, O.; Marcano, L.; Rodrigo, I.; Iglesias-Rojas, D.; Barón, A.; Olazagoitia-Garmendia, A.; Olivi, L.; Plazaola, F.; Fdez-Gubieda, M. L.; Castellanos-Rubio, A.; Garitaonandia, J. S.; Orue, I.; Insausti, M. Shaping Up Zn-Doped Magnetite Nanoparticles from Mono- and Bimetallic Oleates: The Impact of Zn Content, Fe Vacancies, and Morphology on Magnetic Hyperthermia Performance. *Chem. Mater.* **2021**, *33* (9), 3139–3154. https://doi.org/10.1021/acs.chemmater.0c04794.
(12) Bronstein, L. M.; Huang, X.; Retrum, J.; Schmucker, A.; Pink, M.; Stein, B. D.; Dragnea, B. Influence of Iron Oleate Complex Structure on Iron Oxide Nanoparticle Formation. *Chem. Mater.* **2007**, *19* (15), 3624–3632. https://doi.org/10.1021/cm062948j.
(13) Kim, B. H.; Shin, K.; Kwon, S. G.; Jang, Y.; Lee, H.-S.; Lee, H.; Jun, S. W.; Lee, J.; Han, S. Y.; Yim, Y.-H.; Kim, D.-H.; Hyeon, T. Sizing by Weighing: Characterizing Sizes of Ultrasmall-Sized Iron Oxide Nanocrystals Using MALDI-TOF Mass Spectrometry. *J. Am. Chem. Soc.* **2013**, *135* (7), 2407–2410. https://doi.org/10.1021/ja310030c.
(14) Kemp, S. J.; Ferguson, R. M.; Khandhar, A. P.; Krishnan, K. M. Monodisperse Magnetite Nanoparticles with Nearly Ideal Saturation Magnetization. *RSC Adv.* **2016**, *6* (81), 77452–77464. https://doi.org/10.1039/C6RA12072E.
(15) Kovalenko, M. V.; Bodnarchuk, M. I.; Lechner, R. T.; Hesser, G.; Schäffler, F.; Heiss, W. Fatty Acid Salts as Stabilizers in Size- and Shape-Controlled Nanocrystal Synthesis: The Case of Inverse Spinel Iron Oxide. *J. Am. Chem. Soc.* **2007**, *129* (20), 6352–6353. https://doi.org/10.1021/ja0692478.
(16) Bronstein, L. M.; Atkinson, J. E.; Malyutin, A. G.; Kidwai, F.; Stein, B. D.; Morgan, D. G.; Perry, J. M.; Karty, J. A. Nanoparticles by Decomposition of Long Chain Iron Carboxylates: From Spheres to Stars and Cubes. *Langmuir* **2011**, *27* (6), 3044–3050. https://doi.org/10.1021/la104686d.
(17) Ma, Z.; Mohapatra, J.; Wei, K.; Liu, J. P.; Sun, S. Magnetic Nanoparticles: Synthesis, Anisotropy, and Applications. *Chem. Rev.* **2021**, acs.chemrev.1c00860. https://doi.org/10.1021/acs.chemrev.1c00860.
(18) Castellanos-Rubio, I.; Arriortua, O.; Iglesias-Rojas, D.; Barón, A.; Rodrigo, I.; Marcano, L.; Garitaonandia, J. S.; Orue, I.; Fdez-Gubieda, M. L.; Insausti, M. A Milestone in the Chemical Synthesis of Fe_3O_4 Nanoparticles: Unreported Bulklike Properties Lead to a Remarkable Magnetic Hyperthermia. *Chem. Mater.* **2021**, acs.chemmater.1c02654. https://doi.org/10.1021/acs.chemmater.1c02654.
(19) Lekshmi, I. C.; Buonsanti, R.; Nobile, C.; Rinaldi, R.; Cozzoli, P. D.; Maruccio, G. Tunneling Magnetoresistance with Sign Inversion in Junctions Based on Iron Oxide Nanocrystal Superlattices. *ACS Nano* **2011**, *5* (3), 1731–1738. https://doi.org/10.1021/nn102301y.
(20) Chen, J.; Ye, X.; Oh, S. J.; Kikkawa, J. M.; Kagan, C. R.; Murray, C. B. Bistable Magnetoresistance Switching in Exchange-Coupled $CoFe_2O_4$–Fe_3O_4 Binary Nanocrystal Superlattices by Self-Assembly and Thermal Annealing. *ACS Nano* **2013**, *7* (2), 1478–1486. https://doi.org/10.1021/nn3052617.
(21) Lv, Z.-P.; Luan, Z.-Z.; Cai, P.-Y.; Wang, T.; Li, C.-H.; Wu, D.; Zuo, J.-L.; Sun, S. Enhancing Magnetoresistance in Tetrathiafulvalene Carboxylate Modified Iron Oxide Nanoparticle Assemblies. *Nanoscale* **2016**, *8* (24), 12128–12133. https://doi.org/10.1039/C6NR03311C.

(22) Zhou, B. H.; Rinehart, J. D. A Size Threshold for Enhanced Magnetoresistance in Colloidally Prepared $CoFe_2O_4$ Nanoparticle Solids. *ACS Cent. Sci.* **2018**, *4* (9), 1222–1227. https://doi.org/10.1021/acscentsci.8b00399.
(23) Zhou, B. H.; Rinehart, J. D. Pseudo Spin Valve Behavior in Colloidally Prepared Nanoparticle Films. *ACS Appl. Electron. Mater.* **2019**, *1* (7), 1065–1069. https://doi.org/10.1021/acsaelm.9b00196.
(24) Kole, M.; Khandekar, S. Engineering Applications of Ferrofluids: A Review. *Journal of Magnetism and Magnetic Materials* **2021**, *537*, 168222. https://doi.org/10.1016/j.jmmm.2021.168222.
(25) Panagiotopoulos, N.; Vogt, F.; Barkhausen, J.; Buzug, T. M.; Duschka, R. L.; Lüdtke-Buzug, K.; Ahlborg, M.; Bringout, G.; Debbeler, C.; Gräser, M.; Kaethner, C.; Stelzner, J.; Medimagh, H.; Haegele, J. Magnetic Particle Imaging: Current Developments and Future Directions. *IJN* **2015**, 3097. https://doi.org/10.2147/IJN.S70488.
(26) Yu, E. Y.; Bishop, M.; Zheng, B.; Ferguson, R. M.; Khandhar, A. P.; Kemp, S. J.; Krishnan, K. M.; Goodwill, P. W.; Conolly, S. M. Magnetic Particle Imaging: A Novel in Vivo Imaging Platform for Cancer Detection. *Nano Lett.* **2017**, *17* (3), 1648–1654. https://doi.org/10.1021/acs.nanolett.6b04865.
(27) Tay, Z. W.; Hensley, D. W.; Vreeland, E. C.; Zheng, B.; Conolly, S. M. The Relaxation Wall: Experimental Limits to Improving MPI Spatial Resolution by Increasing Nanoparticle Core Size. *Biomed. Phys. Eng. Express* **2017**, *3* (3), 035003. https://doi.org/10.1088/2057-1976/aa6ab6.
(28) Wu, K.; Su, D.; Saha, R.; Wong, D.; Wang, J.-P. Magnetic Particle Spectroscopy-Based Bioassays: Methods, Applications, Advances, and Future Opportunities. *J. Phys. D: Appl. Phys.* **2019**, *52* (17), 173001. https://doi.org/10.1088/1361-6463/ab03c0.
(29) Wu, K.; Su, D.; Saha, R.; Liu, J.; Chugh, V. K.; Wang, J.-P. Magnetic Particle Spectroscopy: A Short Review of Applications Using Magnetic Nanoparticles. *ACS Appl. Nano Mater.* **2020**, *3* (6), 4972–4989. https://doi.org/10.1021/acsanm.0c00890.
(30) Biacchi, A.; Bui, T.; Dennis, C.; Woods, S.; Hight Walker, A. Design and Engineering Colloidal Magnetic Particles for Nanoscale Thermometry. *International Journal on Magnetic Particle Imaging* **2020**, Vol 6 No 2 Suppl. 1 (2020). https://doi.org/10.18416/IJMPI.2020.2009068.
(31) Bui, T.; Biacchi, A.; Woods, S. Towards Bimagnetic Nanoparticle Thermometry. *International Journal on Magnetic Particle Imaging* **2020**, Vol 6 No 2 Suppl. 1 (2020). https://doi.org/10.18416/IJMPI.2020.2009010.
(32) Cotin, G.; Kiefer, C.; Perton, F.; Ihiawakrim, D.; Blanco-Andujar, C.; Moldovan, S.; Lefevre, C.; Ersen, O.; Pichon, B.; Mertz, D.; Bégin-Colin, S. Unravelling the Thermal Decomposition Parameters for The Synthesis of Anisotropic Iron Oxide Nanoparticles. *Nanomaterials* **2018**, *8* (11), 881. https://doi.org/10.3390/nano8110881.
(33) Cotin, G.; Perton, F.; Petit, C.; Sall, S.; Kiefer, C.; Begin, V.; Pichon, B.; Lefevre, C.; Mertz, D.; Greneche, J.-M.; Begin-Colin, S. Harnessing Composition of Iron Oxide Nanoparticle: Impact of Solvent-Mediated Ligand–Ligand Interaction and Competition between Oxidation and Growth Kinetics. *Chem. Mater.* **2020**, *32* (21), 9245–9259. https://doi.org/10.1021/acs.chemmater.0c03041.
(34) Perton, F.; Cotin, G.; Kiefer, C.; Strub, J.-M.; Cianferani, S.; Greneche, J.-M.; Parizel, N.; Heinrich, B.; Pichon, B.; Mertz, D.; Begin-Colin, S. Iron Stearate Structures: An Original Tool for Nanoparticles Design. *Inorg. Chem.* **2021**, acs.inorgchem.1c01689. https://doi.org/10.1021/acs.inorgchem.1c01689.
(35) Redl, F. X.; Black, C. T.; Papaefthymiou, G. C.; Sandstrom, R. L.; Yin, M.; Zeng, H.; Murray, C. B.; O'Brien, S. P. Magnetic, Electronic, and Structural Characterization of Nonstoichiometric Iron Oxides at the Nanoscale. *J. Am. Chem. Soc.* **2004**, *126* (44), 14583–14599. https://doi.org/10.1021/ja046808r.
(36) Sanchez-Lievanos, K. R.; Tariq, M.; Brennessel, W. W.; Knowles, K. E. Heterometallic Trinuclear Oxo-Centered Clusters as Single-Source Precursors for Synthesis of Stoichiometric Monodisperse Transition Metal Ferrite Nanocrystals. *Dalton Trans.* **2020**, *49* (45), 16348–16358. https://doi.org/10.1039/D0DT01369B.
(37) Muro-Cruces, J.; Roca, A. G.; López-Ortega, A.; Fantechi, E.; del-Pozo-Bueno, D.; Estradé, S.; Peiró, F.; Sepúlveda, B.; Pineider, F.; Sangregorio, C.; Nogues, J. Precise Size Control of the Growth of

Fe_3O_4 Nanocubes over a Wide Size Range Using a Rationally Designed One-Pot Synthesis. *ACS Nano* **2019**, *13* (7), 7716–7728. https://doi.org/10.1021/acsnano.9b01281.

(38) Hufschmid, R.; Arami, H.; Ferguson, R. M.; Gonzales, M.; Teeman, E.; Brush, L. N.; Browning, N. D.; Krishnan, K. M. Synthesis of Phase-Pure and Monodisperse Iron Oxide Nanoparticles by Thermal Decomposition. *Nanoscale* **2015**, *7* (25), 11142–11154. https://doi.org/10.1039/C5NR01651G.

(39) Feld, A.; Weimer, A.; Kornowski, A.; Winckelmans, N.; Merkl, J.-P.; Kloust, H.; Zierold, R.; Schmidtke, C.; Schotten, T.; Riedner, M.; Bals, S.; Weller, H. Chemistry of Shape-Controlled Iron Oxide Nanocrystal Formation. *ACS Nano* **2019**, *13* (1), 152–162. https://doi.org/10.1021/acsnano.8b05032.

(40) Yu, W. W.; Falkner, J. C.; Yavuz, C. T.; Colvin, V. L. Synthesis of Monodisperse Iron Oxide Nanocrystals by Thermal Decomposition of Iron Carboxylate Salts. *Chem. Commun.* **2004**, No. 20, 2306. https://doi.org/10.1039/b409601k.

(41) Mitra, A.; Mohapatra, J.; Sharma, H.; Meena, S. S.; Aslam, M. Controlled Synthesis and Enhanced Tunnelling Magnetoresistance in Oriented Fe_3O_4 Nanorod Assemblies. *J. Phys. D: Appl. Phys.* **2018**, *51* (8), 085002. https://doi.org/10.1088/1361-6463/aaa697.

(42) Unni, M.; Uhl, A. M.; Savliwala, S.; Savitzky, B. H.; Dhavalikar, R.; Garraud, N.; Arnold, D. P.; Kourkoutis, L. F.; Andrew, J. S.; Rinaldi, C. Thermal Decomposition Synthesis of Iron Oxide Nanoparticles with Diminished Magnetic Dead Layer by Controlled Addition of Oxygen. *ACS Nano* **2017**, *11* (2), 2284–2303. https://doi.org/10.1021/acsnano.7b00609.

(43) Herrera, A. P.; Polo-Corrales, L.; Chavez, E.; Cabarcas-Bolivar, J.; Uwakweh, O. N. C.; Rinaldi, C. Influence of Aging Time of Oleate Precursor on the Magnetic Relaxation of Cobalt Ferrite Nanoparticles Synthesized by the Thermal Decomposition Method. *Journal of Magnetism and Magnetic Materials* **2013**, *328*, 41–52. https://doi.org/10.1016/j.jmmm.2012.09.069.

(44) Balakrishnan, T.; Lee, M.-J.; Dey, J.; Choi, S.-M. Sub-Nanometer Scale Size-Control of Iron Oxide Nanoparticles with Drying Time of Iron Oleate. *CrystEngComm* **2019**, *21* (27), 4063–4071. https://doi.org/10.1039/C9CE00112C.

(45) Ito, S.; Inoue, K.; Mastumoto, M. $[Fe_3O(OCOR)_6L_3]^+$-Catalyzed Epoxidation of Olefinic Alcohol Acetates by Molecular Oxygen. *J. Am. Chem. Soc.* **1982**, *104* (23), 6450–6452. https://doi.org/10.1021/ja00387a051.

(46) Ertürk, E.; Göllü, M.; Demir, A. S. Efficient Rearrangement of Epoxides Catalyzed by a Mixed-Valent Iron Trifluoroacetate $[Fe_3O(O_2CCF_3)_6(H_2O)_3]$. *Tetrahedron* **2010**, *66* (13), 2373–2377. https://doi.org/10.1016/j.tet.2010.01.102.

(47) Spannring, P.; Yazerski, V.; Bruijnincx, P. C. A.; Weckhuysen, B. M.; Klein Gebbink, R. J. M. Fe-Catalyzed One-Pot Oxidative Cleavage of Unsaturated Fatty Acids into Aldehydes with Hydrogen Peroxide and Sodium Periodate. *Chem. Eur. J.* **2013**, *19* (44), 15012–15018. https://doi.org/10.1002/chem.201301371.

(48) Enferadi Kerenkan, A.; Béland, F.; Do, T.-O. Chemically Catalyzed Oxidative Cleavage of Unsaturated Fatty Acids and Their Derivatives into Valuable Products for Industrial Applications: A Review and Perspective. *Catal. Sci. Technol.* **2016**, *6* (4), 971–987. https://doi.org/10.1039/C5CY01118C.

(49) Lynch, J.; Zhuang, J.; Wang, T.; LaMontagne, D.; Wu, H.; Cao, Y. C. Gas-Bubble Effects on the Formation of Colloidal Iron Oxide Nanocrystals. *J. Am. Chem. Soc.* **2011**, *133* (32), 12664–12674. https://doi.org/10.1021/ja2032597.

(50) Sun, S.; Zeng, H.; Robinson, D. B.; Raoux, S.; Rice, P. M.; Wang, S. X.; Li, G. Monodisperse MFe_2O_4 (M = Fe, Co, Mn) Nanoparticles. *J. Am. Chem. Soc.* **2004**, *126* (1), 273–279. https://doi.org/10.1021/ja0380852.

(51) Vreeland, E. C.; Watt, J.; Schober, G. B.; Hance, B. G.; Austin, M. J.; Price, A. D.; Fellows, B. D.; Monson, T. C.; Hudak, N. S.; Maldonado-Camargo, L.; Bohorquez, A. C.; Rinaldi, C.; Huber, D. L. Enhanced Nanoparticle Size Control by Extending LaMer's Mechanism. *Chem. Mater.* **2015**, *27* (17), 6059–6066. https://doi.org/10.1021/acs.chemmater.5b02510.

(52) Singh, G.; Chan, H.; Baskin, A.; Gelman, E.; Repnin, N.; Kral, P.; Klajn, R. Self-Assembly of Magnetite Nanocubes into Helical Superstructures. *Science* **2014**, *345* (6201), 1149–1153. https://doi.org/10.1126/science.1254132.
(53) Chalasani, R.; Vasudevan, S. Form, Content, and Magnetism in Iron Oxide Nanocrystals. *J. Phys. Chem. C* **2011**, *115* (37), 18088–18093. https://doi.org/10.1021/jp204697f.
(54) Bodnarchuk, M. I.; Kovalenko, M. V.; Groiss, H.; Resel, R.; Reissner, M.; Hesser, G.; Lechner, R. T.; Steiner, W.; Schäffler, F.; Heiss, W. Exchange-Coupled Bimagnetic Wüstite/Metal Ferrite Core/Shell Nanocrystals: Size, Shape, and Compositional Control. *Small* **2009**, *5* (20), 2247–2252. https://doi.org/10.1002/smll.200900635.
(55) Pichon, B. P.; Gerber, O.; Lefevre, C.; Florea, I.; Fleutot, S.; Baaziz, W.; Pauly, M.; Ohlmann, M.; Ulhaq, C.; Ersen, O.; Pierron-Bohnes, V.; Panissod, P.; Drillon, M.; Begin-Colin, S. Microstructural and Magnetic Investigations of Wüstite-Spinel Core-Shell Cubic-Shaped Nanoparticles. *Chem. Mater.* **2011**, *23* (11), 2886–2900. https://doi.org/10.1021/cm2003319.
(56) Mitra, A.; Mohapatra, J.; Meena, S. S.; Tomy, C. V.; Aslam, M. Verwey Transition in Ultrasmall-Sized Octahedral Fe_3O_4 Nanoparticles. *J. Phys. Chem. C* **2014**, *118* (33), 19356–19362. https://doi.org/10.1021/jp501652e.
(57) Hevroni, A.; Bapna, M.; Piotrowski, S.; Majetich, S. A.; Markovich, G. Tracking the Verwey Transition in Single Magnetite Nanocrystals by Variable-Temperature Scanning Tunneling Microscopy. *J. Phys. Chem. Lett.* **2016**, *7* (9), 1661–1666. https://doi.org/10.1021/acs.jpclett.6b00644.
(58) Kim, T.; Sim, S.; Lim, S.; Patino, M. A.; Hong, J.; Lee, J.; Hyeon, T.; Shimakawa, Y.; Lee, S.; Attfield, J. P.; Park, J.-G. Slow Oxidation of Magnetite Nanoparticles Elucidates the Limits of the Verwey Transition. *Nat Commun* **2021**, *12* (1), 6356. https://doi.org/10.1038/s41467-021-26566-4.

Chapter 3

Quantifying superparamagnetic signatures in nanoparticle magnetite: a generalized approach for physically meaningful statistics and synthesis diagnostics

3.1 Introduction

Magnetization is a common measurable for characterizing bulk, nanoscale, and molecular materials, which can be quantified to high precision as a function of an applied external field. These data provide detailed information about a material's electronic structure, phase purity, and impurities, though interpreting this data can be challenging due to many contributing factors. In sub-single-domain particles of a magnetic material, an inherently time-dependent rotation of the entire particle spin becomes possible. This phenomenon, known as superparamagnetism (SPM), simultaneously represents a very early size-dependent property to be considered, while being one of the least explored in the current quantum materials era. This discrepancy is, at least in part, due to the need for models with less built-in complexity that can facilitate the generation of comparative data. In this chapter, we map an extensive dataset of variable-size SPM Fe_3O_4 (magnetite) to an intrinsic statistical model for their field-dependence. By constraining the SPM behavior to a probabilistic model, the data are apportioned to several decorrelated sources. From this, there is strong evidence that standard measures such as saturation magnetization, M_S, are poor comparative parameters, being dependent on experimental knowledge and measurement of the magnetic mass. In

contrast, parameters of the intrinsic probability distribution, such as the maximum susceptibility, χ_{max}, are far better suited to describe the SPM behavior itself and do not propagate unknown magnetic mass error. By confining the data fitting to intrinsic variables of the model distribution, scaling parameters, and linear contributions, we find greater value in magnetic data, ultimately aiding potential synthesis diagnostics and prediction of new properties and functionality.

Much of nanoscience is predicated on the idea that fundamental properties of solid-state materials undergo radical changes when reduced to the nanoscale size regime, both as the result of the outsized role of the surface and from spatial confinement of the wavefunction. The enhanced and tunable functionality possible from such changes has resulted in a rapidly expanding array of synthetic and characterization techniques, as well as more intuitive and physically accurate models. In this pursuit, chemistry has played an increasingly important role in targeting and optimizing structure-property relationships on the nanoscale. One of the most intriguing areas to build structure-property insight is in nanoscale analogues of correlated magnetic materials. Such materials display fundamentally different behavior as a result of spatial confinement, enhancing the role of phonon coupling and giving rise to superparamagnetism (SPM) - a curious blending of permanent magnetism and paramagnetism. In SPM, the sub-single-domain confinement results in a collective angular momentum state with moment $M_{\mathrm{SPM}} = \mathrm{M_S Cos}(\theta)$, where θ is the angle of rotation of the moment vector $\theta = [-\pi/2\,, \pi/2]$ with $\theta = \pm\,\pi/2$ representing the energy minima of a bistable double-well potential with spins totally aligned or anti-aligned. In this framework, the ground state is defined by an energetically isolated manifold of coupled spins known as a macro- or superspin. The macrospin has a collective spin that scales with the particle volume and takes on a time-dependent, high susceptibility switching behavior that is sensitive to a wide range of interactions and chemical modifications. Effectively, the SPM particle acts as a Curie paramagnet with a moment equivalent to the net moment of all contributions of the SPM nanoparticle, often $10^4 - 10^5\ \mu_B$. The switchable nature of SPM finds applications at the intersections of many diverse fields[1] such as biomedicine,[2] electronics,[3,4] sensing,[5] imaging,[6] rheology,[7] and catalysis.[8] With energy concerns driving the need for higher performance

and materials scarcity driving efforts to diversify component resources, the need for understanding, control, and quantification of magnetic materials is extant.

Herein, we demonstrate how the stochastic nature of SPM can be leveraged in a general, physically meaningful model wherein the field-dependent magnetization curve is treated as a parameterized cumulative distribution function, *F(x)*, of a Cauchy distribution (also known as the Lorentz or Cauchy-Lorentz distribution). Within this framework, we can decorrelate the intrinsic distribution of particle spin alignments from overall scaling and background paramagnetism. This method is designed to generate a consistent parameter space across samples displaying SPM to extract consistent, intuitive, and quantitative information from samples collected under a variety of conditions and with various imperfections. In essence, it acts as a pre-processing step to categorize parameters by their origin and constraints, dramatically reducing the noise in any further modeling based on specific quantum mechanical models. In a useful example, we demonstrate how peakshape parameters such as the maximum susceptibility, χ_{max}, display a consistent linear trend with magnetic particle size while scaling parameters such as saturation magnetization, M_S do not.

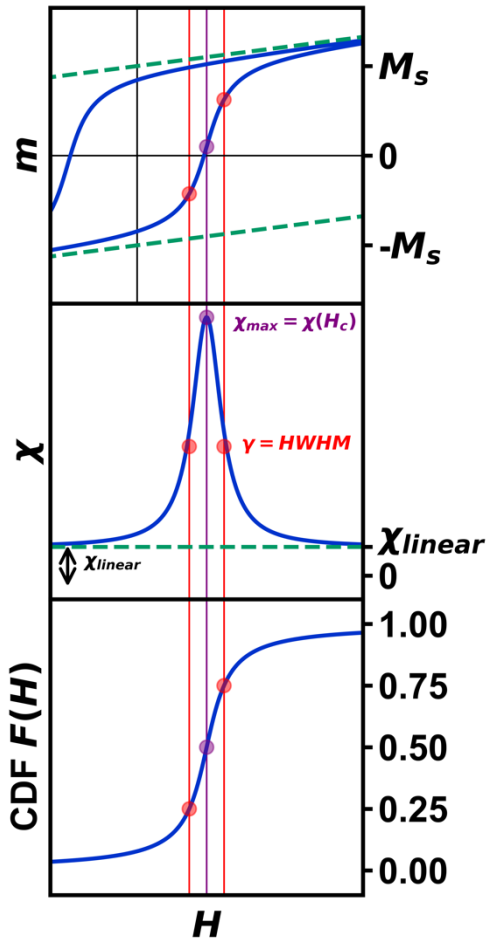

Figure 3.1. Magnetization curves (top), differential magnetization (χ) curve (middle), and corresponding Cauchy CDF (bottom). The effect of χ_{linear} (green dashed line) is demonstrated in the magnetization curve, as it obscures both the true saturation magnetization (M_s) and coercive field (H_c), however, it is depicted more clearly as the vertical offset of the differential magnetization curve at $H = \pm\infty$. Stemming purely from the statistical model, γ is represented in red as the half-width at half-max (HWHM). The susceptibility at H_c, denoted χ_{max}, is represented in purple.

Arguably the most common and information-rich characterization method of bulk, nanoscale, and molecular magnetic materials is the measurement of magnetization as a function of an external magnetic field (Figure 3.1; Figure 3.6). In nanomaterials, specific models have been employed to interpret magnetic moment vs. magnetic field in terms of structure[9,10] and degree of crystallinity,[11–13] as well as nanoscale-specific properties such as size,[14,15] shape,[16,17] and surface.[18,19]

In many cases, the correlation of properties with fit parameters depends strongly on the specifics of the material and sample form, making broad comparisons across many samples difficult. At the heart of

the difficulty in applying generalizable models to nanoscale magnetism, especially colloidal nanoparticles, is the meaningful treatment of rapidly fluctuating forces arising from non-uniform physical systems (i.e., particle distributions). Modeling complex data as a combination of both deterministic and stochastic forces is often achieved via solutions to stochastic differential equations. For example, the effect of particle size dispersity can be modeled through a lognormal distributed function. The most common solution to a Langevin equation used in magnetism corresponds to the macrospin limit ($\vec{J} \rightarrow \infty$) of the Brillouin equation for saturation behavior of a discrete magnetic angular momentum vector, $\vec{J}$. The macrospin approximation of the SPM, however, means that the moment vs. external field behavior is better estimated as the net sum of the moment-weighted populations of fully aligned and anti-aligned states. From this standpoint, a magnetic field sweep can be re-normalized in the form of a cumulative distribution function (CDF; *F(H)*). This CDF describes a large population of macrospins aligned in one field direction changing their equilibrium population as field is swept until the equilibrium lies fully in the other direction. Due to the equilibrium nature of the system, the CDF endpoints of 0 and 1 are only reached at fields of $H = \pm\infty$. The use of such a model for data modeling and comparative analysis is of interest because any parameter distribution associated with it can be assigned to the intrinsic SPM behavior and is subject to the constraints of the distribution.

The Cauchy distribution (Figure 3.7) is a continuous, stable probability distribution that conforms to the requirements detailed above. Its cumulative distribution function (Figure 3.1, Equation 3.1) and probability density function (PDF; Equation 3.2) are modified by the location parameter, x_0, and the scale parameter, γ.[20] As a stable distribution, the Cauchy distribution has applications in chemistry and physics,[21–23] geology,[24] engineering,[25] and economics.[26]

$$F(x; x_0, \gamma) = \frac{1}{\pi} arctan\left(\frac{x - x_0}{\gamma}\right) + \frac{1}{2} \qquad \text{Equation 3.1}$$

$$f(x; x_0, \gamma) = \frac{1}{\pi}\left[\frac{\gamma}{(x - x_0)^2 + \gamma^2}\right] \qquad \text{Equation 3.2}$$

$$M(H;\ H_c, \gamma\ ) = \frac{2M_s}{\pi} arctan\left(\frac{H - H_c}{\gamma}\right) + \chi_{linear} H \qquad \text{Equation 3.3}$$

All data reported herein is fit to the CDF of an underlying Cauchy distribution that is scaled proportional to M_s with an additive parameter $\chi_{linear}H$, where $\chi_{linear}H$ is a susceptibility term accounting for the sum response from paramagnetic and diamagnetic components. To extract consistent and quantitative information, the Cauchy distribution model is presented to provide insight into intrinsic SPM behavior. This model provides a material-independent formalism for standardized data collection and comparison, as well as a method for pre-processing data for validation and further analysis via deterministic models.

3.2 Results and discussion

3.2.1 Synthesis and physical characterization of iron oxide nanoparticles

Magnetite (Fe_3O_4) nanoparticles have a high magnetization and superparamagnetic susceptibility over a wide size range, making them desirable targets for magnetic optimization towards numerous applications.[27] Magnetite nanoparticle samples of varying size (d = 5 – 12 nm) were synthesized according to our previously described method (Figure 3.2a, Figure 3.8a-e, Table 2.4).[15] The percent relative standard deviation (%RSD) among all samples exhibits a notable degree of consistency, falling between 9.88% and 12.97%. Briefly, a stoichiometric powder form of iron oleate was used in the high temperature decomposition of iron oleate with octadecene and oleic acid as the solvent and surfactant, respectively. To avoid the commonly observed issue of overreduction of magnetite (Fe_3O_4) to wüstite (FeO), 5% O_2 was flowed through the reaction during the reflux stage. One particularly difficult aspect of modeling SPM nanoparticle magnetization is the detection and quantification of interparticle interactions. To probe the effect of interparticle interactions, silica shells were grown onto each set of magnetite nanoparticles (Figure 3.2b) through a previously described reverse microemulsion procedure.[28] Briefly, silica shells were grown onto Fe_3O_4 by the hydrolysis of tetraethylorthosilicate (TEOS) in microemulsions of aqueous ammonia in cyclohexane. Empty silica shells further prevent interparticle interactions. The average diameter was determined via TEM. Magnetite phase purity was confirmed by pXRD (Figure 3.9). Finally, to account for

variability in surface ligand mass by sample, Thermogravimetric Analysis (TGA) was carried out from 30 °C to 1000 °C under air (Figure 3.10, Figure 3.11, Table 3.3).

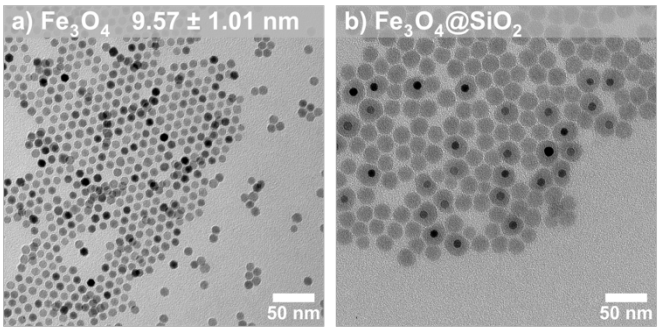

Figure 3.2. TEM images (a) 9.57 nm Fe_3O_4 nanoparticles and (b) Fe_3O_4@SiO_2 nanoparticles.

3.2.2 Magnetic characterization of iron oxide nanoparticles

Magnetization vs. magnetic field studies (Figure 3.3a-b) were conducted on all Fe_3O_4 and Fe_3O_4@SiO_2 samples ($H = -7$ to 7 T; $T = 300$ K). A calibration of the magnetic field was carried out using a palladium standard with a precisely known susceptibility. This step is necessary for precise measurement of the low-field magnetization, as remnant fields of approximately ±30 Oe in the superconducting magnet can fluctuate over time. This small residual field leads to a difference between the recorded and true fields, resulting in an "inverted" hysteresis loop and false coercivities (details in Experimental Details). An interpolation was performed on the forward sweep of each curve, generating evenly spaced points to prevent biasing, then fit to Equation 3.3 for further analysis (Table 3.1). The derivative, dM/dH of the fit function from each data set (Figure 3.3d-e) represents the instantaneous magnetic susceptibility as a function of magnetic field. Visualizing dM/dH (proportional to the Cauchy PDF and also known as a Lorentzian lineshape) can be advantageous for various applications, such as Magnetic Particle Imaging (MPI),[29] and provides intuition about parameters typically neglected in SPM analysis. These parameters include the maximum superparamagnetic susceptibility, χ_{max}, (Figure 3.3f), γ, (Figure 3.3g) and χ_{linear}, the y-axis offset of dM/dH vs. H at $H = \pm\infty$ (Figure 3.1). While some amount of χ_{linear} is common due to decoupled spins

at the particle surface, from defects, or from molecular impurities, these effects are typically only observable at fields where the SPM macrospin is fully saturated.

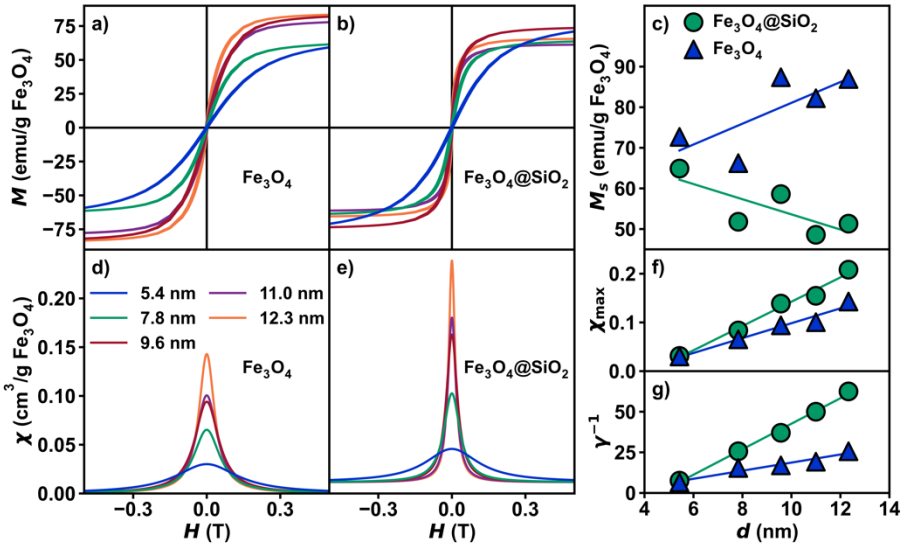

Figure 3.3. Magnetic properties. Plots of isothermal magnetization vs. magnetic field for (a) Fe_3O_4 and (b) Fe_3O_4@SiO_2 at 300 K. (c) Plot of saturation magnetization vs. nanoparticle diameter (nm). Plots of derivative to fit (magnetic susceptibility) vs. magnetic field for (d) Fe_3O_4 and (e) Fe_3O_4@SiO_2 at 300 K. (f) Plots of χ_{max} vs. nanoparticle diameter (nm) and (g) γ^{-1} vs. nanoparticle diameter (nm).

One of the most interesting points to emerge from our quantification of SPM magnetization data by the Cauchy distribution function was the lack of conformity of the saturation magnetization, M_S to a distinct size trend. The size of the macrospin is expected to increase linearly with particle volume in the SPM regime, and we observe only a very weak trend (Figure 3.3c). In a general sense, an increase in saturation magnetization with nanoparticle diameter is observed for the bare Fe_3O_4 nanoparticles, while a slight decrease in saturation magnetization with diameter is observed in Fe_3O_4@SiO_2. This difference in behavior could be attributed to surface effects at the interface between the two materials, although due to the effect of sample mass error, it is important to exercise caution when considering saturation magnetization. The difference in error of the sample mass is roughly 10^2 times larger than the error in magnetic moment. To demonstrate the effect of error, 1000 samples following randomized normal distributions in magnetic moment and mass with corresponding typical errors were generated and plotted as a histogram of magnetic moment per gram (Figure 3.12). For these reasons, parameters based on

susceptibility (γ, γ^{-1}, χ_{max}, χ_{linear}) can supplement saturation magnetization to better describe the overall magnetic properties of SPM nanoparticles. The use of susceptibility-based terms is demonstrated in Figure 3.3f and Figure 3.3g, as both χ_{max} and γ^{-1} exhibit a strong linear dependence on nanoparticle diameter. By comparison, only a weak trend is evident in M_s vs. d in (Figure 3.3c), highlighting that γ is determined from the distribution function only and thus decorrelated from the scaling of the magnetization curve.

The effect of interparticle interactions via dipolar coupling is commonly neglected in measurements of nanoparticle SPM due to assumptions about its relative strength or how the behavior should manifest. It has been shown that the introduction of large silica shells can drastically reduce interparticle interactions compared to other methods. Indeed, from our ZFC-FC measurement, stark differences are observed between interacting vs. non-interacting samples (Figure 3.13). While non-interacting Fe_3O_4 nanoparticles are expected to exhibit a rise in the FC curve with decreasing temperature below the blocking temperature, as dipolar coupling strength increases, Fe_3O_4 nanoparticles (e.g., randomly-close-packed powder assemblies) will exhibit a slight dip in the FC curve below the blocking temperature.[32,33] Additionally, the non-interacting case results in a sharper ZFC curve. All five Fe_3O_4@SiO_2 lack signatures of interparticle interactions, confirmed by the rise in the FC curves below the blocking temperature and a significant enhancement in peak sharpness (Figure 3.14b). To compare both nanoparticle sets, the Fe_3O_4 mass percentage in Fe_3O_4@SiO_2 was determined by EDX (Table 3.3). In applications such as MPI and granular magnetoresistance, the sharpness of the magnetization curve directly correlates with performance. In the absence of dipolar coupling, χ_{max} and γ^{-1} increase across all sizes, indicating a sharpening of the dM/dH peak. For example, the 12.3 nm sample exhibits an increase in χ_{max} of 106 % between Fe_3O_4 and Fe_3O_4@SiO_2.

Table 3.1. Magnetic hysteresis loop fit parameters to Cauchy distribution.

Fe_3O_4						
Size (nm)	**M_s (emu/g Fe_3O_4)**	**H_c (Oe)**	**γ**	**χ_{linear} (cm^3/g Fe_3O_4)**	**χ_{max} (cm^3/g Fe_3O_4)**	**χ^2 of fit**
5.43	72.69	0.40	0.154	-3.77×10^{-6}	0.030	941.5
7.83	66.22	0.80	0.065	-7.34×10^{-6}	0.065	1562.7
9.57	87.38	1.23	0.059	-1.27×10^{-5}	0.094	5247.7
11.00	82.21	0.91	0.052	-1.40×10^{-5}	0.101	3894.1
12.33	86.95	1.76	0.039	-8.05×10^{-6}	0.143	2051.2
$Fe_3O_4@SiO_2$						
Size (nm)	**M_s (emu/g Fe_3O_4)**	**H_c (Oe)**	**γ**	**χ_{linear} (cm^3/g Fe_3O_4)**	**χ_{max} (cm^3/g Fe_3O_4)**	**χ^2 of fit**
5.43	64.89	-0.08	0.132	-2.89×10^{-5}	0.031	222.1
7.83	51.79	-0.07	0.039	-1.48×10^{-4}	0.083	27.3
9.57	58.60	0.36	0.027	-1.05×10^{-4}	0.139	32.5
11.00	48.58	0.47	0.020	-1.29×10^{-4}	0.155	120.9
12.33	51.32	0.80	0.016	-6.35×10^{-5}	0.208	317.3

As a test of the trends observed with χ_{max} and γ^{-1}, an analysis across a larger dataset was performed (Figure 3.4, Table 3.4). An identical analysis was conducted using 22 Fe_3O_4 samples, synthesized over a period of two years with variations in iron oleate synthetic methods, and with diameters ranging from 4 nm to 14 nm. Each 300 K magnetization curve was fit to Equation 3.3. In a similar fashion to the smaller dataset, the larger dataset also exhibits a weak dependence of M_s on diameter ($R^2 = 0.37$) with a stronger relationship of χ_{max} ($R^2 = 0.88$) and γ^{-1} ($R^2 = 0.88$) vs. diameter, thus demonstrating the viability of this method. The collection, analysis, and statistical modelling of large datasets holds the potential to uncover previously unobserved trends in magnetic nanoparticles and help identify impurities,

phase mixtures, multi-domain relaxation effects, and other synthetic challenges often obscured by qualitative or overly parameterized models.

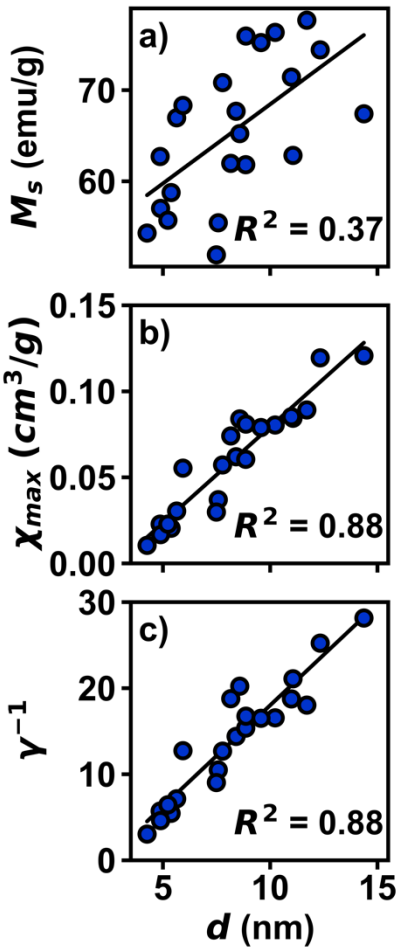

Figure 3.4. Plots of magnetic parameters for large dataset of Fe_3O_4 nanoparticles, plotted in per g of sample. (a) Plot of M_s vs. d. (b) Plot of χ_{max} vs. d. (c) Plot of γ^{-1} vs. d.

Following the strong trend of maximum magnetic susceptibility as a function of diameter, the ability to predict and target specific magnetic properties can become trivial. This may prove useful in biological and sensing applications requiring maximal magnetic susceptibility response within a targeted field range. For example, in MPI, the parameter (HWFM of χ vs. d) is indicative of spatial resolution.[29] Another example is in nanocomposite magnetoresistance, where predicting the structure-property relationship correlates with magnetoresistance percentage and curve shape.[4]

As previously discussed, superparamagnetic nanoparticles are typically characterized with their native long-chain ligands present and thus contain a significant percentage (10-25 % w/w) of diamagnetic organic material. The presence of diamagnetic material is wholly accounted for by the linear susceptibility term, χ_{linear}. Therefore, any diamagnetic contribution can be effectively subtracted out, leaving just the contribution from the SPM portion. This concept is also observed in the Fe_3O_4@SiO_2 samples, as the diamagnetic contribution from silica is entirely accounted for with χ_{linear}.

Extending this concept to multiple independent SPM signals, the Cauchy method can deconvolute contributions from magnetic materials beyond the simple case of neat oleate bound and silica shelled iron oxide nanoparticles. While any sum of Cauchy distributions within an isolated particle will form a single Cauchy distribution (e.g., representing a more complex energy manifold), a separate, population of isolated magnetic components with different properties will be represented with a unique Cauchy function. To show this experimentally, a physical mixture was made with 5.4 nm Fe_3O_4@SiO_2 and 12.3 nm Fe_3O_4@SiO_2 to simulate a bimodal distribution that can result from colloidal synthesis. Contributions from each sample are observed in the ZFC-FC measurement (Figure 3.5a). The magnetization curve was fit to a linear combination of two unique Cauchy functions (Figure 3.5b) modified by a term, p, to account for the relative ratio of each component. The plot of magnetic susceptibility vs. magnetic field (Figure 3.5c) of the mixture demonstrates that two unique distributions are necessary to fully describe the magnetization curve, while a single Cauchy CDF is a poor fit (Figure 3.15). A test for multiple distribution fits to interpret magnetization data may prove useful in applications beyond the SPM nanoparticles studied in this work. At minimum, it can help to prevent misinterpretation of mixed samples where qualitative interpretation of the data may result in poor conclusions and perpetuate synthetic difficulties.

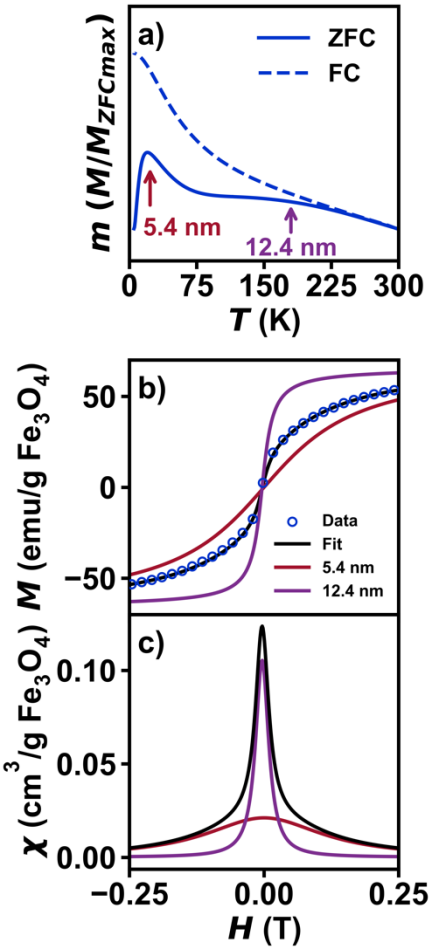

Figure 3.5. Magnetic data for a physical mixture of 5.4 nm Fe_3O_4@SiO_2 and 12.3 nm Fe_3O_4@SiO_2. (a) Plot of normalized zero-field cooled magnetization vs. temperature from 5-300 K under an applied field of 0.01 T. (b) Plot of isothermal magnetization vs. magnetic field for the physical mixture. The fit is shown in black, with contributions from 5.4 nm and 12.3 nm shown in red and purple, respectively. The fit was carried out using a sum of two unique Cauchy functions, with a relative ratio between the two, p, as an additional fit parameter. The γ and H_c parameters from the individual samples were held constant, while M_s and χ_{linear} were allowed to vary to account for mass errors. (c) Plot of magnetic susceptibility vs. magnetic field, with contributions from the 5.4 nm and 12.3 nm shown in blue and orange, respectively. and (e) Fe_3O_4@SiO_2 at 300 K. (f) Plots of χ_{max} vs. nanoparticle diameter and γ^{-1} vs. nanoparticle diameter.

3.3 Conclusions

In this chapter, statistical modelling is shown to improve the quantification of experimentally complex data of SPM nanoparticles. A generalized curve-fitting model is demonstrated based on the Cauchy distribution to better describe the overall magnetization curve. The preservation of underlying

statistics is imperative for making accurate comparisons between datasets, with the potential to discover stronger trends, built upon new models, ultimately aiding material design.

3.4 Experimental details

3.4.1 Materials

The reagents used were iron (III) chloride hexahydrate (97% Alfa Aesar), iron (II) chloride tetrahydrate (97% Fisher), sodium oleate (97% TCI), oleic acid (90%, Alfa Aesar) and 1-octadecene (90% Sigma Aldrich). ACS grade hexane, ethanol, and methanol were purchased from Fisher. Oleic acid was degassed and stored under vacuum in a Schlenk flask covered with aluminum foil. All other chemicals were used as received.

3.4.2 Synthesis of iron oleate

Iron oleate in its powder form was synthesized according to a previous literature procedure described in Chapter 2.[15]

3.4.3 Nanoparticle synthesis from iron oleate (FeOl)

Fe_3O_4 nanoparticles were synthesized and purified according to a previous literature procedure described in Chapter 2.[15]

3.4.4 Synthesis of Fe_3O_4@SiO_2 nanoparticles

Silica shelled iron oxide nanoparticles were synthesized in a reverse microemulsion method according to a literature procedure.[28] In a typical synthesis, 17 mL Igepal CO-520 was stirred in a 20 mL scintillation vial for two minutes, followed by the addition of 0.8 mg Fe_3O_4 nanoparticles in hexanes (1-10 mg/mL Fe_3O_4 dispersion in hexanes). Next, 0.13 mL NH_4OH was added dropwise, and the solution was stirred for five minutes, followed by the addition of 0.15 mL tetraethylorthosilicate (TEOS). The reaction

was capped and allowed to stir at room temperature for 72 hours. The final purification step consists of a of an initial flocculation with methanol, centrifugation (7 minutes at 8500 rpm), redispersion in ethanol, flocculation with hexanes, and a final centrifugation step (7 minutes at 8500 rpm) to recover the Fe_3O_4@SiO_2 nanoparticles.

3.4.5 Characterization

Transmission electron microscopy was carried out using a FEI Spirit TEM operating at 120 kV, with images collected by a 2k x 2k Gatan CCD camera. TEM samples were prepared by drop-casting and air drying a dilute solution of nanoparticles in hexanes onto a carbon-coated copper TEM grid. Particles were analyzed in ImageJ using the default thresholding algorithm of sample sizes exceeding 1000 particles for all syntheses.

Powder X-ray diffraction was performed with a Bruker D8 Advance diffractometer using a Bruker Apex II Ultra CCD using Mo Kα (λ = 0.71073 Å) radiation.

Thermogravimetric analysis was carried out using a SDT650 instrument. Samples (10-20 mg) were loaded into a 90 μL alumina pan and heated under air from 30 °C to 1000 °C. The conversion of Fe_3O_4 to Fe_2O_3 was accounted for and confirmed via powder X-ray diffraction.

Energy dispersive X-ray analysis was performed on a Zeiss Sigma 500 SEM instrument operating at 15 kV. Samples were prepared by dropping powdered Fe_3O_4@SiO_2 samples onto conductive carbon tape. Each sample was analyzed at three locations on the stub for a minimum of 200 seconds each.

Magnetic measurements were carried out using a Quantum Design MPMS3 SQUID magnetometer. Nanoparticle samples were dried to a fine powder (1-2 mg), loaded into a VSM sample holder, and secured in a plastic straw. A calibration of the magnetic field was carried out using the palladium standard supplied by Quantum Design with a precisely known susceptibility, a necessary step to remove small remnant fields in the superconductive magnet. This small residual field leads to a difference between the recorded and true fields, resulting in an “inverted” hysteresis loop and an incorrect coercivity. Further details for this calibration are found in Quantum Design Application Notes.[34,35]

Fitting of the magnetization curves were performed in Python. To remove emphasis on any particular portion of the magnetization curve, a linear interpolation was performed on the forward sweep of the magnetization curve, generating 10,000 equally spaced points. Fitting was carried out using the default least squares method of the LMFIT package according to the initial values and constraints below. The data and code for this analysis can be found at DOI: 10.5281/zenodo.7987572.

3.5 Additional information

Table 3.2. Summary of synthesis parameters for Fe_3O_4 nanoparticles.

Size (nm)	Stdev	FeOl (g)	OA (g)	ODE (g)
5.43	0.62	0.50	0.78	6.40
7.83	1.05	0.25	0.29	7.10
9.57	1.01	1.00	0.77	5.87
11.00	1.08	1.00	1.16	6.48
12.33	1.61	0.50	0.39	6.78

Table 3.3. Iron oxide percentages for Fe_3O_4 and Fe_3O_4@SiO_2 nanoparticles.

	Fe_3O_4 (native oleate ligands)	Fe_3O_4@SiO_2
Size (nm)	**Fe_3O_4 % (w/w)**	**Fe_3O_4 % (w/w)**
5.43	74.862	8.742
7.83	79.733	2.315
9.57	86.115	3.996
11.00	86.920	2.618
12.33	85.611	5.357

Table 3.4. Magnetic hysteresis loop fit parameters to Cauchy distribution for large dataset.

Size (nm)	M_s (emu/g Fe_3O_4)	γ	χ_{linear} (cm^3/g Fe_3O_4)	χ_{max} (cm^3/g Fe_3O_4)
4.26	54.33	0.329	9.17×10^{-7}	0.011
4.87	62.73	0.175	8.93×10^{-6}	0.023
4.89	57.04	0.217	-1.58×10^{-5}	0.017
5.23	55.73	0.155	-3.36×10^{-5}	0.023
5.38	58.77	0.183	1.32×10^{-5}	0.020
5.64	66.96	0.140	-3.72×10^{-7}	0.030
5.93	68.33	0.079	-5.56×10^{-6}	0.055
7.49	51.94	0.111	5.10×10^{-6}	0.030
7.58	55.46	0.095	3.00×10^{-6}	0.037
7.78	70.83	0.079	-7.43×10^{-6}	0.057
8.16	61.97	0.053	-1.29×10^{-6}	0.074
8.41	67.69	0.069	-4.83×10^{-6}	0.062
8.58	65.23	0.049	-8.82×10^{-6}	0.084
8.86	61.83	0.065	4.88×10^{-5}	0.061
8.87	75.94	0.060	-2.44×10^{-6}	0.081
9.57	75.22	0.061	-1.02×10^{-5}	0.079
10.23	76.33	0.060	-1.03×10^{-5}	0.080
10.99	71.44	0.053	-1.15×10^{-5}	0.085
11.06	62.84	0.047	-6.87×10^{-6}	0.084
11.71	77.67	0.055	-1.26×10^{-6}	0.089
12.33	74.42	0.040	-6.39×10^{-6}	0.119
14.37	67.40	0.036	-3.40×10^{-6}	0.121

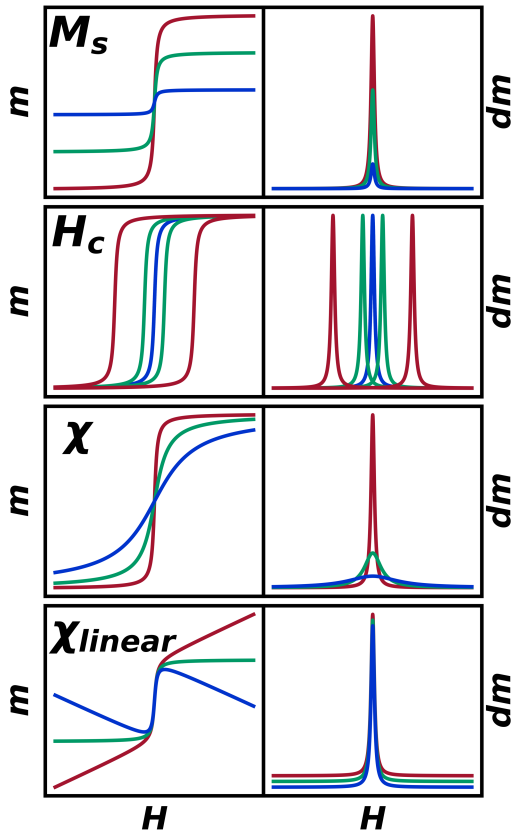

Figure 3.6. Magnetization curves (left) and corresponding differential magnetization curves (right) with varying parameters of M_s, H_c, χ, H_c, and χ_{linear}.

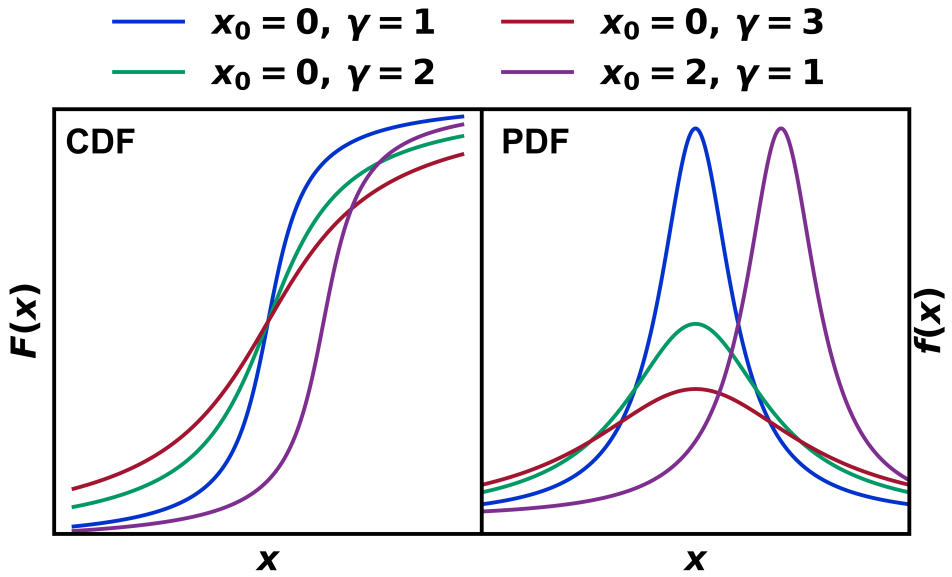

Figure 3.7. Cauchy distribution with varying location parameters (x_0) and scale factor (γ) in its (a) cumulative distribution function (CDF) form and (b) probability distribution function (PDF) form.

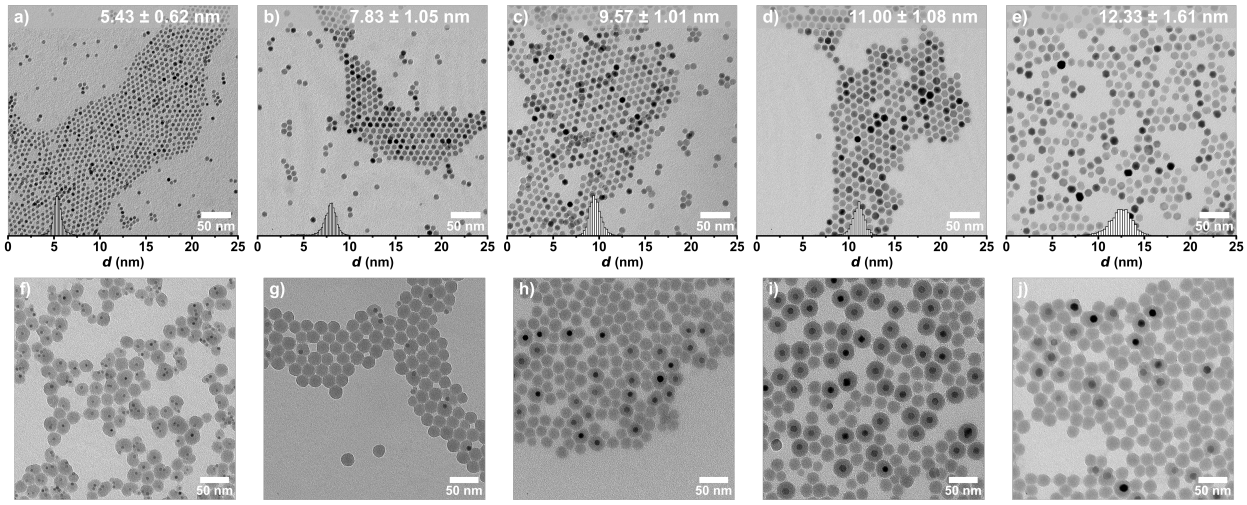

Figure 3.8. TEM images of (a-e) Fe_3O_4 nanoparticles and (f-j) Fe_3O_4@SiO_2 nanoparticles.

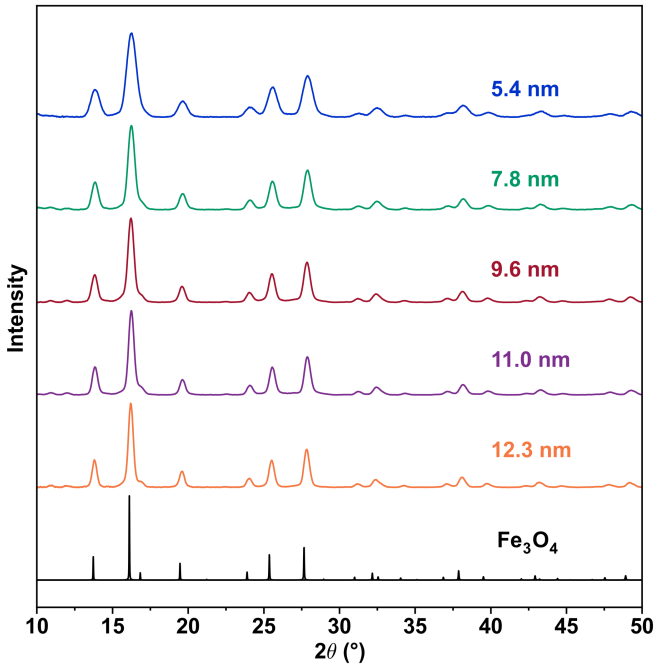

Figure 3.9. Powder X-ray diffraction (PXRD) patterns for the five Fe_3O_4 nanoparticle sizes, collected using a Mo Kα (l = 0.71073 Å) source.

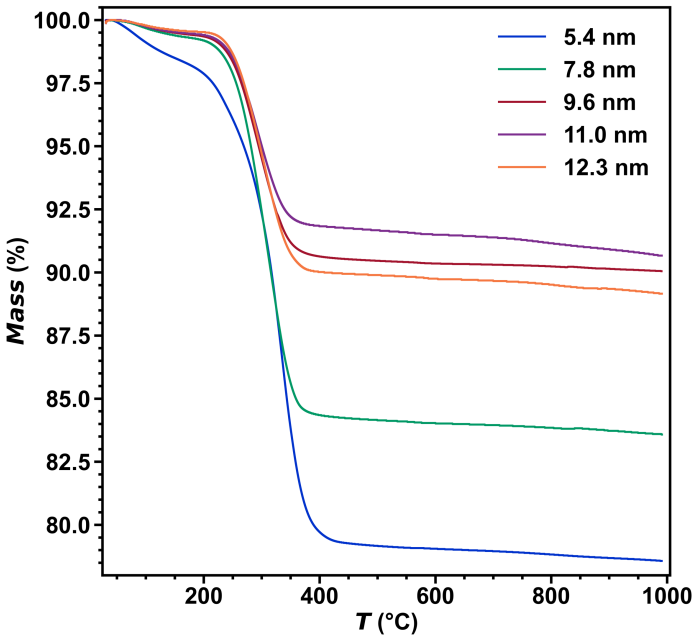

Figure 3.10. Thermogravimetric analysis (TGA) for the five Fe_3O_4 nanoparticle sizes, collected under air from 30 °C to 1000 °C at 10 °C/min. The Fe_3O_4 mass percentage was calculated after accounting for the 3.40% mass increase for the conversion of Fe_3O_4 to Fe_2O_3.

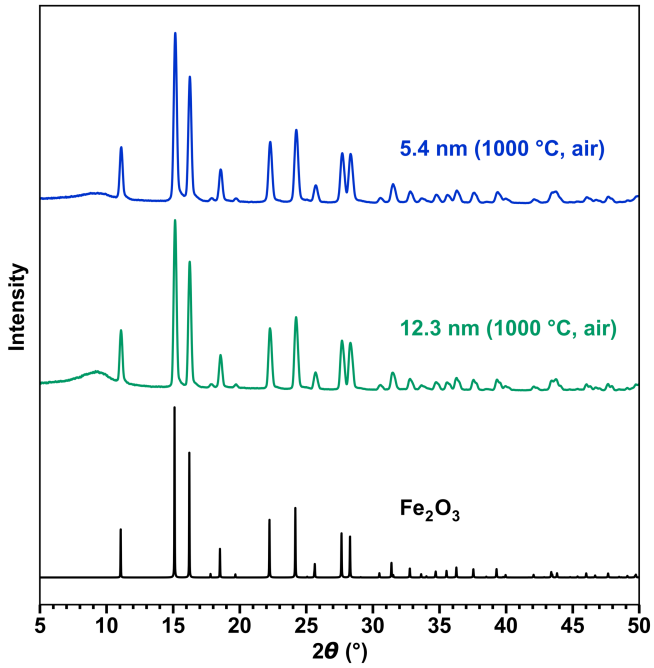

Figure 3.11. Powder X-ray diffraction (PXRD) patterns after TGA (Figure 3.10) for the 5.4 nm and 12.3 nm samples, collected using a Mo Kα (l = 0.71073 Å) source.

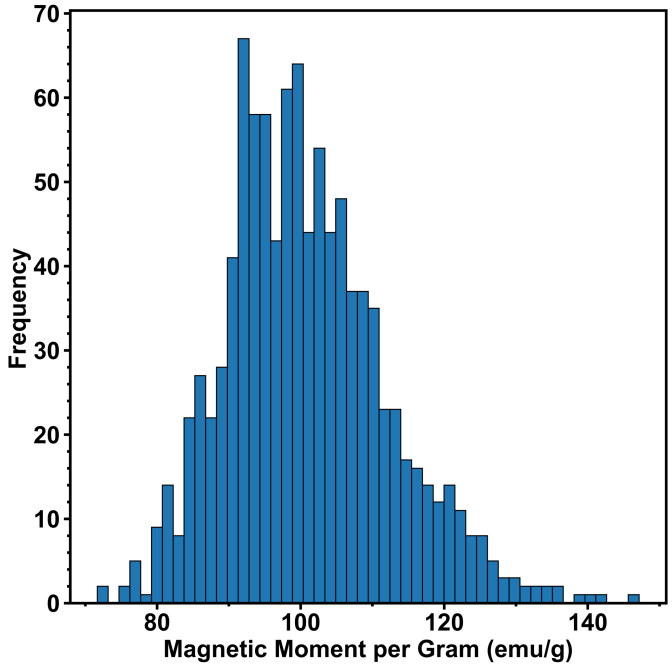

Figure 3.12. Histogram of magnetic moment per gram generated with 1000 samples following randomized normal distributions in both mass and magnetic moment. Typical values with a mass of 1.0 ± 0.1 mg and a magnetic moment of 0.1 ± 0.005 emu were used.

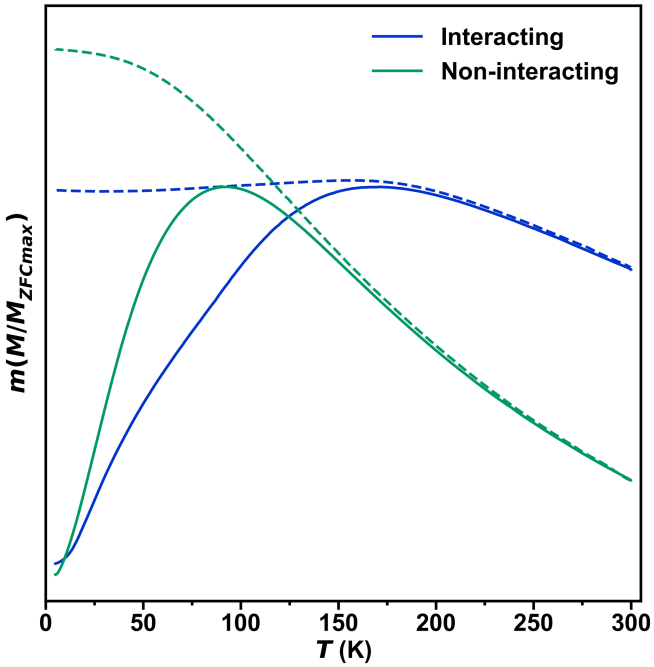

Figure 3.13. Plots of normalized zero-field cooled magnetization (solid) and field cooled magnetization vs. temperature (dashed) from 5-300 K for a nanoparticle system containing interparticle interactions (blue) and no interparticle interactions (green).

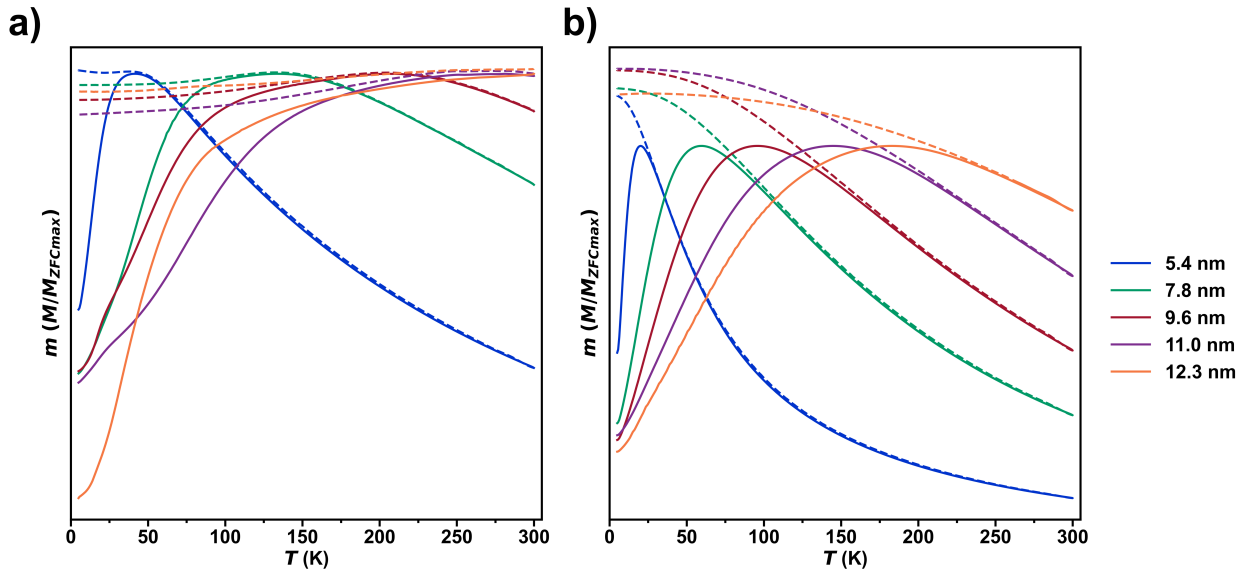

Figure 3.14. Plots of normalized zero-field cooled magnetization (solid) and field cooled magnetization (dashed) vs. temperature from 5-300 K under an applied field of 0.01 T for (a) Fe_3O_4 and (b) Fe_3O_4@SiO_2.

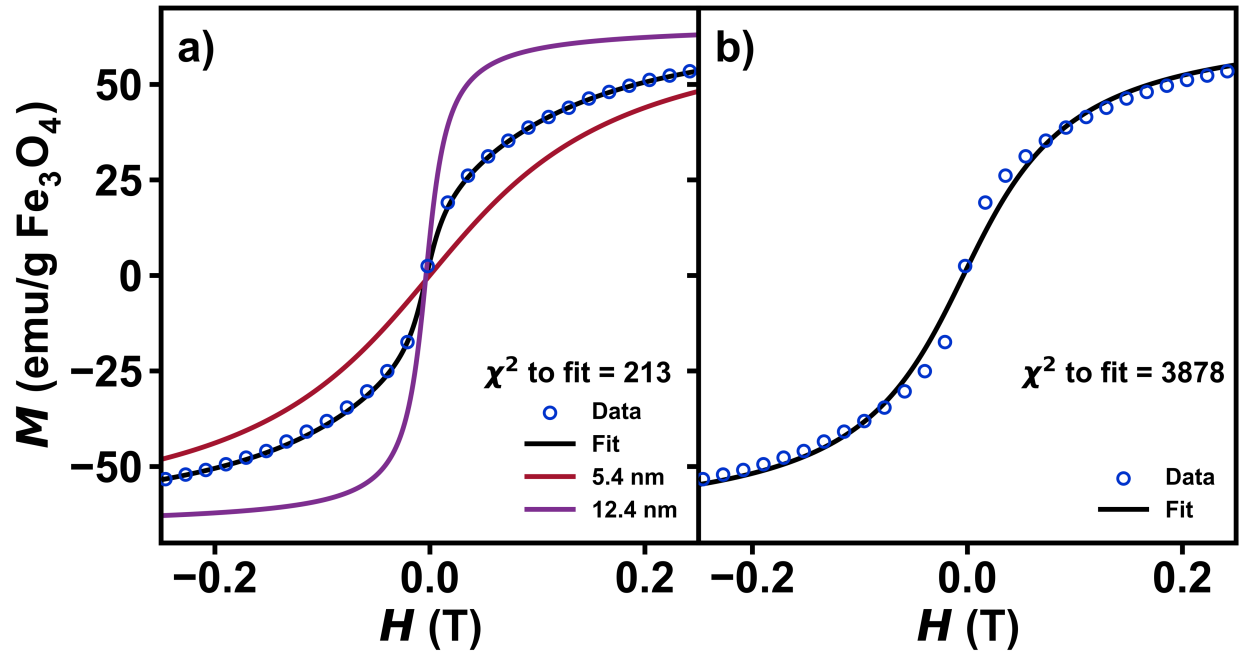

Figure 3.15. Magnetization curves for a physical mixture of 5.4 nm Fe_3O_4@SiO_2 and 12.3 nm Fe_3O_4@SiO_2. (a) Plot of isothermal magnetization vs. magnetic field for the physical mixture. The fit is shown in black, with contributions from 5.4 nm and 12.3 nm shown in red and purple, respectively. The fit was carried out using a sum of two unique Cauchy functions, with a relative ratio between the two, p, as an additional fit parameter. The γ and H_c parameters from the individual samples were held constant, while M_s and χ_{linear} were allowed to vary to account for mass errors. (b) Plot of isothermal magnetization vs. magnetic field for the mixture with fit to a single Cauchy function.

3.6 Acknowledgements

Chapter 3, in full, is a reformatted reprint from the manuscript entitled "Quantifying Superparamagnetic Signatures in Nanoparticle Magnetite: A Generalized Approach for Physically Meaningful Statistics and Synthesis Diagnostics" by Kirkpatrick, K. M.; Zhou, B. H.; Bunting, P. C.; Rinehart, J. D. The dissertation author was a primary researcher and author of this paper. Reprinted with permission from *Chem. Sci.* **2023**, *14* (27), 7589–7594. Reproduced with permission from the Royal Society of Chemistry.

3.7 References

(1) Zhu, K.; Ju, Y.; Xu, J.; Yang, Z.; Gao, S.; Hou, Y. Magnetic Nanomaterials: Chemical Design, Synthesis, and Potential Applications. *Acc. Chem. Res.* **2018**, *51* (2), 404–413. https://doi.org/10.1021/acs.accounts.7b00407.

(2) Wallyn; Anton; Vandamme. Synthesis, Principles, and Properties of Magnetite Nanoparticles for In Vivo Imaging Applications—A Review. *Pharmaceutics* **2019**, *11* (11), 601. https://doi.org/10.3390/pharmaceutics11110601.

(3) Zhou, B. H.; Rinehart, J. D. A Size Threshold for Enhanced Magnetoresistance in Colloidally Prepared $CoFe_2O_4$ Nanoparticle Solids. *ACS Cent. Sci.* **2018**, *4* (9), 1222–1227. https://doi.org/10.1021/acscentsci.8b00399.

(4) Zhou, B. H.; Rinehart, J. D. Pseudo Spin Valve Behavior in Colloidally Prepared Nanoparticle Films. *ACS Appl. Electron. Mater.* **2019**, *1* (7), 1065–1069. https://doi.org/10.1021/acsaelm.9b00196.

(5) Gloag, L.; Mehdipour, M.; Chen, D.; Tilley, R. D.; Gooding, J. J. Advances in the Application of Magnetic Nanoparticles for Sensing. *Adv. Mater.* **2019**, *31* (48), 1904385. https://doi.org/10.1002/adma.201904385.

(6) Yu, E. Y.; Bishop, M.; Zheng, B.; Ferguson, R. M.; Khandhar, A. P.; Kemp, S. J.; Krishnan, K. M.; Goodwill, P. W.; Conolly, S. M. Magnetic Particle Imaging: A Novel in Vivo Imaging Platform for Cancer Detection. *Nano Lett.* **2017**, *17* (3), 1648–1654. https://doi.org/10.1021/acs.nanolett.6b04865.

(7) Kole, M.; Khandekar, S. Engineering Applications of Ferrofluids: A Review. *Journal of Magnetism and Magnetic Materials* **2021**, *537*, 168222. https://doi.org/10.1016/j.jmmm.2021.168222.

(8) Kumar, P.; Tomar, V.; Kumar, D.; Joshi, R. K.; Nemiwal, M. Magnetically Active Iron Oxide Nanoparticles for Catalysis of Organic Transformations: A Review. *Tetrahedron* **2022**, *106–107*, 132641. https://doi.org/10.1016/j.tet.2022.132641.

(9) Sharifi Dehsari, H.; Ksenofontov, V.; Möller, A.; Jakob, G.; Asadi, K. Determining Magnetite/Maghemite Composition and Core–Shell Nanostructure from Magnetization Curve for Iron Oxide Nanoparticles. *J. Phys. Chem. C* **2018**, *122* (49), 28292–28301. https://doi.org/10.1021/acs.jpcc.8b06927.

(10) Wu, L.; Shen, B.; Sun, S. Synthesis and Assembly of Barium-Doped Iron Oxide Nanoparticles and Nanomagnets. *Nanoscale* **2015**, *7* (39), 16165–16169. https://doi.org/10.1039/C5NR05291B.

(11) Castellanos-Rubio, I.; Arriortua, O.; Iglesias-Rojas, D.; Barón, A.; Rodrigo, I.; Marcano, L.; Garitaonandia, J. S.; Orue, I.; Fdez-Gubieda, M. L.; Insausti, M. A Milestone in the Chemical Synthesis of Fe3O4 Nanoparticles: Unreported Bulklike Properties Lead to a Remarkable Magnetic Hyperthermia. *Chem. Mater.* **2021**, *33* (22), 8693–8704.
(12) Lee, K.; Lee, S.; Ahn, B. Understanding High Anisotropic Magnetism by Ultrathin Shell Layer Formation for Magnetically Hard–Soft Core–Shell Nanostructures. *Chem. Mater.* **2019**, *31* (3), 728–736. https://doi.org/10.1021/acs.chemmater.8b03591.
(13) Wetterskog, E.; Tai, C.-W.; Grins, J.; Bergström, L.; Salazar-Alvarez, G. Anomalous Magnetic Properties of Nanoparticles Arising from Defect Structures: Topotaxial Oxidation of $Fe_{1-x}O|Fe_{3-\delta}O_4$ Core|Shell Nanocubes to Single-Phase Particles. *ACS Nano* **2013**, *7* (8), 7132–7144. https://doi.org/10.1021/nn402487q.
(14) Qiao, L.; Fu, Z.; Li, J.; Ghosen, J.; Zeng, M.; Stebbins, J.; Prasad, P. N.; Swihart, M. T. Standardizing Size- and Shape-Controlled Synthesis of Monodisperse Magnetite (Fe_3O_4) Nanocrystals by Identifying and Exploiting Effects of Organic Impurities. *ACS Nano* **2017**, *11* (6), 6370–6381. https://doi.org/10.1021/acsnano.7b02752.
(15) Kirkpatrick, K. M.; Zhou, B. H.; Bunting, P. C.; Rinehart, J. D. Size-Tunable Magnetite Nanoparticles from Well-Defined Iron Oleate Precursors. *Chem. Mater.* **2022**, *34* (17), 8043–8053. https://doi.org/10.1021/acs.chemmater.2c02046.
(16) Narnaware, P. K.; Ravikumar, C. Mechanistic Insights into the Formation and Growth of Anisotropic-Shaped Wüstite–Spinel Core–Shell Iron Oxide Nanoparticles in a Coordinating Solvent. *J. Phys. Chem. C* **2020**, *124* (45), 25010–25027. https://doi.org/10.1021/acs.jpcc.0c05606.
(17) Mamiya, H.; Fukumoto, H.; Cuya Huaman, J. L.; Suzuki, K.; Miyamura, H.; Balachandran, J. Estimation of Magnetic Anisotropy of Individual Magnetite Nanoparticles for Magnetic Hyperthermia. *ACS Nano* **2020**, *14* (7), 8421–8432. https://doi.org/10.1021/acsnano.0c02521.
(18) Lv, Z.-P.; Wang, T.; Ge, J.-Y.; Luan, Z.-Z.; Wu, D.; Zuo, J.-L.; Sun, S. Controlling the Assembly and Spin Transport of Tetrathiafulvalene Carboxylate Coated Iron Oxide Nanoparticles. *J. Mater. Chem. C* **2017**, *5* (29), 7200–7206. https://doi.org/10.1039/C7TC01021D.
(19) Crespo, P.; de la Presa, P.; Marín, P.; Multigner, M.; María Alonso, J.; Rivero, G.; Yndurain, F.; María González-Calbet, J.; Hernando, A. Magnetism in Nanoparticles: Tuning Properties with Coatings. *J. Phys.: Condens. Matter* **2013**, *25* (48), 484006. https://doi.org/10.1088/0953-8984/25/48/484006.
(20) Johnson, N.; Kotz, S.; Balakrishnan, N. *Continuous Univariate Distributions*, 2nd ed.; Wiley, 1994; Vol. 1.
(21) Mukhopadhyay, A.; Bhowmick, K.; Mitra, G. B. Edgeworth Series Expansion of the Truncated Cauchy Function and Its Effectiveness in the Study of Atomic Heterogeneity. *Zeitschrift für Kristallographie - Crystalline Materials* **2000**, *215* (12), 718–726. https://doi.org/10.1524/zkri.2000.215.12.718.
(22) Borgia, G. C.; Brown, R. J. S.; Fantazzini, P. The Effect of Diffusion and Susceptibility Differences on T2 Measurements for Fluids in Porous Media and Biological Tissues. *Magnetic Resonance Imaging* **1996**, *14* (7–8), 731–736. https://doi.org/10.1016/S0730-725X(96)00157-9.
(23) Stapf, S.; Kimmich, R.; Seitter, R.-O. Proton and Deuteron Field-Cycling NMR Relaxometry of Liquids in Porous Glasses: Evidence for Lévy-Walk Statistics. *Phys. Rev. Lett.* **1995**, *75* (15), 2855–2858. https://doi.org/10.1103/PhysRevLett.75.2855.
(24) Vasquez, C. A.; Fazzito, S. Y. Simple Hysteresis Loop Model for Rock Magnetic Analysis. *Stud Geophys Geod* **2020**, *64* (1), 114–129. https://doi.org/10.1007/s11200-019-1942-8.
(25) Winterton, S. S.; Smy, T. J.; Tarr, N. G. On the Source of Scatter in Contact Resistance Data. *JEM* **1992**, *21* (9), 917–921. https://doi.org/10.1007/BF02665549.
(26) Ciner, C. Stock Return Predictability in the Time of COVID-19. *Finance Research Letters* **2021**, *38*, 101705. https://doi.org/10.1016/j.frl.2020.101705.

(27) Ma, Z.; Mohapatra, J.; Wei, K.; Liu, J. P.; Sun, S. Magnetic Nanoparticles: Synthesis, Anisotropy, and Applications. *Chem. Rev.* **2021**, acs.chemrev.1c00860. https://doi.org/10.1021/acs.chemrev.1c00860.
(28) Ding, H. L.; Zhang, Y. X.; Wang, S.; Xu, J. M.; Xu, S. C.; Li, G. H. Fe_3O_4@SiO_2 Core/Shell Nanoparticles: The Silica Coating Regulations with a Single Core for Different Core Sizes and Shell Thicknesses. *Chem. Mater.* **2012**, *24* (23), 4572–4580. https://doi.org/10.1021/cm302828d.
(29) Hufschmid, R.; Arami, H.; Ferguson, R. M.; Gonzales, M.; Teeman, E.; Brush, L. N.; Browning, N. D.; Krishnan, K. M. Synthesis of Phase-Pure and Monodisperse Iron Oxide Nanoparticles by Thermal Decomposition. *Nanoscale* **2015**, *7* (25), 11142–11154. https://doi.org/10.1039/C5NR01651G.
(30) Unni, M.; Uhl, A. M.; Savliwala, S.; Savitzky, B. H.; Dhavalikar, R.; Garraud, N.; Arnold, D. P.; Kourkoutis, L. F.; Andrew, J. S.; Rinaldi, C. Thermal Decomposition Synthesis of Iron Oxide Nanoparticles with Diminished Magnetic Dead Layer by Controlled Addition of Oxygen. *ACS Nano* **2017**, *11* (2), 2284–2303. https://doi.org/10.1021/acsnano.7b00609.
(31) Chen, D.-X.; Sanchez, A.; Taboada, E.; Roig, A.; Sun, N.; Gu, H.-C. Size Determination of Superparamagnetic Nanoparticles from Magnetization Curve. *Journal of Applied Physics* **2009**, *105* (8), 083924. https://doi.org/10.1063/1.3117512.
(32) Muscas, G.; Concas, G.; Laureti, S.; Testa, A. M.; Mathieu, R.; De Toro, J. A.; Cannas, C.; Musinu, A.; Novak, M. A.; Sangregorio, C.; Lee, S. S.; Peddis, D. The Interplay between Single Particle Anisotropy and Interparticle Interactions in Ensembles of Magnetic Nanoparticles. *Phys. Chem. Chem. Phys.* **2018**, *20* (45), 28634–28643. https://doi.org/10.1039/C8CP03934H.
(33) De Toro, J. A.; Normile, P. S.; Lee, S. S.; Salazar, D.; Cheong, J. L.; Muñiz, P.; Riveiro, J. M.; Hillenkamp, M.; Tournus, F.; Tamion, A.; Nordblad, P. Controlled Close-Packing of Ferrimagnetic Nanoparticles: An Assessment of the Role of Interparticle Superexchange Versus Dipolar Interactions. *J. Phys. Chem. C* **2013**, *117* (19), 10213–10219. https://doi.org/10.1021/jp402444x.
(34) Dumas, R. Correcting for the Absolute Field Error Using the Pd Standard; Application Note 1500-021, Rev. B0. **2020**.
(35) Dumas, R. Using SQUID VSM Superconducting Magnets at Low Fields; Application Note 1500-011, Rev. A0. **2010**.

Chapter 4

Analyzing Magnetization Curves of Molecular Er^{3+} Networks with 0−3-Dimensional Spin Interactivity

4.1 Introduction

While the materials of choice in Chapters 1-3 are superparamagnetic nanoparticles, many more interesting magnetic systems exist, including molecular materials.[1–6] Characterized by slow magnetic relaxation, single-molecule magnets (SMMs) are a family of materials that have gained incredible interest in recent decades for applications such as molecular spintronics and quantum information storage.[1–3] Extensive research efforts have focused on improving the functionality of SMMs by increasing the blocking temperature,[7,8] the critical point at below which the material exhibits slow relaxation of its magnetization in the absence of an applied magnetic field. While increasing the functional temperature remains a key goal in the field, it is equally important to comprehensively control and understand the directional dependence of magnetization (referred to as anisotropy) as well as the interactions between magnetic units.[9] This understanding is essential for practical applications of SMMs.

Molecular magnetism is a recently developed, yet diverse area of research at the intersection between chemistry, physics, materials science, and mathematics. Many subsets exist within molecular magnetism, including the study of multifunctional materials such as photoswitchable magnets,[10] as well as porous materials[11] and quantum spintronics materials.[12] At the heart of molecular magnetism is the single molecule magnet (SMM), an organometallic coordination complex which exhibits slow relaxation of its magnetization. The field of SMMs was initiated with the discovery that the Mn_{12} cluster retains its magnetization at extremely low temperatures.[13] While large organometallic clusters have been synthesized

approaching the scale of nanoparticles in attempts to increase the blocking temperature by maximizing spin,[14] extreme care must be taken in the arrangement and choice of metal(s) and ligand(s) to maximize magnetic anisotropy.

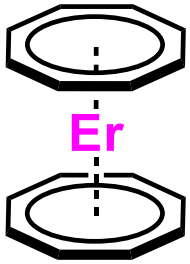

Figure 4.1. Depiction of erbium (III) bis-cyclooctatetraene anion.

To control magnetic anisotropy, appropriate ligands can be used to stabilize the magnetic moment, such as cyclopentadiene based ligands,[15] porphyrins,[16] and cyclooctatetraene.[17] In the case of erbium-based SMMs, the magnetic moment states of Er^{3+} form an oblate charge density, which is best stabilized by a symmetrical equatorial coordination environment, complementing the cyclooctatetraene dianion (COT^{2-}) in the complex $ErCOT_2$.[17] Termed Metal-Ligand Pair Anisotropy (MLPA), a single COT ring was found to sufficiently stabilize Er^{3+}, thereby leaving the remaining half of the Er^{3+} coordination sphere available for additional functionalities, such as bridging to other ErCOT units.[18,19] An incredible amount of synthetic tunability and creativity within the ErCOT MLPA system is possible, demonstrated by the bottom-up style synthesis of mono-, di-, and trinuclear ErCOT based magnets.[20] Synthetic choices, such as the ligands used to arrange the ErCOT units result in drastic changes in the magnetic properties.[21]

Generally, magnetization curves on molecular materials are measured with the primary intent of searching for open hysteresis, and in the process, a wealth of information is typically neglected. Typically, the coercive field (H_c) and saturation magnetization (M_s) are determined, along with a qualitative description of the shape. however, A quantitative in-depth analysis, however, reveals subtle differences that can be identified and compared. Statistical parameters can be extracted, quantified, and tracked, with the intent of better understanding the field dependent behavior. While the goal of this analysis was to determine the effect of crystallographic arrangement on the magnetization curve, additional parameters were explored,

such as the effect of dipolar coupling between units and temperature dependence. This work represents the first use of a purely statistical model to garner quantifiable parameters from magnetization curves of molecular magnetic materials.

This analysis, described in greater detail in Chapter 3, was previously carried out on the 300 K magnetization curves of superparamagnetic nanoparticles containing a single transition at exactly 0 T,[22] however, the $ErCOT_2$ system represents a much more complex magnetization curve involving multiple transitions. As such, a linear combination of multiple distribution functions is necessary to completely account for each component in the $ErCOT_2$ magnetization curves. The Cauchy distribution, also known as the Lorentz distribution, is a continuous distribution function has been used in chemistry and physics,[23–25] geology,[26] and economics[27] to model a variety of data and processes. The distribution can be presented in the cumulative distribution function (CDF, Equation 3.1) form or the probability density function (PDF, Equation 3.2) form. The CDF form represents magnetization vs. magnetic field, while the PDF form represents the derivative or magnetic susceptibility vs. magnetic field. Adapting the Cauchy distribution requires slight changes, with the implementation of a scaling factor (M_s), and substitution of the location factor from x_0 to H_p, representing the magnetic field at which the process is centered. The modified equations for fitting to the magnetization and derivative of the magnetization are show in Equation 3.3 and Equation 4.4, respectively. The open-source software package, *multi_cauchy*, was used to automatically parse, analyze, and plot the large amount of data for this study.[28]

$$F(x; x_0, \gamma) = \frac{1}{\pi} arctan\left(\frac{x - x_0}{\gamma}\right) + \frac{1}{2} \qquad \text{Equation 4.1}$$

$$f(x; x_0, \gamma) = \frac{1}{\pi}\left[\frac{\gamma}{(x - x_0)^2 + \gamma^2}\right] \qquad \text{Equation 4.2}$$

$$M(H;\ H_p, \gamma\ ) = \frac{2M_s}{\pi} arctan\left(\frac{H - H_p}{\gamma}\right) \qquad \text{Equation 4.3}$$

$$\chi(H;\ H_c, \gamma\ ) = \frac{2M_s}{\pi}\left[\frac{\gamma}{(x - x_p)^2 + \gamma^2}\right] \qquad \text{Equation 4.4}$$

4.2 Results and discussion

Co-crystallizing the identical magnetic unit of $[(ErCOT_2)]^-$ with various cationic molecules shown in Figure 1.1 changes the crystallographic arrangement between $ErCOT_2$ units. Depending on the counter-ion, the organizational motif can be described as layered hexagons, zig-zag triangles, or alternating sheets, altering both the spacing and angle between magnetic units. While a host of characterization techniques and additional analysis were carried out in this project, this chapter only describes the parsing, deconvolution, fitting, and analysis of the magnetization curves.

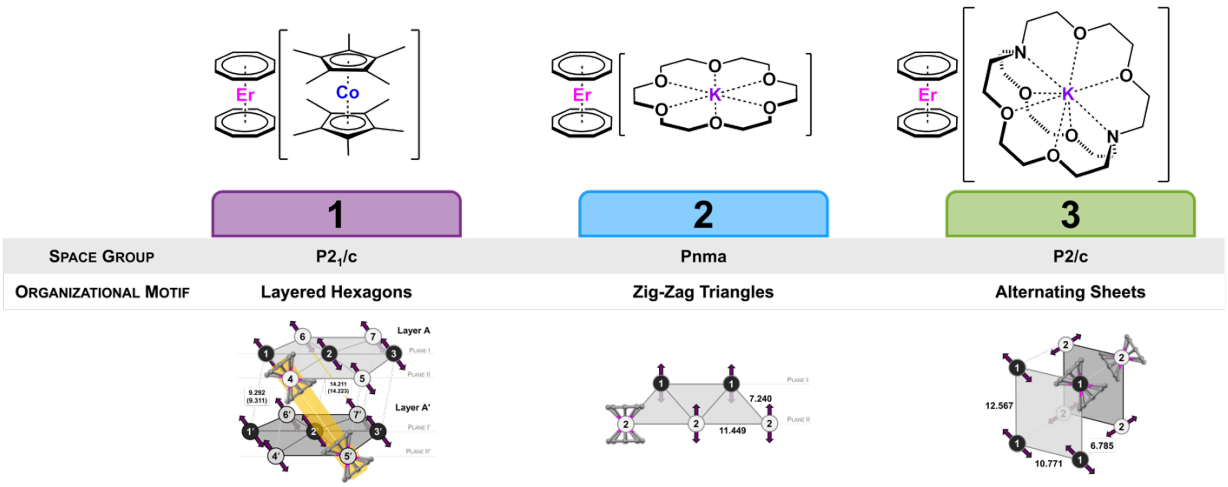

Figure 4.2. Scheme of molecular compounds **1**, **2**, and **3** with corresponding space group, organizational motif, and crystallographic arrangement of $ErCOT_2$ units.

For compounds **1**, **2**, and **3**, magnetization curves were collected at temperatures of 2, 4, 6, and 8 K at a magnetic field sweep rate of 60 Oe/s, with the 2 K scans shown in Figure 4.3. In the 2 K scan alone, clear differences between the curves of each compound are observed. While each exhibits the same number of inflection points in their magnetization curves, the magnitude and/or location of each process varies. While one could qualitatively compare the data to draw conclusions, describing the characteristics quantitatively—by mathematically determining the number of components and analyzing the curve shape, location, percent contribution, and magnitude of the curve—is significantly more meaningful. This approach makes it easier to make comparisons across samples and temperatures.

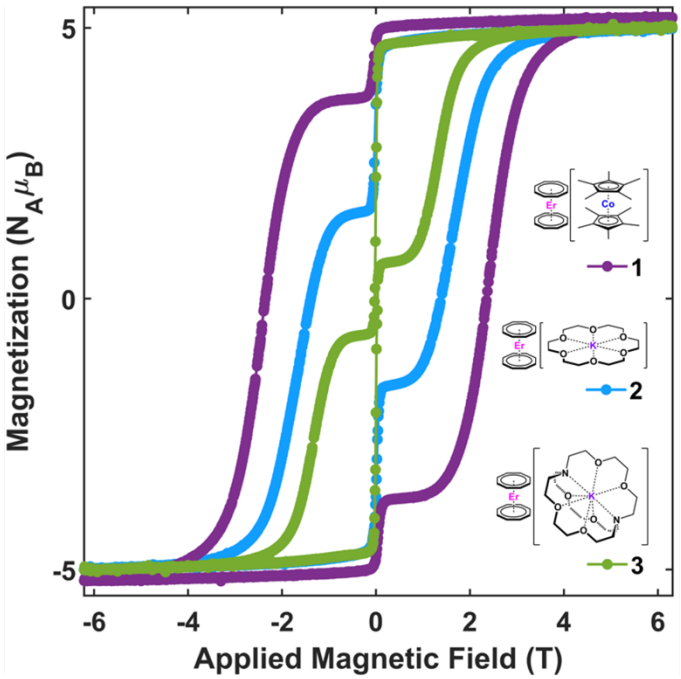

Figure 4.3. Magnetization curves of **1**, **2**, and **3** collected at 2 K at a magnetic field sweep rate of 60 Oe/s.

It is immediately clear from Figure 4.3 that two distinct processes take place near 0 field and between 1-3 T. Once the fitting analysis is carried out, however, a third process, albeit broad and low in intensity, presents itself near -2.5 T. This third component becomes clear at higher temperatures with the 8 K scan shown in Figure 4.4a. A testament to this fitting analysis, small contributions that would otherwise go unnoticed are now visible. Each of the three processes, described as "terms" in Figure 4.4a, are unique Cauchy distributions of Equation 3.3, which are ultimately combined to form the final function, shown in black, and fit to the data, shown in red/blue. The difference between the fit and the forward sweep (red) and reverse sweep (blue) of the magnetization curve is the residual, shown at the bottom of the plots in Figure 4.4. Clear visualization of the residual can help identify missing components or peaks, as well areas where the model may fail to properly fit the data.

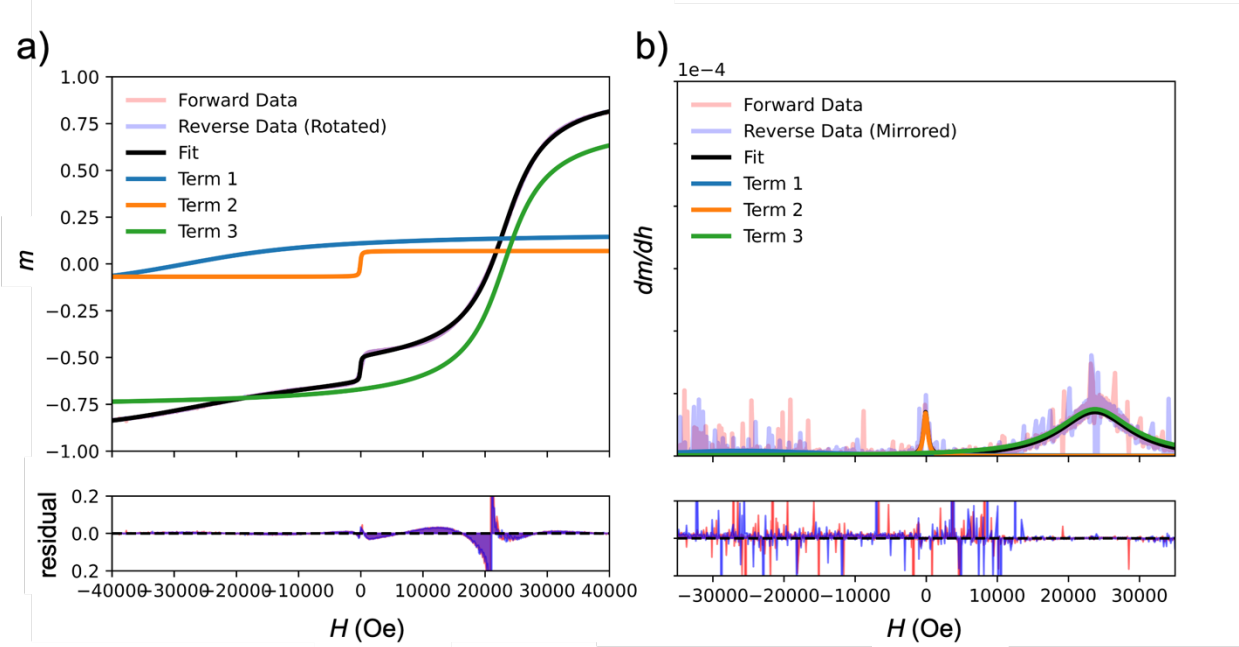

Figure 4.4. Magnetization curves of **1** collected at 8 K highlighting individual Cauchy components and resulting fit in its (a) CDF form and (b) PDF form.

An inherent advantage of the Cauchy distribution is the ability to view and fit the data in both the magnetization (CDF) and derivative (PDF) form. For example, Figure 4.4b shows the derivative of the magnetization curve, revealing distinct peaks, which can then be fit to the Cauchy PDF. The flexibility of statistical modelling allows one to move between both forms, which can be advantageous for visualization purposes. In this work, each magnetization curve was fit to a sum of three unique Cauchy CDF distributions. Those fit parameters can then be used to view the data in both the magnetization (CDF) and derivative of magnetization (PDF) form. While fits to both the magnetization and its derivative can be performed, in this case, only the fits to the magnetization curve (CDF) were carried out.

From the Cauchy fitting analysis, the parameters obtained are the half-width at half-max of the peak, denoted γ, and the location, denoted H_p. Additionally, determining the peak's maximum height and its overall percentage contribution, calculated based on the area under the curve, can complement the findings from the statistical model. It is worth noting that these peak parameters are interrelated, and the choice of which parameter to prioritize may depend on the specific system under investigation.

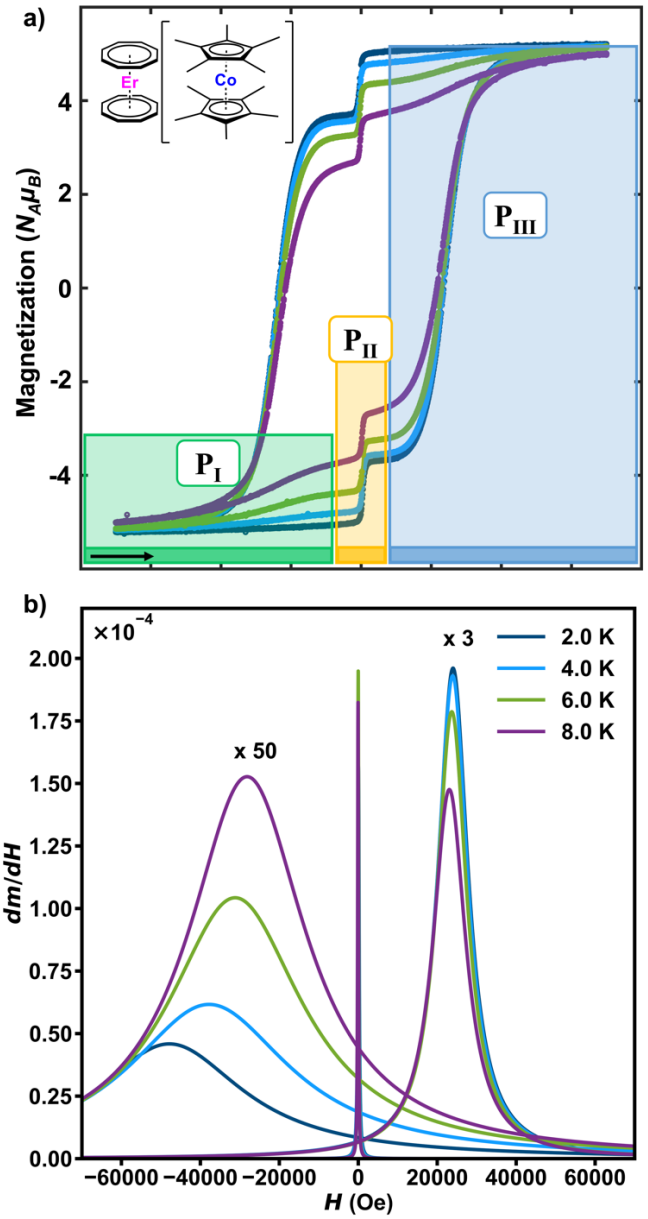

Figure 4.5. Cauchy analysis of compound **1** across a temperature range of T = 2, 4, 6, and 8 K. Magnetization curves (top) highlighting the three components, $\mathbf{P_I}$ (green), $\mathbf{P_{II}}$ (yellow), and $\mathbf{P_{III}}$ (blue). Cauchy PDFs from the fit analysis (bottom) with the first process ($\mathbf{P_I}$) and third process ($\mathbf{P_{III}}$) magnified.

The temperature dependence of each compound was analyzed, with **1**, [ErCOT$_2$][CoCp*$_2$], as an example in Figure 4.5. While a few differences are observed between the magnetization curves (Figure 4.5a), these subtle differences are much clearer when plotted as the PDF (Figure 4.5b). For example, $\mathbf{P_I}$ and $\mathbf{P_{III}}$ increase and decrease in height, respectively. While these temperature dependent differences can be described qualitatively, it is much more impactful to scientifically and rigorously quantify the changes.

While all of the quantitative parameters obtained from the fitting analysis give insight into the underlying nature of each inflection point of the magnetization curve, the peak properties are best described through percent contribution in this case. Determined by the area under the curve of each process with respect to the others, the percent contribution is normalized, allowing for comparison between compounds and potentially other molecular systems. Shown in Figure 4.6, both $\mathbf{P_I}$ and $\mathbf{P_{II}}$ steadily decrease in their percent contribution, while $\mathbf{P_{III}}$ increases. These temperature dependent trends are consistent for all compounds, demonstrated in Figure 4.9.

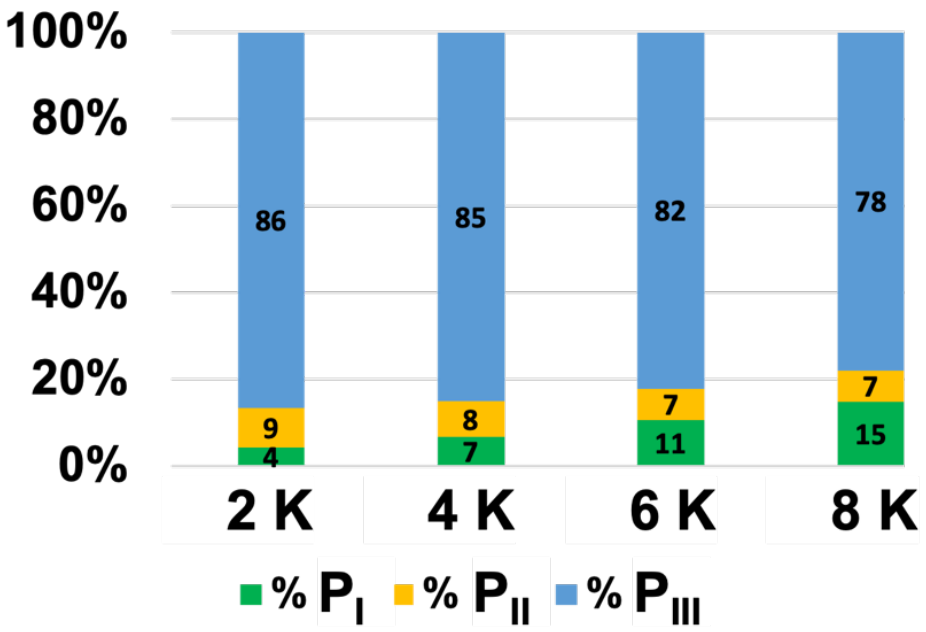

Figure 4.6. Bar graph of percent contributions for each process in **1** at T = 2, 4, 6, and 8 K.

The concrete quantification of the magnetization curves gained as a result of the Cauchy fitting is important in discussing the identity and underlying nature of each process. While the specific underlying phenomena behind processes $\mathbf{P_I}$ and $\mathbf{P_{III}}$ are yet to be unambiguously assigned, the tools needed for systematic tracking and analysis of these processes are now readily available.

The sharp change in magnetization that occurs near zero field ($\mathbf{P_{II}}$), however, is likely associated with a quantum process. An abrupt inflection point in magnetization is indicative of quantum tunneling of magnetization (QTM), a phenomenon in which the magnetic moment can undergo a coherent transition by

"tunneling" through the energy barrier to a different quantum state.[17] Additionally, $\mathbf{P_{II}}$ may also represent the quantum avalanche effect, characterized by a rapid cascade of dipole flipping in a self-propagating process.[29,30] Further complicating the assignment is the possibility that $\mathbf{P_{II}}$ may be a combination of both quantum effects occurring simultaneously. Dipolar interactions have been shown to impact the magnitude of both processes. To explore the underlying quantum effect(s) of $\mathbf{P_{II}}$ with respect to dipolar interactions between magnetic units, dilutions were prepared using diamagnetic yttrium analogues.

In addition to the temperature dependence, the magnetization curves of **1-3** were analyzed and compared to draw conclusions on the crystallographic differences, with the fit results shown in Figure 4.7. In each compound, the $ErCOT_2$ units can be simplified as an Ising-type spin that is held constant while the distance, angle, and strength of interactions between $ErCOT_2$ is varied. Structurally, compound **1** consists of a complex layered hexagon organization of $ErCOT_2$ units. While $ErCOT_2$ units between layers are predicted to interact ferromagnetically, the $ErCOT_2$ units within each layer are predicted to act in an antiferromagnetic fashion. Compound **2** is composed of a zig-zag triangle motif and compound **3** consists of alternating sheets of $ErCOT_2$ units.

Correlating each $ErCOT_2$ interaction observed in the crystal structure to a component in the magnetization curve is a non-trivial process, however, the fitting analysis still yields information on the impact of the three structural motifs on the overall curve. For example, a trend in increasing peak height is observed for $\mathbf{P_I}$ and $\mathbf{P_{III}}$ as the structural arrangement transitions from alternating sheets (**3**), to zig-zag triangles (**2**), and then layered hexagons (**1**). This trend, however, is reversed for $\mathbf{P_{II}}$, yielding insight into the effect of crystallographic structure on the behavior of the QTM process or quantum avalanche process. The percent contribution of each component is another parameter that can be used to make comparisons between samples, as it incorporates the area under the curve as opposed to the peak height alone.

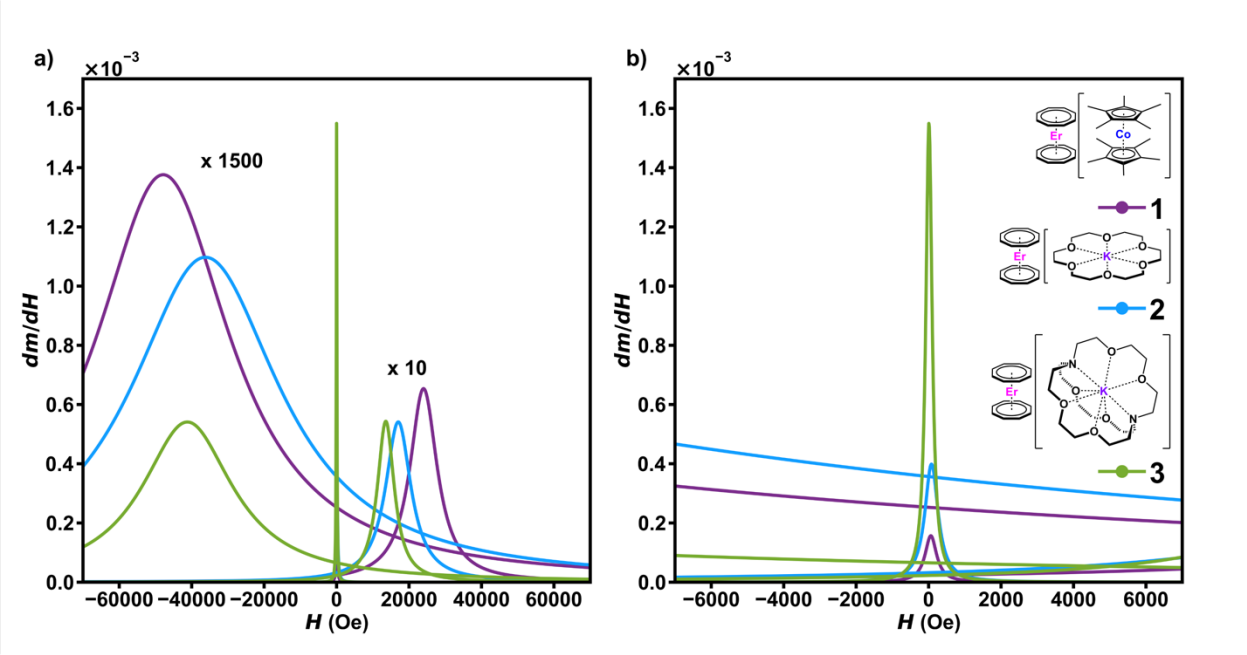

Figure 4.7. Magnetization curves of **1-3** collected at 2 K with individual Cauchy PDF contributions plotted from (a) H = -7 to 7 T and (b) H = -0.65 T to 0.65 T.

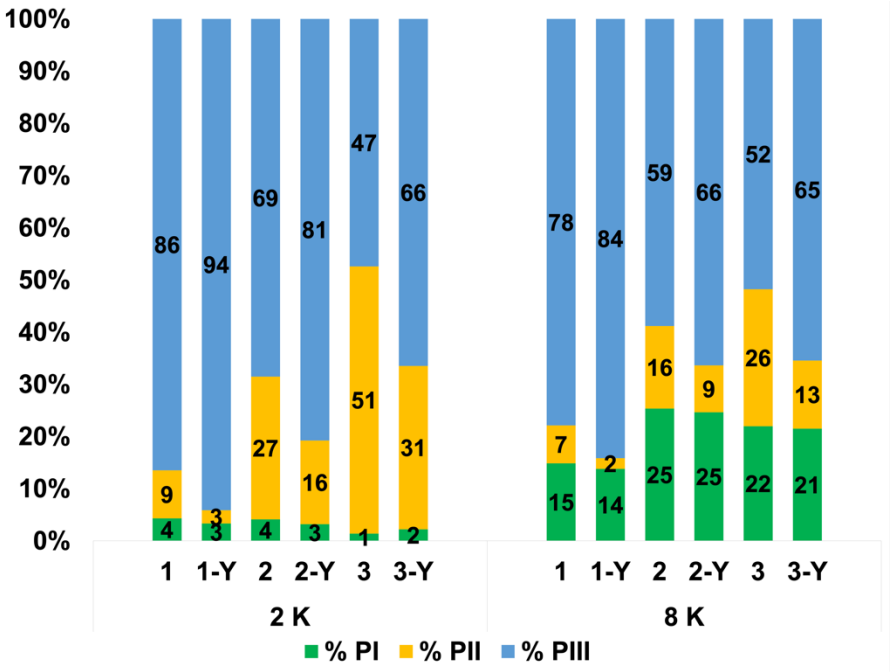

Figure 4.8. Bar graphs of percent contributions for each process in **1** and **1-Y** at T = 2 and 8 K.

Finally, to further study the impact of dipolar coupling between $ErCOT_2$ units, each of the three compounds shown in Figure 4.3 was diluted in a 95:5 molar ratio with the diamagnetic yttrium analogue,

$YCOT_2$, denoted **1-Y**, **2-Y**, and **3-Y**. The percent contribution of each component at both 2 and 8 K was utilized to compare the undiluted compounds to the diluted compounds, shown in Figure 4.8. Of particular note is the decrease of $\mathbf{P_{II}}$ in all diluted compounds, reinforcing the notion that $\mathbf{P_{II}}$ is a process dependent on the rapid flipping of spins; if the effective distance between $ErCOT_2$ units decreases, $\mathbf{P_{II}}$ would decrease as well. Additionally, $\mathbf{P_I}$ increases in its contribution across all diluted analogues, indicating the origin may be intramolecular, within each $ErCOT_2$ unit, as opposed to a long-range interaction, such as the quantum avalanche effect.

4.3 Conclusions

In this chapter, the magnetization curves of a series of $ErCOT_2$ compounds were fit to a statistical model. Each component constituting the overall curve was quantified and tracked across varying crystallographic arrangements, temperature, and degree of dipolar coupling by diluting with a diamagnetic analogue. This analysis provides a universal method to extract additional information from magnetization curves of molecular magnetic materials.

4.4 Experimental details

The magnetization curve fitting analysis was performed in Python using the *multi_cauchy* program developed by Phil Bunting of the Rinehart Lab.[28] While the software can automatically identify peaks, this analysis was carried out using user-specified peak locations and constraints. Fits were performed to both the magnetization and derivative of magnetization data using the Cauchy CDF and PDF, respectively. Fitting was carried out using the default least squares method of the LMFIT package. The data and code for this analysis can be found at https://doi.org/10.5281/zenodo.8322969, an online repository called Zenodo. A README is available with examples. The *multi_cauchy* software can be found at https://doi.org/10.5281/zenodo.8299498,

4.5 Additional information

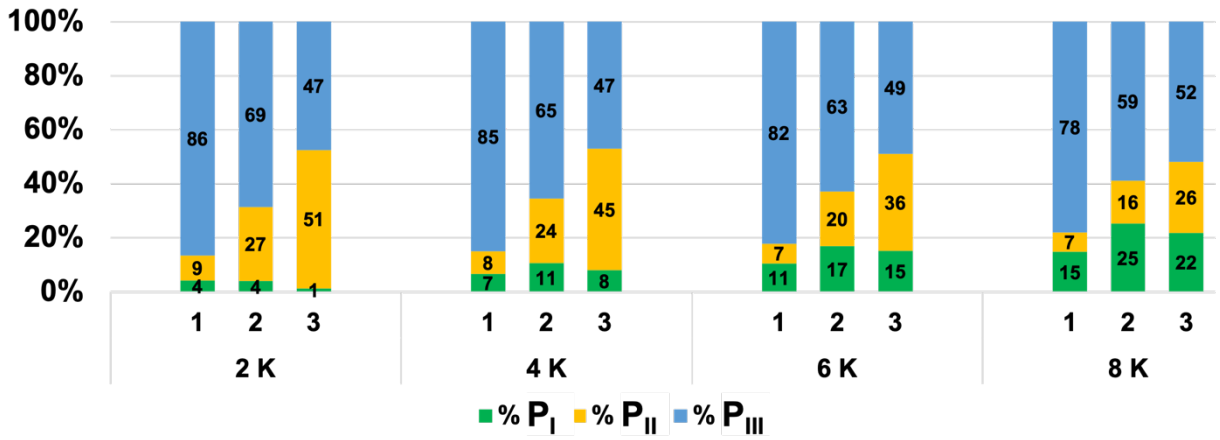

Figure 4.9. Bar graph of percent contributions for each process in **1**, **2**, and **3** at T = 2, 4, 6, and 8 K.

4.6 Acknowledgements

Chapter 4, is partially adapted from the manuscript entitled "Molecular Network Approach to Anisotropic Ising Lattices: Parsing Magnetization Dynamics in Er^{3+} Systems with 0–3-Dimensional Spin Interactivity" by Orlova, A. P.; Varley, M. S.; Bernbeck, M. G.; Kirkpatrick, K. M.; Bunting, P. C.; Gembicky, M.; Rinehart, J. D. The dissertation author was a secondary researcher of this paper. Reprinted with permission from *J. Am. Chem. Soc.* **2023.** Copyright 2023 American Chemical Society.

4.7 References

(1) Zadrozny, J. M.; Niklas, J.; Poluektov, O. G.; Freedman, D. E. Millisecond Coherence Time in a Tunable Molecular Electronic Spin Qubit. *ACS Cent. Sci.* **2015**, *1* (9), 488–492. https://doi.org/10.1021/acscentsci.5b00338.

(2) Sessoli, R. Toward the Quantum Computer: Magnetic Molecules Back in the Race. *ACS Cent. Sci.* **2015**, *1* (9), 473–474. https://doi.org/10.1021/acscentsci.5b00384.

(3) Wernsdorfer, W.; Sessoli, R. Quantum Phase Interference and Parity Effects in Magnetic Molecular Clusters. *Science* **1999**, *284* (5411), 133–135. https://doi.org/10.1126/science.284.5411.133.

(4) Woodruff, D. N.; Winpenny, R. E. P.; Layfield, R. A. Lanthanide Single-Molecule Magnets. *Chem. Rev.* **2013**, *113* (7), 5110–5148. https://doi.org/10.1021/cr400018q.

(5) Demir, S.; Jeon, I.-R.; Long, J. R.; Harris, T. D. Radical Ligand-Containing Single-Molecule Magnets. *Coordination Chemistry Reviews* **2015**, *289–290*, 149–176. https://doi.org/10.1016/j.ccr.2014.10.012.
(6) Gould, C. A.; Darago, L. E.; Gonzalez, M. I.; Demir, S.; Long, J. R. A Trinuclear Radical-Bridged Lanthanide Single-Molecule Magnet. *Angew. Chem. Int. Ed.* **2017**, *56* (34), 10103–10107. https://doi.org/10.1002/anie.201612271.
(7) Velkos, G.; Krylov, D. S.; Kirkpatrick, K.; Spree, L.; Dubrovin, V.; Büchner, B.; Avdoshenko, S. M.; Bezmelnitsyn, V.; Davis, S.; Faust, P.; Duchamp, J.; Dorn, H. C.; Popov, A. A. High Blocking Temperature of Magnetization and Giant Coercivity in the Azafullerene $Tb_2@C_{79}N$ with a Single-Electron Terbium–Terbium Bond. *Angew. Chem. Int. Ed.* **2019**, *58* (18), 5891–5896. https://doi.org/10.1002/anie.201900943.
(8) Vieru, V.; Gómez-Coca, S.; Ruiz, E.; Chibotaru, L. F. Increasing the Magnetic Blocking Temperature of Single-Molecule Magnets. *Angew Chem Int Ed* **2023**, e202303146. https://doi.org/10.1002/anie.202303146.
(9) Rinehart, J. D.; Long, J. R. Exploiting Single-Ion Anisotropy in the Design of f-Element Single-Molecule Magnets. *Chem. Sci.* **2011**, *2* (11), 2078. https://doi.org/10.1039/c1sc00513h.
(10) Arczyński, M.; Stanek, J.; Sieklucka, B.; Dunbar, K. R.; Pinkowicz, D. Site-Selective Photoswitching of Two Distinct Magnetic Chromophores in a Propeller-Like Molecule To Achieve Four Different Magnetic States. *J. Am. Chem. Soc.* **2019**, *141* (48), 19067–19077. https://doi.org/10.1021/jacs.9b09576.
(11) Maspoch, D.; Ruiz-Molina, D.; Wurst, K.; Domingo, N.; Cavallini, M.; Biscarini, F.; Tejada, J.; Rovira, C.; Veciana, J. A Nanoporous Molecular Magnet with Reversible Solvent-Induced Mechanical and Magnetic Properties. *Nature Mater* **2003**, *2* (3), 190–195. https://doi.org/10.1038/nmat834.
(12) Coronado, E. Molecular Magnetism: From Chemical Design to Spin Control in Molecules, Materials and Devices. *Nat Rev Mater* **2019**, *5* (2), 87–104. https://doi.org/10.1038/s41578-019-0146-8.
(13) Sessoli, R.; Gatteschi, D.; Caneschi, A.; Novak, M. A. Magnetic Bistability in a Metal-Ion Cluster. *Nature* **1993**, *365* (6442), 141–143.
(14) Schurkus, H. F.; Chen, D.; O'Rourke, M. J.; Cheng, H.-P.; Chan, G. K.-L. Exploring the Magnetic Properties of the Largest Single-Molecule Magnets. *J. Phys. Chem. Lett.* **2020**, *11* (10), 3789–3795. https://doi.org/10.1021/acs.jpclett.0c00020.
(15) Guo, F.-S.; Day, B. M.; Chen, Y.-C.; Tong, M.-L.; Mansikkamäki, A.; Layfield, R. A. Magnetic Hysteresis up to 80 Kelvin in a Dysprosium Metallocene Single-Molecule Magnet. *Science* **2018**, *362* (6421), 1400–1403. https://doi.org/10.1126/science.aav0652.
(16) Kan, J.; Wang, H.; Sun, W.; Cao, W.; Tao, J.; Jiang, J. Sandwich-Type Mixed Tetrapyrrole Rare-Earth Triple-Decker Compounds. Effect of the Coordination Geometry on the Single-Molecule-Magnet Nature. *Inorg. Chem.* **2013**, *52* (15), 8505–8510. https://doi.org/10.1021/ic400485y.
(17) Meihaus, K. R.; Long, J. R. Magnetic Blocking at 10 K and a Dipolar-Mediated Avalanche in Salts of the Bis(η^8-Cyclooctatetraenide) Complex $[Er(COT)_2]^-$. *J. Am. Chem. Soc.* **2013**, *135* (47), 17952–17957. https://doi.org/10.1021/ja4094814.
(18) Hilgar, J. D.; Flores, B. S.; Rinehart, J. D. Ferromagnetic Coupling in a Chloride-Bridged Erbium Single-Molecule Magnet. *Chem. Commun.* **2017**, *53* (53), 7322–7324. https://doi.org/10.1039/C7CC02356A.
(19) Hilgar, J. D.; Bernbeck, M. G.; Flores, B. S.; Rinehart, J. D. Metal–Ligand Pair Anisotropy in a Series of Mononuclear Er–COT Complexes. *Chem. Sci.* **2018**, *9* (36), 7204–7209. https://doi.org/10.1039/C8SC01361F.
(20) Orlova, A. P.; Hilgar, J. D.; Bernbeck, M. G.; Gembicky, M.; Rinehart, J. D. Intuitive Control of Low-Energy Magnetic Excitations via Directed Dipolar Interactions in a Series of Er(III)-Based Complexes. *J. Am. Chem. Soc.* **2022**, *144* (25), 11316–11325. https://doi.org/10.1021/jacs.2c03236.

(21) Hilgar, J. D.; Bernbeck, M. G.; Rinehart, J. D. Million-Fold Relaxation Time Enhancement across a Series of Phosphino-Supported Erbium Single-Molecule Magnets. *J. Am. Chem. Soc.* **2019**, *141* (5), 1913–1917. https://doi.org/10.1021/jacs.8b13514.
(22) Kirkpatrick, K. M.; Zhou, B. H.; Bunting, P. C.; Rinehart, J. D. Quantifying Superparamagnetic Signatures in Nanoparticle Magnetite: A Generalized Approach for Physically Meaningful Statistics and Synthesis Diagnostics. *Chem. Sci.* **2023**, *14* (27), 7589–7594. https://doi.org/10.1039/D3SC02113K.
(23) Mukhopadhyay, A.; Bhowmick, K.; Mitra, G. B. Edgeworth Series Expansion of the Truncated Cauchy Function and Its Effectiveness in the Study of Atomic Heterogeneity. *Zeitschrift für Kristallographie - Crystalline Materials* **2000**, *215* (12), 718–726. https://doi.org/10.1524/zkri.2000.215.12.718.
(24) Borgia, G. C.; Brown, R. J. S.; Fantazzini, P. The Effect of Diffusion and Susceptibility Differences on T2 Measurements for Fluids in Porous Media and Biological Tissues. *Magnetic Resonance Imaging* **1996**, *14* (7–8), 731–736. https://doi.org/10.1016/S0730-725X(96)00157-9.
(25) Stapf, S.; Kimmich, R.; Seitter, R.-O. Proton and Deuteron Field-Cycling NMR Relaxometry of Liquids in Porous Glasses: Evidence for Lévy-Walk Statistics. *Phys. Rev. Lett.* **1995**, *75* (15), 2855–2858. https://doi.org/10.1103/PhysRevLett.75.2855.
(26) Vasquez, C. A.; Fazzito, S. Y. Simple Hysteresis Loop Model for Rock Magnetic Analysis. *Stud Geophys Geod* **2020**, *64* (1), 114–129. https://doi.org/10.1007/s11200-019-1942-8.
(27) Ciner, C. Stock Return Predictability in the Time of COVID-19. *Finance Research Letters* **2021**, *38*, 101705. https://doi.org/10.1016/j.frl.2020.101705.
(28) Bunting, Philip C.; Rinehart, J. D. Multi_cauchy. *Zenodo v1.0.1*.
(29) McHugh, S.; Wen, B.; Ma, X.; Sarachik, M. P.; Myasoedov, Y.; Zeldov, E.; Bagai, R.; Christou, G. Tuning Magnetic Avalanches in the Molecular Magnet Mn 12 -Acetate. *Phys. Rev. B* **2009**, *79* (17), 174413. https://doi.org/10.1103/PhysRevB.79.174413.
(30) Sarachik, M. P. Magnetic Avalanches in Molecular Magnets. arXiv February 20, 2013. http://arxiv.org/abs/1302.5100 (accessed 2023-11-01).